Multi-resolution Modeling and Simulation of Marine Hydrokinetic Turbine Arrays at Site Scale

A THESIS
SUBMITTED TO THE FACULTY OF THE GRADUATE SCHOOL
OF THE UNIVERSITY OF MINNESOTA
BY

Saurabh Chawdhary

IN PARTIAL FULFILLMENT OF THE REQUIREMENTS
FOR THE DEGREE OF
DOCTORATE OF PHILOSOPHY

Prof. Fotis Sotiropoulos and Prof. Lian Shen

April, 2017

Acknowledgements

The work done in this thesis would not have been possible without generous help and support of many people. First and foremost, I would like to thank my adviser Prof. Fotis Sotiropoulos for entrusting in me. I appreciate the belief he showed in me by providing me an opportunity to work on this dissertation. He agreed to support my Ph.D. at a time when I was looking for second adviser and was considering dropping out of grad school at the same time. If it was not for him, I may not have continued with Ph.D. The quality that I admire most in my adviser, is the fundamental approach of solving problems even for the problems of most applied nature. I tried to imbibe this quality throughout my research. I also sincerely thank my adviser Prof. Lian Shen for his kind and generous support, specially during the final year of my degree. His support and motivation in the final stages were crucial in finishing this thesis. He was always ready to provide help and feedback. I am thankful to other members in my committee. Prof. Michele Guala helped me throughout grad school. I could walk up to him and talk about research anytime of the day. I benefited from his insight as an experimentalist. Prof. Terence Simon provided valuable feedback on my writing and on the general direction of the research.

The help and support of all members of my research group was critical in the successful completion of my thesis. I received constant support from Dr. Dionysios Angelidis and Dr. Xiaolei Yang who were willing to invest time in helping with any problem whatsoever. I also thank other fellow researchers: Dr. Antoni Calderer, Mohammad Hajit, Dr. Aaron Boomsma, Dr. Ali Khosronejad, Dr. Anvar Gilmanov, Dr. Craig Hill, Dr. Daniel Foti, Dr. Jonathan Schwenk, Mirko Musa and fellow students at St. Anthony Falls Laboratory (SAFL). I learned a lot through my interactions with them. Looking back, I could not have asked for a better research group to work with.

I also wish to acknowledge the sponsorship from National Science Foundation (NSF) through NSF-grant IIP-1318201. I am thankful to the support of Minnesota Supercomputing Institute for providing computational resources. The information–technology support at SAFL eased my technical troubles. I am thankful to Matt Jansen, Charles Nguyen and other members of SAFL staff for their quick help throughout my stay at SAFL.

I wish to express my sincerest gratitude towards my family members - my sisters, Saumya & Shalini, my Mom and Dad. I would not have achieved anything without my parents‘ constant support and encouragement for my endeavors. I wish to acknowledge the support of many friends in the beautiful city of Minneapolis, who were always there to lift my spirits up every time I needed. The support structure that the lovely people I met in Minneapolis provided, gave me the required emotional strength to work through graduate school. In the fire of graduate school, great friendships were forged that will be cherished for at least a lifetime.

Lastly, I wish to express heartfelt gratitude to the river Mississippi. The calm and peace that the waters bestowed upon me, made the difficult experiences a lot easier to bear.

“Study nature, love nature, stay close to nature. It will never fail you.” *Frank Lloyd Wright.*

Dedication

To all those who held me up over the years.

Abstract

Marine and hydro-kinetic (MHK) energy hold promise to become significant contributor towards sustainable energy generation. Despite the promise, commercialization of MHK energy technologies is still in the development stage. While many simplified models for MHK site resource-assessment exist, more research is needed to enable efficient energy extraction from identified MHK sites. A marine energy company named Verdant Power Inc. was granted first federal license to install up to 30 axial hydrokinetic turbines in the East River in New York City under what came to be known as Roosevelt Island Tidal Energy (RITE) project. Therefore, in this study we investigate issues of relevance to post-site-identification stage for a real-life tidal energy project, the RITE project, using high-fidelity numerical simulations.

An effective way to develop arrays of hydrokinetic turbines in river and tidal channels is to arrange them in TriFrame configurations where three turbines are mounted together at the apexes of a triangular frame. The TriFrames serve as the building block for rapidly deploying multi-turbine arrays. The wake structure of a TriFrame of three model turbines is investigated. We employ large-eddy simulation (LES) with the curvilinear immersed boundary method (CURVIB) for fully resolving the turbine geometry details to simulate turbine-turbine wake interactions in the TriFrame configuration. First, the computed results are compared with experiments in terms of mean flow and turbulence characteristics with overall good agreement with bed-flume experiments. The flow-fields are then analyzed to elucidate the mechanisms of turbine interactions and wake evolution in the TriFrame configuration. We found that the wake of the upstream TriFrame turbine exhibits unique characteristics indicating presence of the Venturi effect as the wake encounters the two downstream turbines. We finally compare the wakes of the TriFrame turbines with that of an isolated single turbine wake to further illustrate how the TriFrame configuration affects the wake characteristics and power production in an array of TriFrames.

Lastly, we propose a large eddy simulation (LES)-based framework to investigate the site-specific flow dynamics past MHK arrays in a real-life marine environment. To this end, the new generation unstructured Cartesian flow solver, coupled with a sharp

interface immersed boundary method for 3D incompressible flows, is used. Optimized data-structures and efficient algorithms were developed to enable faster simulation on high-resolution grids. Multi-resolution simulations on locally refined grids are then employed to model the flow in a section of the East River with detailed river bathymetry and inset turbines at field scale. The results are analyzed in terms of the wake recovery and overall wake dynamics in the array. Comparison with the baseline flow in the East River reveal the effects of tidal array installation.

Contents

List of Tables

List of Figures

Chapter 1

Motivation

Water has been a reliable source of energy for our civilization since the invention of water wheel to power flour grinding, irrigation and water lifting. Technological advancements in hydropower since then have been increasing the usable hydropower. By the end of 2011, the global installed hydroelectric capacity was reported to be 1.31 TWe [17]. As per the U.S. Energy Information Administration [18], total hydroelectric production in the U.S. during 2005 was 270 TW·h, about three quarters of total renewable energy production in the nation. In 2012, the total hydroelectric production was about the same, but its share in renewable energy production decreased to 55% from the 205 share of 75%. Clearly, in spite of hydroelectricity being a renewable resource, the industry has not seen significant growth in the U.S; growth figures are similar for many other developed countries.

Hydroelectric power plants create a range of adverse impacts on the environment. Lack of dissolved oxygen in the tailrace of the plant severely affects the wildlife in the downstream water [19, 20]. Hydropower operations can also significantly alter the sediment transport and river channel dynamics in the long run [21, 22]. This creates space for more research in order to overcome existing challenges in extracting energy from hydro sources. While there are efforts to improve hydroelectric power generation, a viable alternative to harness energy from flowing stream of water has come up in the form of Marine and hydrokinetic (MHK) systems which do not require a dam for impounding water [23]. Instead, MHK systems use the kinetic energy of the free flowing natural streams (or bodies) of water - river, tidal channels, sea waves etc. Hydrokinetic

generation does not involve significantly altering the natural flow path of the water streams.

Figure 1.1: MHK turbines under development for deployment at commercial scale [2].

According to the U.S. Marine and Hydrokinetic Renewable Energy Roadmap [2], MHK resource has potential to supply up to 10% of total U.S. energy demand, more than the amount of electricity produced by all conventional hydropower in the country. Ocean Renewable Energy Coalition (OREC) lists the total installed MHK energy capacity of at least 15 GW by 2030 as one of its goals in this roadmap. However, MHK power generation is a relatively new research field and currently in commercial development stage. There are several proposed MHK devices for energy extraction which are still undergoing prototype testing phase (See Fig. 2.1). One can draw stark similarities between the nascent MHK industry as it stands today and the wind energy sector before it became a booming industry in last 10 years. Sustained efforts in research and development are needed to support the industry through the current phase in order to realize the goal of 15 GW by 2030.

The complex features of the marine environments such as intricate bed topography, highly turbulent flows and moving sediment beds pose major research challenges. These features can significantly influence the performance and structural integrity of the hydrokinetic turbines. Critical prerequisites for the successful development of an efficient multi-turbine MHK arrays are to develop techniques for: quantifying the amount of energy the array can extract under a wide range of turbulent flow conditions; optimizing the placement of turbines in the array; and evaluating potential interactions between the turbines and the aquatic environment. Computational modeling presents a viable approach for tackling these questions. The answers are highly correlated to the features of the site under consideration. The marine bathymetry, flow speeds and sediment bed characteristics play important role in determining the array configuration for

maximum energy extraction. The turbine-turbine and turbine-bathymetry interactions should also be accurately accounted for in the model. The goal of the current study is to investigate the research questions posed here in a site specific manner and address the computational challenges in development of an efficient and scalable numerical model.

Chapter 2

Introduction

Water has been a reliable source of energy for our civilization since the invention of water wheel to power flour grinding, irrigation and water lifting. Technological advancements in hydropower since then have been increasing the usable hydropower. By the end of 2011, the global installed hydroelectric capacity was reported to be 1.31 TWe [17]. As per the U.S. Energy Information Administration [18], total hydroelectric production in the U.S. during 2005 was 270 TW·h, about three quarters of total renewable energy production in the nation. In 2012, the total hydroelectric production was about the same, but its share in renewable energy production decreased to 55% from the 205 share of 75%. Clearly, in spite of hydroelectricity being a renewable resource, the industry has not seen significant growth in the U.S; growth figures are similar for many other developed countries.

Hydroelectric power plants create a range of adverse impacts on the environment. Lack of dissolved oxygen in the tailrace of the plant severely affects the wildlife in the downstream water [19, 20]. Hydropower operations can also significantly alter the sediment transport and river channel dynamics in the long run [21, 22]. This creates space for more research in order to overcome existing challenges in extracting energy from hydro sources. While there are efforts to improve hydroelectric power generation, a viable alternative to harness energy from flowing stream of water has come up in the form of Marine and hydrokinetic (MHK) systems which do not require a dam for impounding water [23]. Instead, MHK systems use the kinetic energy of the free flowing natural streams (or bodies) of water - river, tidal channels, sea waves etc. Hydrokinetic

generation does not involve significantly altering the natural flow path of the water streams.

Figure 2.1: MHK turbines under development for deployment at commercial scale [2].

According to the U.S. Marine and Hydrokinetic Renewable Energy Roadmap [2], MHK resource has potential to supply up to 10% of total U.S. energy demand, more than the amount of electricity produced by all conventional hydropower in the country. Ocean Renewable Energy Coalition (OREC) lists the total installed MHK energy capacity of at least 15 GW by 2030 as one of its goals in this roadmap. However, MHK power generation is a relatively new research field and currently in commercial development stage. There are several proposed MHK devices for energy extraction which are still undergoing prototype testing phase (See Fig. 2.1). One can draw stark similarities between the nascent MHK industry as it stands today and the wind energy sector before it became a booming industry in last 10 years. Sustained efforts in research and development are needed to support the industry through the current phase in order to realize the goal of 15 GW by 2030.

The complex features of the marine environments such as intricate bed topography, highly turbulent flows and moving sediment beds pose major research challenges. These features can significantly influence the performance and structural integrity of the hydrokinetic turbines. Critical prerequisites for the successful development of an efficient multi-turbine MHK arrays are to develop techniques for: quantifying the amount of energy the array can extract under a wide range of turbulent flow conditions; optimizing the placement of turbines in the array; and evaluating potential interactions between the turbines and the aquatic environment. Computational modeling presents a viable approach for tackling these questions. The answers are highly correlated to the features of the site under consideration. The marine bathymetry, flow speeds and sediment bed characteristics play important role in determining the array configuration for

maximum energy extraction. The turbine-turbine and turbine-bathymetry interactions should also be accurately accounted for in the model. The goal of the current study is to investigate the research questions posed here in a site specific manner and address the computational challenges in development of an efficient and scalable numerical model.

The primary mechanism of energy extraction for (MHK) turbines is similar to wind turbines. Multiple aerofoil shaped blades are connected to a rotor shaft. The kinetic energy of flowing water turns the blades around the rotor. This spins the rotor which in turn is used to spin the electrical generator. In the present study, we are interested in turbines laid out in an array in a current based system. Though current based sources may include river, ocean and tidal currents and canals, our focus lies on the tidal currents. A field scale three dimensional numerical simulation of a long reach of stream of water, with or without the turbines, is an extremely challenging computational problem because of high Reynolds number and complex natural river geometry and bathymetry. This is also apparent in the previously published literature on natural river simulations. The following sub-sections summarize related computational efforts in the literature.

2.1 Previous works on river flow simulation

Sinha *et al.*'s work [24] was the first attempt to simulate a large reach of a natural river along with the complex features including the islands on the river and bathymetry with sharp geometric gradients. They used the k-ϵ turbulence model with the Reynolds Averaged Navier-Stokes (RANS) equations in generalized curvilinear coordinates to study flow in a 4 km stretch of Columbia river downstream of the Wanapum Dam. Boundary fitted grids were used to conform to the geometrical features. A maximum Reynolds number of 27300 was simulated. A multi-block grid approach was used to refine the grid in the vicinity of complex features in the domain. The computed mean velocity profile was in excellent agreement with the measured values.

In 2004, Rodriguez *et al.* [25] performed numerical simulations of flow in a highly sinuous 70m reach of the Embarras river incorporating natural geometry using Flow-3D software. The grid was reconstructed from field data of the river bathymetry. Boundary conditions were based on the field measurements. The Renormalization Group (RNG)

theory, an improvement over k-ϵ, was used for turbulence closure of RANS equations. The RNG theory is known to provide better predictions for near-wall flows and flows with rapid distortions [26, 27]. The Reynolds number was approximately 5×10^5, much higher compared to similar studies. The computed results agreed well with the measurements in the reach. Abad *et al.* [28] also performed simulations based on a natural river geometry using a model similar to that of Rodriguez *et al.* [25]. They studied the flow in a meander bend of the Sugar Creek and the numerical results were in good agreement with the field measured data,

Kang. *et al.* [29] studied flow in a pseudo-natural meandering channel in the Outdoor Stream Lab (OSL) installed at the St. Anthony Falls laboratory (SAFL). The CURvilinear Immersed Boundary (CURVIB) method [30] was extended to incorporate dynamic Large Eddy Simulation (LES). Subgrid stresses were modeled using a dynamic Smagorinsky model [31]. LES is well suited for river flows where most of the energy is contained in energetic albeit slowly moving large eddies. The mean velocity field predictions from the computations were in good agreement with the velocity measured in the OSL. LES results were compared with the $k-\omega$ RANS model and it was found that the RANS model predicted an order of magnitude higher turbulent kinetic energy (TKE) in a shallow region near the bed. This limitation of the RANS type two equation model was also reported earlier by Stosser *et al.* [32]. Furthermore, Kang and Sotiropoulos [33] showed that the $k-\omega$ model was not able to capture the complex multi-cellular patterns of the secondary flow within strongly curved meandering bend. LES, on the other hand, could successfully reproduce the secondary cells.

The simulation in a natural river geometry with highest reported Reynolds number was performed using Fluent software for a reach of the Hudson river estuary [34]. The Reynolds number based on mean depth of 20 m was 11 million. Both LES and unsteady RANS were used for turbulence modeling and results were validated with average velocity measurements from ADCPs (Acoustic Doppler Current Profilers) installed in the Hudson river.

Recently, Khosronejad *et al.* [35] developed a high fidelity framework to model the coupled river hydrodynnamics and morphodynamics. In this method, the sediment water interface is treated as Immersed Boundary using the CURVIB-FSI approach of Borazjani *et al.* [5]. The method is extensively validated with the existing literature.

This method could predict the scouring around bridges piers [36] and to study scour produced by flow past different stream restoration rock structures in a laboratory setting [37].

2.2 Previous works on resource assessment for energy extraction

Garrett and Cummins [51, 52, 53] determines the maximum limit of power that can be extracted from tidal channels using turbines. A one dimensional theoretical model suggested that the limit is considerably less than the average kinetic energy flux of the channel without turbines. This is because as the number of turbines flocking the channel is increased the available energy for successive turbines is reduced. Table 2.1, reproduced from [1], summarizes the numerical studies in the last 10 years for resource assessment of marine current energy at various sites across the world. Ben *et al.* [39] developed a Matlab model to simulate forces the on rotor and power generated by turbines. Turbines were modeled using Blade Element Momentum (BEM) approach. Modeling of flow over the turbine was simply done by taking flow velocity from oceanographic databases and using them with the turbine model, without considering the natural site geometry. In another 2D model for resource assessment in tidal passage [40] a series of turbines were represented by increasing the bottom friction over the entire passage. The power generated in such a model was estimated as a fixed fraction of total drag power on the bottom of channel. In resource evaluation study for *Ría de Muros* (Northwest Spain) [41] the depth averaged 2D equations were solved using Delft3D-FLOW numerical code. Power extraction was modeled (using equation 2.1) as fixed fraction (equal to power coefficient C_p) of kinetic energy flux incident on the cross section equivalent to a fictitious turbine.

$$p_c = \frac{1}{2} C_p \rho V^3 \tag{2.1}$$

where ρ is density of water, V is flow speed over the turbine and p_c is the extracted power. The power coefficient was assumed constant $C_p = 0.33$.

O'Rourke *et al.* [44] employed a 2D depth-averaged model for resource assessment with a grid spacing of 405m (and subgrids of 45m and 135m in some regions) and claimed it to be more accurate in resolving bathymetry of the site than the previous

Table 2.1: Numerical assessment of marine current energy by various researchers[1]

Year	**Site**	**Model**	**Developer**	**Ref.**
2006	Portland Bill, UK	TÉLÉMAC	Électricité de France	[38]
2007	Raz de Sein, Brittany, France	Matlab-Simulink	MathWorks	[39]
2008	Minas Passage, Bay of Fundy, Canada	2-D finite-volume model (FVCOM)	C. S. Chen, Cowles G & Beardsley	[40]
2009	Ra de Muros, Spain	Delft 3D-FLOW	Delft Hydraulics	[41]
	Various sites in Norway	Bergen Ocean Model & High Resolution Tidal Model	University of Bergen & University of Oslo	[42]
	Puget Sound, Washington, USA	1-D time dependant model	University of Washington	[43]
2010	Various sites in Ireland	2-D depth-integrated numerical model	RPS Kirk McClure Morton	[44]
	South Wales coast, UK	Refined finite volume numerical model	Cardiff University	[45]
	Various sites in Malasiya	Princeton Ocean Model (POM)	Princeton University	[46]
2011	Georgia coast, USA	Regional Ocean Modeling System (ROMS)	Rutgers IMCS Ocean Modeling Group	[47]
	Verde Island Passage, Philippines	Delft 3D	Delft Hydraulics	[48]
2012	Langyatai Strait, China	Delft 3D-FLOW	Delft Hydraulics	[49]
	South Carolina coast, USA	Regional Ocean Modeling System (ROMS)	Rutgers IMCS Ocean Modeling Group	[50]

studies using grid spacing of the order of several kilometers. The model was validated against ADCP measurements on the east coast of Ireland. The power extraction was determined using an empirical relationship similar to Equation 2.1.

In many other resource assessment studies similar approaches were used i.e., employment of a 2D depth averaged model to obtain the flow velocity and equation 2.1 with pre-specified C_p to estimate power extraction [45, 46, 49]. Some others use specialized ocean modeling codes like Princeton Ocean Model (POM) [54] or Regional Ocean Modeling System (ROMS) [55] to obtain the flow field [46, 47, 50].

2.3 Previous works on 3D simulations of flow over MHK turbines

Numerical modeling techniques have proven useful in studying the wake of wind turbines - either resolving the actual 3D turbines or modeling the turbine as a momentum sink (actuator disk theory) [56, 57, 58]. Numerical techniques are an effective tool for optimization of MHK turbines arrays. However, there are very few previous researchers who have studied the specific problem of flow past MHK turbines and its effects on and interaction with river beds through 3D numerical simulations. Most studies on flow around MHK have so far focused on artificial channel or straight ducts, often using a 2D simplification.

Kang *et al.* [59] made the first attempts to model turbulent flow past real-life 3D turbine. A turbine resolving LES was carried out in a straight laboratory flume with 185 million grid nodes accurately resolving the geometry of the rotor blades and all other structures of the turbine. The spatially filtered mean flow Navier-Stokes equations were solved using the CURVIB method [30] with wall modeling for reconstructing velocity boundary conditions near all solid surfaces. Firstly, flow past an isolated rotor was simulated along with a grid convergence study. For the second simulation, a complete turbine including all three rotating blades, nacelle and the mounting structure were included as immersed boundaries. The computed torque, power and C_p were within 9.4%, 5.5% and 4.1% of their values measured in experiments respectively. However, among the two simulations mentioned, even though the predicted C_p were very close, the instantaneous downstream flow patterns were significantly different (see Fig. 2.2). It

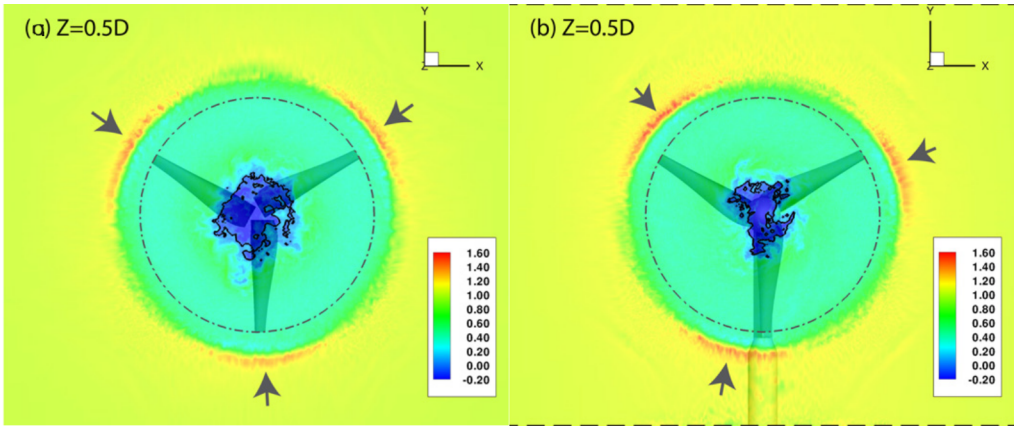

Figure 2.2: The contour plot of the instantaneous streamwise velocity nondimensionalized by bulk mean velocity at the xy-plane located 0.5 diameters downstream of the rotor at the fifth rotor revolution. The rotor rotates in the clockwise direction around the +z axis. The solid and dash-dot lines denote the zero streamwise velocity contours and the trace of the tip of the blades, respectively. The arrows mark the footprints of the three blade tip vortices. Simulation with (a) rotor only; (b) full assembly.

was concluded that, for the turbine geometry under consideration, the presence of parts other than rotor does not significantly affect the pressure field near the rotor (which was indicated by only slight difference in torque), power and C_p values.

Wake meandering of an MHK turbine was further investigated by Kang *et al.* [11]. A geometry resolving LES was performed to mimic the experiments of Chamorro *et al.* [10]. It was found that the precessing hub vortex has a profound effect on the downstream wake. The inner swirling flow, rotating counter to the turbine rotation, interacts with the outer shear layer at some downstream location. This results in considerable increase in the streamwise and cross-stream strength of the wake, enhanced wake meandering and increased turbulence mixing across the wake boundaries. In comparison with simulations with actuator models it was shown that they under-predicted the thickness and streamwise extent of the meandering region. This study highlighted the importance of resolving the geometry of the turbine.

Lawson *et al.* [60] at National Renewable Energy Laboratory (NREL) used the standard rotor design *Reference Model 1* described by the Department of Energy (DOE) to perform a turbine resolving 3D numerical simulations (using STAR CCM+ solver).

Both steady RANS and unsteady RANS ($k-\omega$ SST model) turbulence models were employed to study turbine performance. Good agreement was reported between the two methods. Steady state rotor torque was compared with the corresponding BEM prediction and found that BEM method under-predicts the hydrodynamic force on the rotor. Effects of grid size and time step were also investigated. The study concluded that in order to make accurate predictions, better turbulence models are needed to incorporate the effect of flow separation over blades. Unfortunately comparisons with measurement was not available in any of the simulated cases.

Pinon *et al.* [61] adopted an alternative approach to model the marine turbine wake. They used an unsteady Lagrangian formulation called vortex-particle method. Vorticity-velocity formation of Navier-Stokes equations were solved with a LES turbulence model. BEM theory was used to model the turbines. Computed power coefficient (C_p) curve for different tip speed ratio was validated against the previous works of Bahaj *et al.* [62].

2.4 Previous works on turbine-turbine interactions in an array

A multi-turbine array is used to extract more energy from a stream of water. As the number of turbines in the array increase, the blockage effect increases and the power available to successive turbines decreases. This creates a need for optimizing the array configuration. A better understanding of turbine wake characteristics and turbine-turbine interaction is needed for this purpose.

Colby and Adonizio [63] at Verdant Power studied the effect of turbine-turbine interaction and its effect on marine ecology. ANSYS CFX was used to model flow over multiple turbines in the New York's east river. The simulations were unable to resolve the full turbine wake and hence under-predicted the strength of wake. The numerical wake recovered completely after around 5 rotor diameters downstream whereas experiments in the field showed that they persisted much longer.

The MHK turbines in an array have also been modeled as single energy extraction points in a 2D domain [64]. James *et al.* used a modification of Environmental Fluid Dynamics Code (EFDC) developed at Sandia National Laboratories (SNL) to simulate

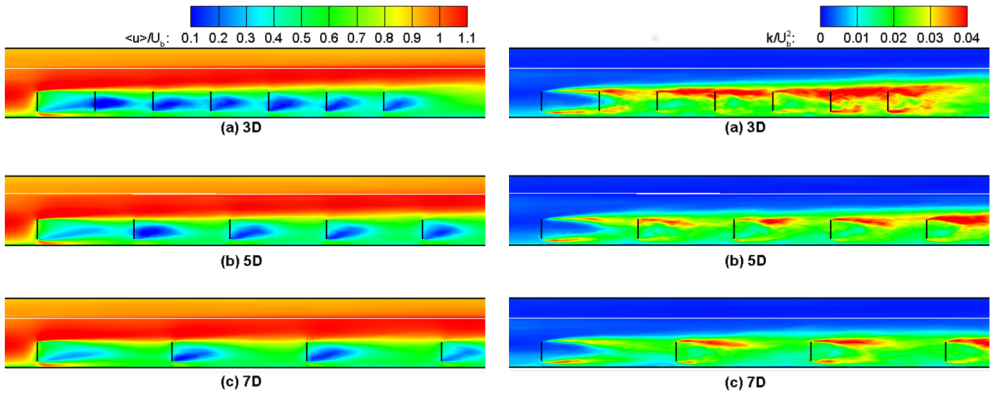

Figure 2.3: Contours of the time-averaged streamwise velocity (left) and turbulence kinetic energy(right) on the x-z plane through the center of turbines for different intra-turbine spacing. The water surface is indicated by the white line. [3]

changes to marine environment caused by array of MHK turbines. The volumetric momentum extraction rate (S_Q) by the turbine using Equation 2.2 was used with fixed thrust coefficient $C_T = 0.5$.

$$S_Q = -\frac{1}{2} C_T A_M U^2 \tag{2.2}$$

where A_M is the flow-facing area of the turbine and U is the local flow speed in a computational cell. Power extracted by the turbine was calculated using equation 2.1.

The National Wind Technology Center at NREL is working on creating a framework for simulating MHK turbine arrays in natural waterways [65]. The effects of turbulence in the incoming flow on the wake characteristics was studied in an artificial straight channel. Ten different configurations including counter-rotating and co-rotating turbines modeled as actuator discs were investigated. It was found that for non-staggered co-rotating case, increasing spacing between rows improved array performance. Staggering turbines downstream in the row also resulted in improved performance. However, the published numerical data were not verified with the experiment measurement. Bai *et al.* [66] also studied multi-row array of turbines wakes using Fluent and employing actuator disc model but no validation of the model was provided.

Yang *et al.* [3] developed a computational framework to perform LES of the MHK turbine array in natural waterways. The CURVIB method used by Kang *et al.* [29]

was implemented with actuator lines modeling the turbines. This framework, which can potentially be applied to a natural waterway, was tested with an array of MHK turbines in a straight channel flow. For the same section of the channel, a single row of turbines was simulated with different inter-turbine spacing - (a) 3D, (b) 5D and (c) 7D; where D is diameter of the turbine rotor. Figure 2.3 shows results for the three cases. Except when the intra-turbine spacing is 3D, the strength of the wake is weakest for the first turbine and strengthens as flow passes over downstream turbines. However, for 3D spacing, the strongest wake does not correspond to the last turbine. The wake is similar from turbine 3 to 6 and weakens for the last turbine. In the TKE plot, it was observed that the strength of TKE in shear layer near rotor top tip was much larger compared to that near bottom tip. This can be attributed to the wall effects of dampening some turbulence and larger shear stress near the rotor top tip [10]. TKE also increases for each successive turbine as the flow moves downstream. For 3D and 5D spacing, the power extracted by second turbine was lower than from the first turbine because of wake effects but for the 7D spacing it was slightly greater than that of the first turbine.

2.4.1 Comparison with wind turbine arrays

There is a wealth of literature in the related field of simulation of wind turbine arrays in the atmosphere [56, 57, 58]. Knowledge of turbine-turbine interaction from this literature can provide us valuable insights if used judiciously as they share a lot of similarity. However, it is important to point out that there are some fundamental differences between the two. Mayers *et al.* [67] showed that close proximity of the free surface significantly affects the wake structure downstream of the turbine. Due to the presence of sea or river-bed and at the bottom and water free-surface at the top the wake cannot be characterized as axisymmetric.

A difference which can act in favor of marine energy development at commercial scale is that, unlike wind, water flows in natural environment can be forecast with a relatively higher degree of certainty. This makes integration of MHK turbine power plants to the existing electrical grids easier. Higher water density also helps in increasing the energy extraction density for MHK turbines. Some other differences include very high Reynolds numbers, potential for cavitation and stall under water.

Chapter 3

Objectives and outlines

3.1 Objective

The review presented in the previous section indicates that there is considerable literature for a first order analysis of sites for energy resource assessment. This is a good starting point for setting up *MHK power plants*. There are also several studies quantifying the wake characteristic of the hydrokinetic turbines [62, 3, 11, 68]. Turbine turbine interactions have also been investigated in different configurations. Most of the wake characterization studies in the literature use idealized straight or curved channels. While this sheds important insights into the behavior of flow past the turbine(s), the effects of the complex interactions of turbine with the natural river environment were not incorporated. To the best of my' knowledge only O'Rourke *et al.* [44] have used a natural geometry for simulations over turbine but it was simplified to 2D and simulations were carried out without considering river bathymetry. Khosronejad *et al.* [69] have shown that the bathymetry and other features in the natural environment can give rise to complex flow dynamics specific to the environment. Other studies have also shown that the geometry of the channel, the flow conditions and the configuration of the turbines placed in the channel all dictate the amount of power generated [65, 66, 3]. Therefore in order to accurately quantify and optimize the power generation, it is important to account for the aforementioned effects.

There are several challenges that need to be addressed before field-scale high resolution 3D numerical simulation can be performed with inset turbines in natural environment. Rodriguez *et al.* [25] rightly pointed out that ample data is needed to reconstruct a model of the channel geometry as a necessary input for the simulations. Knowledge of discharge rate and velocity profiles are also essential to feed as boundary conditions to emulate the natural site. The highly dynamic nature of marine environment adds to the complexity. The flow speed in natural streams of interest are of the order of 1 m/s and the depth is of the order of tens of meters or more leading to Reynolds number of the order of millions or higher. Moreover ,the complex bathymetry and other natural and man-made structures in the stream such as rocks and boulders, riffles and pools, trunks, bridge foundations, etc. give rise to vast range of spatial and temporal flow scales making numerical simulations more challenging. While the statistical approaches of turbulence modeling like RANS are computationally less expensive, they are unable to resolve the dynamically rich coherent vortices. Coherent structure resolving turbulence modeling techniques like LES require a large grid which may require unfeasible computational time for completion. Stosser *et al.* [32] observed that "Because of the high computational cost, LES can currently only be used for lower Reynolds numbers making it not directly applicable in the river engineering practice where usually Re numbers are above 10^6 and computational domains sizes range from several hundred meters to kilometers". Other researchers [28, 29] have also acknowledged the computational challenges in dealing with natural geometries.

The present study aims at addressing some of the above challenges to make possible the high Reynolds number field scale LES of river with embedded turbines through the use of innovative computer algorithms. By using a new efficient Cartesian Unstructured mesh solver with capability to locally refine the grid, we attempt to push the limit of practical realizability for field-scale numerical simulations. We create a framework that can be used to simulate river flow over an array of MHK turbines accounting for turbine-turbine and turbine-bathymetry interactions. It is envisioned that actuator type models will be used to simulate turbines in the array simulation. Since for large arrays, use of actuator models is essential, there is a need to quantify the potential of actuator models in predicting the wake of the MHK turbines. As part of this study we will investigate the predictive capabilities of actuator models for simulating a "tri-frame"

configurations of turbine (figure 6.1) where three turbines are mounted together at the apexes of a triangular frame. Motivation for this part of study comes from the fact that turbines mounted on a tri-frame can serve as building block for rapidly deploying multi-turbine arrays in field.

The objectives of the study can be succinctly stated as 1) assess the predictive capability of actuator model in predicting the wake of the MHK turbines mounted on a tri-frame configuration; 2) develop and validate an efficient code that incorporates locally refined unstructured Cartesian meshes and immersed boundary approaches and is able to carry out LES of MHK arrays in arbitrarily complex natural channels; and 3) use the computational framework developed herein to perform a field scale LES of an array of 30 MHK turbines placed in East River of New York City.

3.2 Outline

The reminder of this thesis organized in chapters 4–9. In Chapter 4, details of numerical method used for this thesis are detailed. We describe the governing equations that are solved as well as the boundary conditions and their implementation in the numerical model. The methods used for turbulence modeling are discussed. The details of immersed boundary method used for modeling the arbitrarily complex immersed boundary method is described. We used two different types of solvers developed in-house at SAFL. Details of both solvers can be found in this chapter.

In Chapter 5, we validate the numerical models used herein using various test cases. We begin with a simple channel flow test case which is compared with the experiment. Next, the immersed boundary method is validated using flow past stationary sphere. Turbine modeling is validated by simulating wind tunnel experiments of an array of turbines. We further validate the moving immersed boundary by simulating an experiment of flow past a model hydrokinetic turbine in a water tunnel.

Following the successful validation of numerical methods, in Chapter 6, we study the flow past 3 model hydrokinetic turbines in a TriFrame arrangement. The composite wake of the 3 turbines is analyzed using high fidelity geometry resolving simulations. Both the instantaneous as well as statistically averaged flow-fields are analyzed. We discuss the role of TriFrame as a building block in constructing an array of MHK turbines.

In Chapter 7, we perform river flow simulations of a real life deployment site - East River in New York City. This simulation is performed using the bathymetry data of river obtained from a recent survey. Once we have a baseline simulation of the East River, we simulate the river with 30 inset turbines at field scale. The flow-field in the river past 30 turbines is analyzed and compared with the baseline flow.

In chapter 8 we describe the results of a study of density current formation on sloping surfaces, characteristic of dense underflow in oceans and rivers.

In Chapter 9, we conclude the thesis by summarize the findings of this work in relation to numerical challenges that were addressed in order to simulate array of MHK turbines in a site specific manner. A discussion of insights gained on deployment of MHK turbine arrays through numerical simulations is presented.

Appendix A describes the new data structures and algorithms developed for the Cartesian unstructured grid solvers that made possible the large scale simulation.

Chapter 4

Numerical Methods

This study is numerical in nature. Computational tools are employed to achieve the aforementioned objectives. Two different numerical solvers were used for the simulations discussed. Initially, simulations were performed using a legacy Navier-Stokes solver known as Virtual Flow Simulator (VFS). Details of the VFS solver are described in section 4.5 For later part of the dissertation, a newly developed unstructured grid solver is used. In this method the incompressible Navier-Stokes equations are solved on locally refined fully unstructured Cartesian grids. The implementation of this method is discussed in the section 4.6. Contributions for the development of unstructured Cartesian grid solver method were made as part of this dissertation. More specifically, contributions were towards redesigning more efficient data structures as they central for unstructured method solver (Berger and Oliger [70]); better implementation of HYPRE library Poisson solver; other algorithmic optimization crucial for performing large scale simulations in realistic time scale.

4.1 Governing Equations

For simulating fluid flow around turbines incompressibility is assumed. The Mach number in such flows remains in the incompressible range. In the environmental flows involving water as fluid, the viscosity is assumed constant and significant for most applications. Flow is considered three-dimensional and solved as unsteady in time. With these assumptions, throughout this work, 3D Navier-Stokes equations for mass

and momentum conservation are solved. The spatially-filtered form of equations for LES read as following:

$$\frac{\partial u_i}{\partial x_i} = 0 \tag{4.1}$$

$$\frac{\partial \bar{u_i}}{\partial t} + \frac{\partial u_i u_j}{\partial x_i} = -\frac{\partial p}{\partial x_i} + \frac{1}{Re}\frac{\partial^2 u_i}{\partial x_j \partial x_j} - \frac{\partial \tau_{ij}}{\partial x_j} + f_i \tag{4.2}$$

where u_i (i=1,2,3) denote the resolved Cartesian velocity components in x_i Cartesian coordinates, ρ denotes the density of fluid, p denotes resolved pressure divided by ρ, τ_{ij} denotes subgrid tensor and Re denotes the Reynolds number based on the chosen characteristic length and velocity scales for non-dimensionalization. The term f_i denotes the contribution of external body forces in the flow field. Such body force could be due to presence of real force field such as gravitational, magnetic, electric field, etc. or introduced as a result of modeling the turbines in the flow using actuator type models.

VFS method solves the spatially averaged (or filtered) Navier-Stokes equation for LES and time averaged equations for RANS in generalized curviliear coordinates. Incompressible continuity equation (4.3) and Navier-Stokes equations (4.4) transformed in generalized curvilinear coordinates can be written as:

$$J\frac{\partial U^i}{\partial \xi^i} = 0 \tag{4.3}$$

$$\frac{1}{J}\frac{\partial U^i}{\partial t} = \frac{\xi_l^i}{J}\left(-\frac{\partial}{\partial \xi^j}\left(U^j u_j\right) + \frac{1}{\rho}\frac{\partial}{\partial \xi^j}\left(\mu \frac{g^{jk}}{J}\frac{\partial u_i}{\partial \xi^k}\right) - \frac{1}{\rho}\frac{\partial}{\partial \xi^j}\left(\frac{\xi_l^j p}{J}\right) - \frac{1}{\rho}\frac{\partial \tau_{ij}}{\partial \xi^j} + F_l\right) \tag{4.4}$$

where ξ^j is the j^{th} curvilinear coordinate, J is the Jacobian of the geometric transformation, $\xi_l^i = \dfrac{\xi^i}{x_l}$ are the transformation metrics, $g^{jk} = \xi_l^j \xi_l^k$ is the contravariant metric tensor, $U^i = u_j \frac{\partial \xi^i}{\partial x_j}$ are the contravariant volume fluxes, u_i are the Cartesian velocity components, p is the static pressure divided by the density, μ is the dynamic viscosity and ρ is the density, τ_{ij} is the sub-grid stress (SGS) tensor for LES method or Reynolds stress tensor for URANS method, F_l is the body force due to forces exerted by the turbine. U^i, u_i and P are either filtered (for LES) or averaged (for URANS) quantities. Equations are expressed using Einstein's notation for tensors where repeated indices imply summation.

4.2 Turbulence Modeling

When solving the Navier-Stokes equations in a discretized domain, the discrete grid cannot resolve the flow scales smaller than the grid cells. In order to accurately capture all the relevant scales the grid resolutions requirements for a Direct Numerical Simulation (DNS) becomes very strict (grid cells smaller than Kolmogorov length scale) at higher Reynolds numbers leading to large grid sizes. Alternate approaches involve modeling the turbulent scales which are not resolved. Turbulence modeling in the VFS method can be done by using either Large Eddy Simulation (LES) or Unsteady Reynolds Averaged Navier-Stokes (URANS) method.

4.2.1 Large Eddy Simulation

In Large Eddy Simulation (LES) method of turbulence modeling, the flow scales (or eddies) smaller than a pre-determined filter size are modeled using 1 equation whereas scales larger than this filter are solved for directly. After applying a spatial filter to the Navier-Stokes equations, an additional term known as sub-grid stress term (τ_{ij}) appears in filtered momentum equations (refer to Eq. 4.4) or 4.1). The τ_{ij} term is a tenser and defined as $\tau_{ij} = \overline{u_i u_j} - \bar{u}_i \bar{u}_j$ in terms of other quantities; the over-bar on the quantities denotes the filtering operation. This definition introduces one additional equation and one new unknown term $\overline{u_i u_j}$. Hence the set of equations are still not closed. To close the set of equations, the sub-grid stress term is modeled instead. In this work, the Smagorinsky sub-grid scale model (see [71]) is used for closure of turbulence. In this model, the τ_{ij} is defined using the concept of turbulent viscosity μ_t as:

$$\tau_{ij} - \frac{1}{3}\tau_{kk}\delta_{ij} = -2\mu_t \overline{S_{ij}} \tag{4.5}$$

where δ_{ij} is Kronecker delta and $\overline{S_{ij}}$ is the filtered strain-rate tensor defined as:

$$\overline{S_{ij}} = \frac{1}{2}\left(\frac{\partial \bar{u}_i}{\partial \bar{x}_j} + \frac{\partial \bar{u}_h}{\partial \bar{x}_i}\right) \tag{4.6}$$

The eddy viscosity is equivalent to the physical viscosity working to diffuse fluid momentum of scales which are not resolved. For incompressible flow, the flow is divergence free and $\tau_{kk} = 0$. The eddy viscosity μ_t was further modeled by Smagorinsky as

$$\mu_t = C_s \Delta^2 |\overline{S}| \tag{4.7}$$

where C_s is the Smagorinsky constant, Δ is the filter size and $|\overline{S}| = \sqrt{2\overline{S_{ij}S_{ij}}}$. The present method uses box filter with the filter size as cube root of the grid local cell volume i.e. $\Delta = J^{-1/3}$

The value of Smagorinsky constant C_s can either be assumed a constant e.g. $C_s = 0.1$ suggested by Smagorinsky or calculated dynamically. A dynamic Smagorinsky constant is a better modeling technique but requires calculation of additional terms in order to determine C_s. In the dynamic Smagorinsky modeling technique, the constant C_s is dynamically calculated for each instance in time and space using method of Germano *et al.* [31]. Germano proposed that the C_s is related to the smallest scale that is resolved in a local region. C_s is calculated locally using with the help of a *test filtering* operation. The filtered Navier-Stokes equations are further passed through a test filter giving rise to a Leonard term:

$$L_{ij} = \widehat{\overline{u_i}\overline{u_j}} - \hat{\overline{u}}_i\hat{\overline{u}}_j \tag{4.8}$$

where the hat symbol operator $\widehat{(\ )}$ denotes the test filtering operation. The Smagorinsky constant is then calculated using the test filtered velocities as following:

$$C_s = \frac{L_{ij}M_{ik}G_{jk}}{M_{np}M_{nq}g_{pq}} \tag{4.9}$$

$$M_{np} = 2\Delta^2\widehat{\overline{S}_p|\overline{S}|} - 2\hat{\Delta}^2\bar{S_n}p|\hat{\overline{S}}| \tag{4.10}$$

where $\hat{\Delta}$ is the test filter size, and g_jk is the covariant metric tensor for cuvilinear coordinates. For unstructured Cartesian grid solver, g_jk is set to identity. Setting test filter size as twice the size of grid filter is an acceptable practice and provides consistent results. C_s is calculated at cell centers in the above equations and then interpolated at the cell faces using linear interpolation.

4.2.2 URANS

For URANS turbulence model the time averaged equations are give in Eq. (4.3 and 4.4). τij term represents the Reynolds stress tensor which is modeled using Boussinesq hypothesis:

$$\tau_{ij} = -2\mu_t\widetilde{S_{ij}} + \frac{2}{3}\rho k\delta_{ij} \tag{4.11}$$

where $\widetilde{S_{ij}}$ is the Reynolds averaged strain-rate tensor, μ_t is eddy viscosity, k is the turbulent kinetic energy and δ_{ij} is the Kronecker delta. μ_t is obtained using $k-\omega$ model of Wilcox [72] to close the equations. The closure equations of this models are:

$$\frac{1}{J}\frac{\partial(\rho k)}{\partial t}+\frac{\partial}{\partial \xi^j}\left(\rho k U^j\right)=\tau_{ij}\frac{\xi_j^k}{J}\frac{\partial u_i}{\partial \xi^k}-\frac{1}{J}\beta^*\rho k\,\omega+\frac{\partial}{\partial \xi^j}\left(\left(\mu+\sigma^*\mu_t\right)\frac{g^{jk}}{J}\frac{\partial k}{\partial \xi^k}\right) \tag{4.12}$$

$$\frac{1}{J}\frac{\partial(\rho\,\omega)}{\partial t}+\frac{\partial}{\partial \xi^j}\left(\rho\,\omega U^j\right)=\alpha\frac{\rho\omega}{k}\tau_{ij}\frac{\xi_j^k}{J}\frac{\partial u_i}{\partial \xi^k}-\frac{1}{J}\beta\rho\,\omega^2+\frac{\partial}{\partial \xi^j}\left(\left(\mu+\sigma^*\mu_t\right)\frac{g^{jk}}{J}\frac{\partial\,\omega}{\partial \xi^k}\right) \tag{4.13}$$

$$\mu_t=\rho k/\omega \tag{4.14}$$

where the values of closure coefficients are specified as $\alpha=5/9$, $\beta=3/40$, $\beta^*=9/100$, $\sigma=1/2$ and $\sigma^*=1/2$.

4.3 Boundary Conditions

At the free surface of the flow, a rigid lid assumption is made. The shape of the free surface is prescribed *a priori* from the experiments. This assumption holds for low Froude numbers. Mathematically the condition is expressed as follows:

$$\frac{\partial u_i}{\partial n_j}s_j=0 \tag{4.15}$$

$$u_j\,n_j=0 \tag{4.16}$$

where s_j denotes tangential and n_j denotes normal directions to the free surface respectively. At rigid walls, the velocity boundary conditions depend on the grid resolution near the wall. If the grid is fine enough such that the first off-wall grid node lies in the laminar sub-layer of the boundary layer then a no-slip boundary condition (Eq. 4.17) is applied.

$$u_i=0 \tag{4.17}$$

This is often the case with low Reynolds number flows when we can sufficiently resolve the wall. In other cases a model, described in the following sub-section, is used.

4.3.1 Wall model

For cases with very high Reynolds number the laminar sub-layer of boundary layer is very thin. To have a grid point which will extend in this sub-layer will require many more grid points and hence, is computationally expensive. To circumvent this problem, a wall modeling approach is used for rough or smooth walls [73]. Shear stress boundary condition and no flux boundary conditions are used for tangential and normal velocity components respectively. To calculate shear stress at a rough wall, the rough-wall log-law [74] is used:

$$\frac{u_s}{u_*} = \frac{1}{\kappa} \log\left(\frac{x_3}{z_0}\right) \tag{4.18}$$

In the above equation, u_s is the tangential velocity, u_* is the shear velocity, $\kappa = 0.4$ is von Kármán constant, x_3 is the wall-normal direction and z_0 is the roughness height of the bed. The velocity at the second off-grid node is known from solution and is used to obtain u_* from equation 4.18. The two components of wall shear stress - streamwise (τ_{wall,x_1}) and spanwise (τ_{wall,x_2}) - are obtained as:

$$\tau_{wall,x_i} = \frac{u_i}{u_s} \rho u_*^2 \qquad (i = 1, 2) \tag{4.19}$$

where u_i is the velocity at second off-wall grid node and $u_s = \sqrt{u_1^2 + u_2^2}$ is the tangential component of velocity at the same point.

The smooth walls are treated in a similar fashion, the only difference being instead of equation 4.18 the smooth wall power law equation is used:

$$\frac{u_s}{u_*} = 8.3\left(\frac{x_3\, u_*}{\nu}\right)^{\frac{1}{7}} \tag{4.20}$$

4.3.2 Boundary condition for $k - \omega$ equations

For cases with low Reynolds number, when wall is resolved and first grid point lies in laminar sub-layer, following conditions are applied at the boundaries [72]:

$$k = 0 \tag{4.21}$$

$$\omega = \frac{6\mu}{\rho\beta d^2} \tag{4.22}$$

where d is the distance of first grid point from the wall. If the first grid point lies in the log-layer of boundary layer following conditions are applied [72]:

$$k = \frac{u_\tau^2}{\sqrt{\beta^*}} \tag{4.23}$$

$$\omega = \frac{u_\tau}{\sqrt{\beta^*}\kappa d} \tag{4.24}$$

where $\kappa = 0.4$ is the von Kármán constant and u_τ the is shear velocity other variables being as described earlier.

4.4 Actuator line model for axial turbines

In performing simulations of axial turbines, the most accurate methodology is when the full geometry of turbine including the blades and nacelle are resolved with very fine grids. Alternative approach is to parameterize the turbine geometry using a model to mimic the forces in the flow. Actuator models – actuator disk, actuator line or actuator surface model – model the force exerted by the rotating turbine blades on the fluid. All three models have been used to study wind and hydrokinetic turbines [11, 75, 8, 76, 77, 78, 3]. Such modeling approaches significantly reduce the computational cost of simulations compared to immersed boundary method of representing turbines at the expense of accuracy. In this dissertation, the actuator line model is used to parameterize the axial turbines for some of the simulations. The details of modeling approach is as follows.

In the actuator line model the blades of the turbine are represented by line forces in the flow. A one-dimensional line mesh is introduced for each blade of the turbine rotor. Forces are calculated on the line mesh based on the velocity field upstream of the turbine and the two-dimensional airfoil characteristic of the turbine rotor blade. The drag C_D and lift C_L coefficients define the airfoil characteristic of the blades. Additionally, local pitch angle is defined for the rotor blade construction of the turbine in question, as an input to actuator lines. In Fig. 4.1 (a), the cross-sectional airfoil element at radius r in the (θ,z) plane indicates that the local relative velocity U_{rel} and the local angle of attack α can be calculated from the velocity triangle as:

$$U_{rel} = \sqrt{U_x^2 + (U_\theta - \omega r)^2} \tag{4.25}$$

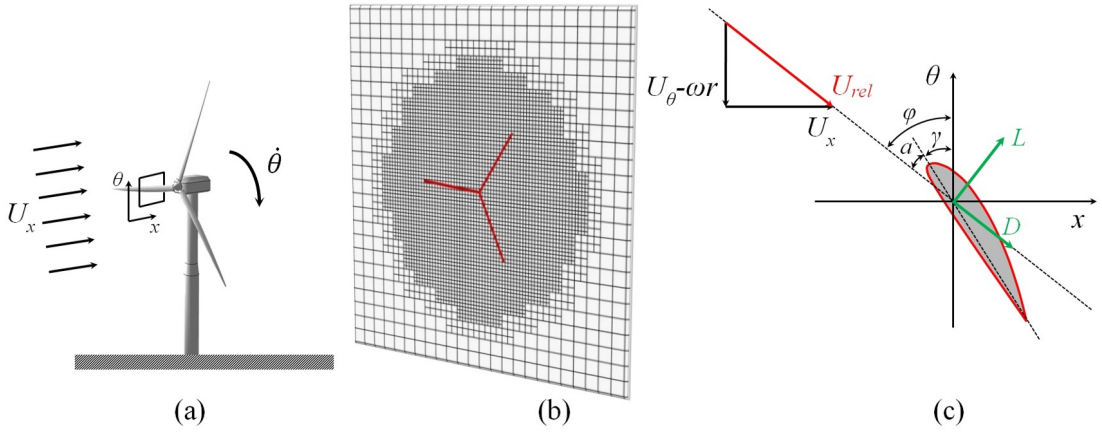

Figure 4.1: Schematic representation of the actuator line model. (a) Sketch of a turbine and a two dimensional section of the blade. (b) Actuator lines immersed within an unstructured Cartesian mesh used to represent the blades of a turbine. (c) Velocity and force analysis with respect to the axial and tangential coordinates. [4]

$$\alpha = \phi - \gamma \tag{4.26}$$

$$\phi = atan\left(\frac{U_x}{U_\theta - \omega r}\right) \tag{4.27}$$

where ω is the angular velocity rotating turbine, U_θ is the tangential velocity component, U_x is the axial velocity component, γ is local pitch angle of the rotor blade and ϕ the angle between the relative velocity and the rotor plane (Fig. 4.1c). In the present implementation of the actuator line method, the cell centered Cartesian velocity values are interpolated on the actuator line (ee Fig. 4.1b) using a 3-point smoothed discrete delta function [79]. Considering that the lift, C_L, and drag, C_D, coefficients are function of the angle of attack, α, the lift L and drag D forces, per chord length c, can be calculated after having projected the velocity field along the actuator line grid points:

$$L = c\frac{1}{2}C_L(\alpha)\rho\ U_{rel}^2 \tag{4.28}$$

$$D = c\frac{1}{2}C_D(\alpha)\rho\ U_{rel}^2 \tag{4.29}$$

4.5 The Virtual Flow Simulator (VFS) method

4.5.1 The Fractional Step Method

The governing equations 4.3 and 4.4 are solved using the second order time accurate implicit fractional step method of Ge and Sotiropoulos [30]. In this method left hand side (LHS) of momentum equation is discretized fully implicitly using a second-order backward difference scheme in time as follows:

$$\frac{1}{J}\frac{U^* - U^{n-1}}{\Delta t/2} = RHS\left(U^*, u^*\right) \tag{4.30}$$

where superscripts n and $n-1$ denote the time-step levels and RHS is the right hand side of the momentum equation 4.4. The advective and diffusion terms in the RHS are descritized using the second-order accurate central difference scheme on a hybrid staggered/non-staggered grid. The velocity field solution thus obtained by solving this equation U^* is not guaranteed to be divergence free since the continuity equation was not imposed as of yet. In the fractional step method, a divergence free condition is imposed in the next step in the form of Poisson equation for pressure correction variable $\phi = p^{n+1} - p^n$ as follows:

$$-J\frac{\partial}{\partial\xi_i}\left(\frac{1}{\rho}\frac{\xi_l^i}{J}\frac{\partial}{\partial\xi_j}\left(\frac{\xi_l^j\phi}{J}\right)\right) = \frac{3}{2\Delta t}J\frac{\partial U_j^*}{\xi_j} \tag{4.31}$$

Following the solution of the above Poisson equation the velocity field and pressure are projected, using equations 4.32 and 4.32, to obtained a divergence free velocity field satisfying both momentum and continuity equations.

$$p^{n+1} = p^n + \phi \tag{4.32}$$

$$U_i^{n+1} = U_i^* - J\frac{2\Delta t}{3}\frac{1}{\rho}\frac{\xi_l^i}{J}\frac{\partial}{\partial\xi_j}\left(\frac{\xi_l^j\phi}{J}\right) \tag{4.33}$$

4.5.2 Iterative Solvers

In the above discretization method there are two equations that need to be solved numerically. Iterative solvers implemented in PETSc (Portable, Extensible Toolkit for Scientific Computation) library are used for both equations. Generalized Minimal Residual(GMRES) method is used to solve the linear system for the pressure correction

Poisson equation 4.31. Algebraic multigrid (AMG) is used as a preconditioner for the GMRES method to accelerate the convergence (see [29] for details). The non-linear discrete momentum equation 4.30 is solved using matrix-free Newton-Krylov method. The inner iterations of the Newton-Krylov solvers also use GMRES method but without preconditioning. Because of the equations are solved in fully implicit manner the numerical scheme does not impose any CFL (Courant-Friedrichs-Lewy) restriction. The code is efficiently parallelized using PETSc library and MPI (Message Passing Interface) to exploit massively parallel computer clusters.

4.5.3 Curvilinear immersed boundaries method

The VFS code incorporates the CURVilinear Immersed Boundary (CURVIB) method which is a sharp interface immersed boundary method capable of simulating arbitrarily complex geometries. The complex body is immersed in the mesh discretizing the background domain. All the points in the mesh are classified as either fluid nodes, solid nodes or Immersed Boundary (IB or Interface) nodes (See Fig. 4.2). The boundary conditions on the solid nodes are defined by the type of motion of the solid body. Boundary condition at IB nodes are obtained by interpolation using neighboring solid and fluid nodes. Interpolation can be linear or quadratic, for grids sufficiently fine to resolve the viscous sublayer, or utilize a wall model approach for high Reynolds number simulations.

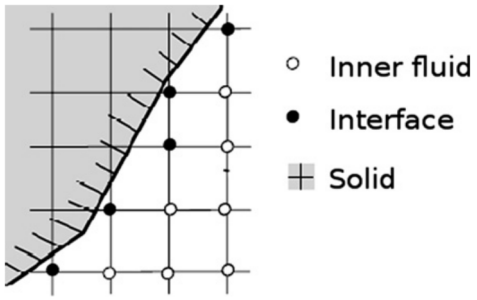

Figure 4.2: Sharp interface immersed boundary method [5].

4.6 Cartesian Unstructured Grid Solver

Subsection are adapted from journal article Angelidis, D., Chawdhary, S., & Sotiropoulos, F. (2016). Unstructured Cartesian refinement with sharp interface immersed boundary method for 3D unsteady incompressible flows. Journal of Computational Physics, 325, 272–300.

River flows are characterized by broad range of scales in different regions of the reach under consideration. Presence of in-stream structures of different length scales - channel geometry is of order of 10m, turbine blades are few meters, bed characteristics at cm scale - in the flow domain further distorts the spatial and temporal flow scales. LES is best suited for simulating such flows because it directly resolves the large energy containing eddies while modeling only the smaller scale eddies. In spite of this decided advantage it is not always possible to perform field scale LES because at high Reynolds number very fine grid resolution is required. As an example, consider a 20m deep, 200m wide and 1km long stretch of river with 5m diameter turbine and a bridge pier of 1m diameter. In order to resolve the coherent structures using LES from the turbine blades, at least 40 points per diameter is needed. A good quality uniform grid for flow domain with this resolution will run upto 2 billion grid points. The grid size, however, is limited by computational power. To optimize the use of computational resources and enable multi-resolution calculations, in this work the unstructured Cartesian flow solver, developed in [4]. The main features of the algorithm are described below.

4.6.1 Grid topology

In order to perform calculation on unstructured flow solvers connectivity between cells should be established. If a reference cell is assumed to be located in the middle of a Rubik's cube (Fig. 4.3a,b), the surrounding cells represent neighbors if thus cell. Hence, we can locally define the mesh topology on locally structured grids. If this idea is extended to multi-resolution grids, all the 27 cells of the Rubik's cube can be considered as *hyper-cells* and they can be further refined. By doing so, a locally structured $3 \times 3 \times 3$ mesh may describe the position of any hyper-cell and we can readily access any refined component of a hyper-cell that may be called *sub-cell*. In order to achieve smooth transition between the levels of refinement and maintain algorithmic simplicity, the

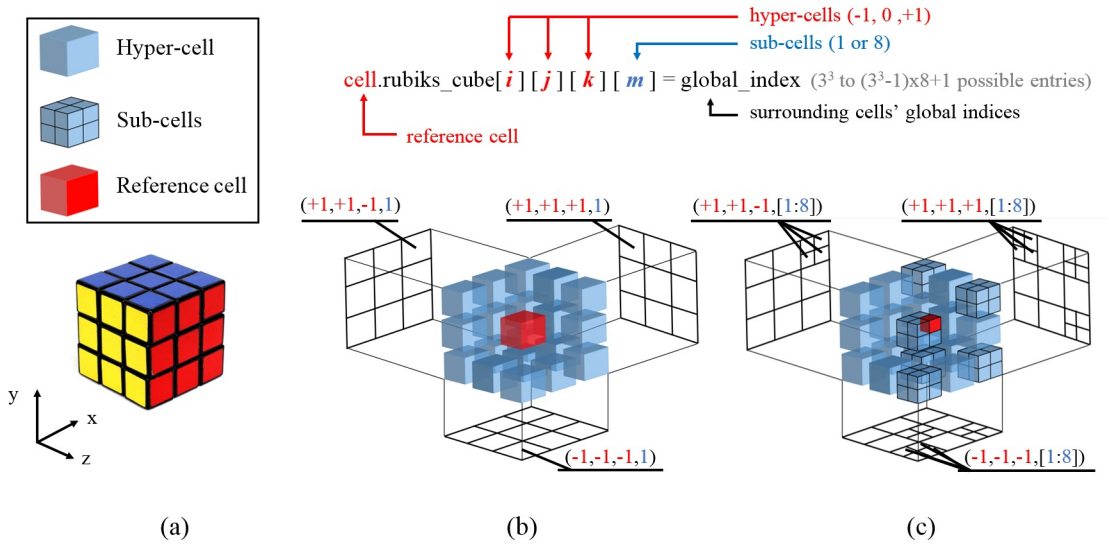

Figure 4.3: The Rubik's cube analogy employed to describe the grid's topology around a reference cell: (a) Rubik's cube; (b) grid's topology without refinement and (c) grid's topology with refinement.

allowed difference between the refinement level of the hyper-cells cannot be larger than one. The structure *cell* in our method contains any information needed to define local or global indices regarding the local grid topology. In this way, any local or global indices can be easily obtained by using a structure like $cell.rubiks\_cube[i][j][k][m]$ where i, j, k=$\{-1, 0, 1\}$ indicate the position of a hyper-cell and $m \in [1, 8]$ the corresponding sub-cells, if any (Fig. 4.3c). It should be noted that the total number of cells included in the $3 \times 3 \times 3$ hyper-cells is the maximum information needed to generate the support stencil needed for all the calculations.

To manage the unstructured staggered arrangement, global indices are defined at the cell centers as well as the face centers. Whenever neighboring cells have different levels of refinement, face indices are defined for the four smaller faces. The adopted monolithic single-block arrangement enables straightforward partition of the computational domain, which is crucial to achieve load balance and control the scalability potential of the solver. All the variables of the staggered arrangement are stored in one-dimensional vectors and the parallelization of the calculations is achieved by distributing the vectors in accordance to the domain decomposition. The adjacency list of the unstructured grid

is modified every time the grid topology is changing and is provided to the partitioner for domain decomposition.

4.6.2 Lagrange reconstruction around cells of varying resolution

The descritization procedure in the vicinity of cells surrounded by other cells with different levels of resolution, is facilitated by using hanging nodes and Lagrange interpolation formula. Provided that the Lagrange basis polynomials can be described as:

$$L_i(\omega) = \prod_{s=0, s\neq 1}^{n_\omega} \frac{\omega - \omega_s}{\omega_i - \omega_s}, 0 \leq i \leq n_\omega \tag{4.34}$$

where ω can be any Cartesian coordinate ξ, η and $(n_\omega + 1)$ is the number of data points, the 1D interpolation can be defined as:

$$\phi(\xi) = \sum_{i=0}^{n_\xi} f(\xi_i) L_i(\xi) \tag{4.35}$$

the 2D interpolation will be:

$$\phi(\xi, \eta) = \sum_{i=0}^{n_\xi} \sum_{j=0}^{n_\eta} f(\xi_i, \eta_j) L_i(\xi) L_j(\eta) \tag{4.36}$$

The above Lagrange interpolant polynomials interpolate $(n_\xi{+}1)$ or $(n_\xi{+}1){\times}(n_\eta{+}1)$ data points $f(\xi_i)$ or $f(\xi_i, \eta_j)$ respectively. Essentially, the interpolated values derived from the Lagrangian basis polynomials constitute a correlation between weighting factors and the information from the data points.

Second order accurate interpolations are performed by utilizing the 1D Lagrange formula on a three-point stencil which results in a quadratic reconstruction and perform 2D Lagrange interpolation on a 3×3 stencil resulting in a bi-quadratic quadrilateral reconstruction. Thus, the equivalent polynomial reconstruction of the Lagrangian interpolations enables the definition of weighting factors when points of the reconstruction stencil lie along the boundaries of the domain governed either by Dirichlet or Neumann conditions. For this reason, the 2D Lagrange interpolation may also be expressed as:

$$\phi(\xi, \eta) = \sum_{i=0}^{n_\xi} \sum_{j=0}^{n_\eta} f(\xi_i, \eta_j) w_{ij}(\xi, \eta) \tag{4.37}$$

and the 2D Lagrange operator can be defined as:

$$\mathcal{S}(.) = \sum_{i=0}^{n_\xi} \sum_{j=0}^{n_\eta} (.)_{\xi_i,\eta_j} w_{ij}(\xi,\eta) \tag{4.38}$$

Around any reference cell, 3×3 support stencils can be formed from the cell centered values of the surrounding hyper-cells, which are coplanar and parallel to its six faces (Fig. 4.3). However, if the hyper-cells are split then the hyper-cells' centered values are obtained by performing averaging from the cell centered values of the corresponding isotropically refined cells, which essentially represents trilinear interpolation on uniform stencils. When all the neighboring cells have the same level of refinement, three-point central finite difference formulas can be readily used. Near cells with varying grid resolution, however, a different approach needs to be employed.

A differencing operator δ_ξ will now be of the following general form:

$$\delta_\xi(.)_i = \frac{c_0\mathcal{S}(.)_{i+1} + c_1\mathcal{S}(.)_{i-1} + c_2\mathcal{S}(.)_{i-2}}{\Delta\xi} + O(\Delta\xi^2) \tag{4.39}$$

with c_0, c_1, $c_2 = g(h_{i+1}, h_{i-1}, h_{i-2})$ is used. C_0, C_1 and C_2 are calculated by performing Taylor expansion around h_i+1, h_i-1, h_i-2. The latter equation enables the calculation of $f^{'}$ with 2^{nd} order accuracy in the middle of faces adjacent to cells with varying grid resolution. This is feasible by using 1D non-uniform stencils and ghost nodes, which will be explained in a following paragraph.

4.6.3 The unstructured hybrid staggered/non-staggered grid layout

A 3D unstructured hybrid staggered/non-staggered grid layout facilitates the satisfaction of the discrete divergence free constraint and simplify the imposition of boundary conditions in the context of the immersed boundary method. The idea of the hybrid staggered/non-staggered approach was initially proposed by [80, 81] but was restricted to structured Cartesian grids. However, the discretization of the governing equations and the employment of the fractional step method on a hybrid unstructured layout requires utilization of hanging nodes. In this work, the velocity components normal to the cell faces are located in the middle of the shared cell surfaces while the pressure is stored at the cell centers. Even though for every cell the pressure is stored at its center, the velocity components to be calculated are located in the middle of the shared faces

and their number depend on the level of refinement of the adjacent cells, as shown in Fig. 4.4. Hence, one cell may be governed by 6 to 24 normal velocity components. The hybrid formulation enables the satisfaction of both the continuity equation and the momentum equations on arbitrarily refined cells, avoiding at the same time odd-even decoupling of the pressure nodes.

Even though fully unstructured grid arrangement is adopted in this work, for clarity we assume that a computational cell adopt a locally structured grid indexing system (i,j,k), as shown in Fig. 4.4. The continuity equation (Eq. 4.1) is discretized by integrating it over control volumes of the unstructured grid. If we assume that the total number of the shared faces of each side ($l \pm \frac{1}{2}$), (l=i,j,k) of a reference cell, p, is $N_{Faces}\big|_{l\pm\frac{1}{2}}$, the discrete divergence operator over the cell will be:

$$\mathcal{D}(\mathbf{u}) = vol\left(\frac{\sum_{N=1}^{N_{Faces}\big|i+\frac{1}{2}} (u_1)_{\left(i+\frac{1}{2}\right)_N} S_{\left(i+\frac{1}{2}\right)_N} - \sum_{N=1}^{N_{Faces}\big|i-\frac{1}{2}} (u_1)_{\left(i-\frac{1}{2}\right)_N} S_{\left(i-\frac{1}{2}\right)_N}}{\Delta x \sum_{N=1}^{N_{Faces}\big|i+\frac{1}{2}} S_{\left(i+\frac{1}{2}\right)_N}} + \ldots\right) = 0 \tag{4.40}$$

where vol is the control volume, $S_{\left(l\pm\frac{1}{2}\right)_N}$, $N = 1, N_{Faces}\big|_{l\pm\frac{1}{2}}$ represent the area of the shared faces and $\mathbf{u}_{\left(l\pm\frac{1}{2}\right)N}$ the corresponding face centered Cartesian velocity components.

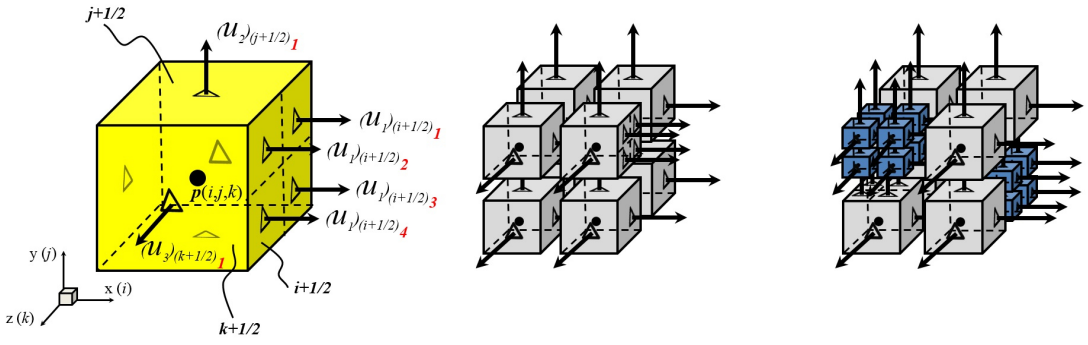

Figure 4.4: Hybrid staggered/non-staggered grid layout on unstructured Cartesian grids. • Cell centered values of pressure or the reconstructred velocity components; △ face centered normal velocity components. [4]

As mentioned above, to avoid odd-even decoupling of the pressure nodes and facilitate the discretization procedure, the normal to the cell faces velocity components are calculated in the middle of the shared faces of the unstructured mesh and the three velocity components are then reconstructed at the cell centers. The velocity field can be calculated at the cell centers from the cell face Cartesian velocity components by averaging the corresponding volume fluxes and dividing by the corresponding normal surface area. For instance, the reconstruction of the Cartesian velocity component (u_1) is accomplished as follows:

$$(u_1) = \frac{\sum_{N=1}^{N_{Faces}\left|i+\frac{1}{2}\right.} (u_1)_{(i+\frac{1}{2})N} S_{\left(i+\frac{1}{2}\right)_N} + \sum_{N=1}^{N_{Faces}\left|i-\frac{1}{2}\right.} (u_1)_{(i-\frac{1}{2})N} S_{\left(i-\frac{1}{2}\right)_N}}{2 \sum_{N=1}^{N_{Faces}\left|i-\frac{1}{2}\right.} S_{\left(i-\frac{1}{2}\right)_N}} \tag{4.41}$$

and similarly the (u_2), (u_3) components are determined by interpolating along their perspective Cartesian directions. Having calculated the Cartesian velocity components at the cell centers, discretization schemes can be implemented in the same manner as in collocated grids, as explained below.

The momentum equations (4.2) can be formulated in a discrete operator form as follows:

$$\frac{\partial u_j}{\partial t} = -\mathcal{A}(u_j) - \mathcal{G}_j(p) \tag{4.42}$$

where $\mathcal{G}$ is the pressure gradient operator and $\mathcal{A}$ is a summation of the convective $\mathcal{C}$ and viscous $\mathcal{V}$ operators:

$$\mathcal{A}(.) = \mathcal{C}(.) - \frac{1}{Re}\mathcal{V}(.) \tag{4.43}$$

which are defined as:

$$\mathcal{C}(.) = \frac{\partial}{\partial x_i}(u_i.) \tag{4.44}$$

and

$$\mathcal{V}(.) = \frac{\partial}{\partial x_i}\left(\frac{\partial}{\partial x_i}.\right) \tag{4.45}$$

respectively. The pressure gradient operator is calculated by using the differencing operator δ_ξ, defined in (4.39), as follows:

$$\mathcal{G}_j(p) = \delta_{x_j}(p) \tag{4.46}$$

For instance, discretizing the x momentum equation in the middle of the $N{=}1,N_{Faces}\big|_{i+\frac{1}{2}}$ shared faces of the unstructured mesh (Fig. 4.4), we obtain the following semi-discrete form at $(i{+}\frac{1}{2})$:

$$\left.\frac{\partial u_1}{\partial t}\right|_{\left(i+\frac{1}{2}\right)_N} = -\mathcal{A}(u_1)\Big|_{\left(i+\frac{1}{2}\right)_N} - \mathcal{G}_1(p)\Big|_{\left(i+\frac{1}{2}\right)_N} \tag{4.47}$$

The $\mathcal{G}_1(p)\Big|_{\left(i+\frac{1}{2}\right)_N}$ term is the differencing operator (Eq. 4.39) applied to calculate the pressure gradient at the faces. Essentially, the 2D Lagrangian operator (Eq. 4.38) is used to calculate the pressure values at hanging nodes, from cell centered values of the hyper-cells, and subsequently, a second order accurate derivative is calculated on a three-point stencil of collinear points (Eq. 4.39). In this case, the hanging nodes are located at the normal intersection of a line passing from the center of the finer cell and a plane passing from the center of mass of hyper-cells, that constitute a 3×3 stencil which is parallel to the calculation face. Additionally, assuming that the $\mathcal{A}_{i,j,k}$ terms have been calculated at all the cell centers, the above mentioned three-point stencil can also be utilized to perform 1D Lagrange interpolation (Eq. 4.35) and calculate the terms $\mathcal{A}$ at the perspective surfaces.

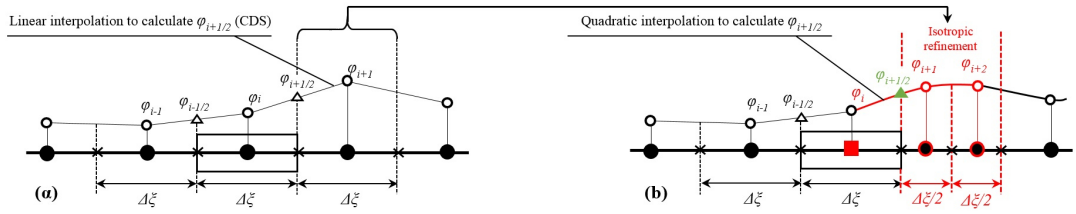

Figure 4.5: One dimensional representation of the discretization scheme employed when a reference cell is adjacent to other cells of a) Equal and b) Varying refinement levels. • Cell centered values; ■ cell centered values (1D) or values at hanging nodes (2D or 3D); ▲ calculations in the middle of the shared surfaces between neighboring cells of varying refinement levels.

Concerning the spatial discretization of the convective terms in the momentum equation, we are using the conventional cell-centered based second-order central differencing scheme (CDS) when the support stencil includes cells of equal grid resolution. This approach has been successfully utilized in the CURVIB solver where the hybrid staggered/non-staggered was adopted [81, 82, 8]. However, to control the level of accuracy when discretizing the governing equations around arbitrarily refined cells, hanging nodes are used and the conventional second-order central differencing scheme is modified. To calculate the convective flux of a dependent variable, ϕ, in the middle of shared surfaces from cells with varying grid resolution, a 1D three-point stencil is used to perform quadratic interpolation (Fig. 4.5). By doing so, the convected variable ϕ is calculated on a non-uniform stencil with second order accuracy and strong coupling between coarse/fine interfaces is achieved.

The convection term (Eq. 4.44) of a variable ϕ for the first velocity component u_1, for example, is discretizated on a hybrid staggered/non-staggered layout when using a second-order central differencing scheme, as follows:

$$\mathcal{C}(\phi)\Big|_{i+\frac{1}{2}} = \frac{1}{2}\frac{\partial}{\partial\xi}(u_1\phi)\Big|_i + \frac{1}{2}\frac{\partial}{\partial\xi}(u_1\phi)\Big|_{i+1} \tag{4.48}$$

with

$$\frac{\partial}{\partial\xi}(u_1\phi)\Big|_i = (u_1)_{i+\frac{1}{2}}\frac{\phi_{i+1}+\phi_i}{2\Delta\xi} - (u_1)_{i-\frac{1}{2}}\frac{\phi_i+\phi_{i-1}}{2\Delta\xi} \tag{4.49}$$

In the general case when a cell i of level L^i and grid spacing $\Delta\xi$ is adjacent to the refined cells $i+1$ and $i+2$ of level L^{i+1} and grid spacing $\frac{1}{2}\Delta\xi$, the semi-discrete convective term is calculated as follows:

$$\mathcal{C}(\phi)\Big|_{i+\frac{1}{2}} = \frac{\partial}{\partial\xi}(u_1\phi)\Big|_i L_0 + \frac{\partial}{\partial\xi}(u_1\phi)\Big|_{i+1} L_1 + \frac{\partial}{\partial\xi}(u_1\phi)\Big|_{i+2} L_2 \tag{4.50}$$

where $L = L_k(\xi)$, $k = 0, 2$ the Lagrange basis polynomials (Eq. 4.34) which apply quadratic interpolation on the three-point stencil. The cell centered convective terms for the cell i, is calculated as:

$$\frac{\partial}{\partial\xi}(u_1\phi)\Big|_i = \frac{(u_1)_{i+\frac{1}{2}}\phi_{i+\frac{1}{2}} - (u_1)_{i-\frac{1}{2}}\phi_{i-\frac{1}{2}}}{\Delta\xi} \tag{4.51}$$

The values of $\phi_{i-\frac{1}{2}}$ and $\phi_{i+\frac{1}{2}}$ are determined with linear interpolation from the neighboring cells if they have the same resolution and can form uniform stencil or with quadratic interpolation otherwise. For instance, if the cells $i-2$, $i-1$, i have the same refinement level, L^i and the cells $i+1$ and $i+2$ are refined cells with L^{i+1} (Fig. 4.5) we get:

$$\left.\frac{\partial}{\partial\xi}(u_1\phi)\right|_i = \frac{(u_1)_{i+\frac{1}{2}}(L_0\phi_i + L_1\phi_{i+1} + L_2\phi_{i+2}) - (u_1)_{i-\frac{1}{2}}\left(\frac{1}{2}\phi_i + \frac{1}{2}\phi_{i-1}\right)}{\Delta\xi} \tag{4.52}$$

To calculate the viscous terms $\mathcal{V}$ (Eq. 4.45), the above mentioned approach extended with the use of hanging nodes, Lagrange interpolation (Eqs. (4.35), (4.38)) and the second order differencing operator of Eq. (4.39). The viscous terms are calculated at the cell centers and subsequently interpolated in the middle of the shared surfaces, procedure described above. The semi-discrete cell centered viscous term for the (u_1) component of the momentum equation can be written as:

$$\begin{aligned}\left.\mathcal{V}(u_1)\right|_{i,j,k} = \frac{\partial}{\partial x_i}\left(\frac{\partial}{\partial x_i}(u_1)\right) =& \frac{\left.\frac{\partial u_1}{\partial x_1}\right|_{i+\frac{1}{2},j,k} - \left.\frac{\partial u_1}{\partial x_1}\right|_{i-\frac{1}{2},j,k}}{\Delta x_1} + \frac{\left.\frac{\partial u_1}{\partial x_2}\right|_{i,j+\frac{1}{2},k} - \left.\frac{\partial u_1}{\partial x_2}\right|_{i,j-\frac{1}{2},k}}{\Delta x_2} \\ &+ \frac{\left.\frac{\partial u_1}{\partial x_3}\right|_{i,j,k+\frac{1}{2}} - \left.\frac{\partial u_1}{\partial x_3}\right|_{i,j,k-\frac{1}{2}}}{\Delta x_3}\end{aligned} \tag{4.53}$$

and similarly the $\mathcal{V}(u_2)$, $\mathcal{V}(u_3)$ components are obtained. More details about the discretization can be found in [4].

4.6.4 Time integration method

The fractional step algorithm is outlined as follows. The momentum equations are solved implicitly discretized in time via the second order accurate backward Euler differencing scheme:

$$\frac{3\mathbf{u}^* - 4\mathbf{u}^n + \mathbf{u}^{n-1}}{2\Delta t} = -\frac{\nabla p^n}{\rho} - \mathbf{u}^*\nabla\mathbf{u}^* + \frac{1}{Re}\nabla^2\mathbf{u}^* \tag{4.54}$$

where n denotes the time step and $\mathbf{u}^*$ represents the intermediate staggered velocity field, which does not satisfy the continuity equation. The right hand side of the above equation is discretized in space according to the hybrid staggered/non-staggered approach described. The pressure correction step is employed to enforce satisfaction of

the continuity equation at the time step $n+1$:

$$-\frac{3\rho(\mathbf{u}^{n+1}-\mathbf{u}^{*})}{2\Delta t}=\nabla\Pi^{n} \tag{4.55}$$

$$\nabla\mathbf{u}^{n+1}=0 \tag{4.56}$$

and the pressure correction, Π:

$$\Pi=p^{n+1}-p^{n} \tag{4.57}$$

can be obtained by the Poisson equation resulted by the combination of the Eqs. (4.55) and (4.56):

$$\nabla^{2}\Pi=\frac{3\rho\nabla\mathbf{u}^{*}}{2\Delta t} \tag{4.58}$$

The velocity field that satisfies the continuity equation is then obtained as follows:

$$\mathbf{u}^{n+1}=\mathbf{u}^{*}-\frac{2\Delta t\nabla\Pi}{3\rho} \tag{4.59}$$

The Jacobian-free Newton-Krylov method is employed to solve the momentum equation in a fully implicit manner. The discretization of pressure (Eq. 4.46) following the strong coupling approach, leads to the generation of a non-symmetric sparse matrix. For this reason, the Algebraic Multi-Grid (AMG) serves as the preconditioner to accelerate the convergence rate of the Newton-Krylov solver when solving the Poisson equation (Eq. 4.58).

4.7 Sharp interface immersed boundary method on adaptively refined meshes

In this work, the local grid refinement of the background mesh is applied in the vicinity of immersed boundaries to improve the accuracy of the calculations with low computational cost. Algorithmically, the sharp interface immersed boundary method involves two steps: a) The grid node classification and b) the reconstruction of the velocity and pressure fields and imposition of appropriate boundary conditions in the immediate vicinity of the immersed body [80, 82].

According to the present approach, the governing equations are discretized on a background grid which does not conform to the physical boundaries of the immersed bodies. For this reason, the cell centered nodes of the background unstructured mesh are classified as either *solid*, IB (immersed boundary) or $fluid\ nodes$, as required by the sharp-interface immersed boundary method. The solid nodes are the nodes which are located inside the body and are excluded from the calculations. The IB nodes are in the immediate vicinity but exterior to the body and need special treatment in order to impose the appropriate boundary conditions in the vicinity of the complex boundaries (see below). The governing equations are discretized and solved on all the other nodes of the background grid which are classified as fluid nodes (Fig. 4.7). To identify the solid nodes on an arbitrarily refined mesh, the immersed boundaries are discretized using unstructured triangular meshes and the ray-casting method is employed. The overall search algorithm is accelerated by adopting the concept of the bounding box, proposed by Borazjani *et al.* [82].

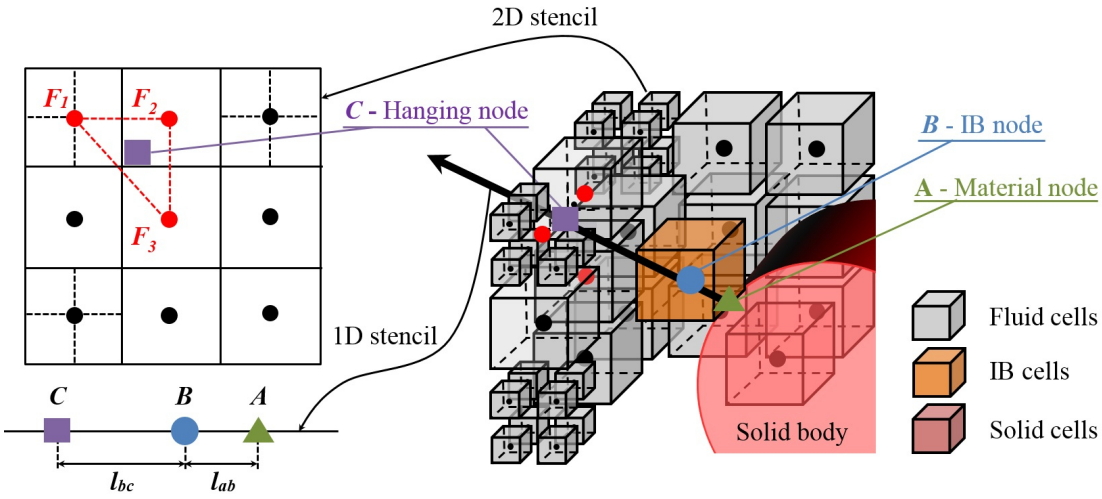

Figure 4.6: Classification of the cell centered nodes on unstructured Cartesian grids and utilization of 1D three-point stencils to facilitate the reconstruction of pressure and velocity field around immersed bodies. Bottom: Utilization of stencils to reconstruct the pressure and velocity field around the immersed bodies on unstructured Cartesian grids [4].

If we assume that the dynamically evolving solid surface $\Gamma^b(t)$ is represented by a

set of K material points that lie on $\Gamma^b(t)$, the corresponding Lagrangian position vector $\mathbf{r}^k(t)$ will be:

$$\mathbf{r}^k(t) \in \Gamma^b(t) \quad \forall \quad t > 0, \quad with \quad \mathbf{r}^k(0) = \mathbf{r}_0^k \quad \forall \quad k = 1, K \tag{4.60}$$

with $\mathbf{r}_0^k$ being the initial position of the k^{th} material point on $\Gamma_0^b \equiv \Gamma^b(0)$. In fact, the material points are the nodes of the triangular mesh of the immersed body. The prescribed motion of the immersed body correlate the velocity of the material points with the temporal variation of the location of those points; as a result of the movement of the interface $\Gamma^b(t)$:

$$\frac{\partial \mathbf{r}^k}{\partial t} = \mathbf{U}^k(t), \quad with \quad \mathbf{r}^k(0) = \mathbf{r}_0^k \quad \forall \quad k = 1, K \tag{4.61}$$

The Lagrangian specification of the velocity of the material points can be linked with the Eulerian velocity vector:

$$\mathbf{u}(\mathbf{r}^k(t), t) = \mathbf{U}^k(t) \quad \forall \quad k = 1, K \tag{4.62}$$

and this constitutes boundary condition to be imposed at every time step.

The pressure field around the immersed body can be calculated by enforcing the Neumann boundary condition on the $\Gamma^b(t)$ interface, by projecting the momentum equation along to the wall normal direction, Γ^b and neglecting the viscous forces and the subgrid-scale stresses:

$$-\frac{\partial p}{\partial n}\bigg|_{\mathbf{r}^k} = \mathbf{n}^k \frac{\partial \mathbf{U}^k(t)}{\partial t} \tag{4.63}$$

where $\mathbf{n}^k$ denotes a unit vector normal to the body at $\mathbf{r}^k$. Note that the pressure on the immersed boundary surface is required when the forces imparted by the flow on the body need to be calculated.

Concerning the discretization of the governing equations in the immediate vicinity of the immersed body, the approach described by [80, 82] on unstructured Cartesian grids is employed. Initially, the velocity field is reconstructed at all the IB nodes (node-B) from the material nodes (node-A) and the hanging nodes (node-C) (Fig. 4.7). Nodes-A correspond to each IB nodes (node-B) and are identified by projecting the IB nodes to the IB surface triangular mesh. Dirichlet condition is imposed at the nodes-A and the

components of the velocity field are calculated from the values of the material points (the vertices of the triangular elements) from Eq. (4.62), by using an inverse distance function [80]. The hanging nodes, node-C, are identified as the closest intersection of the surface-normal vector and any of the six planes around the IB cells, which are essentially 3×3 support stencils formed from the cell centered values of the surrounding hyper-cells, and are parallel to the IB cells' faces (Fig. 4.3). Then, having identified the 3×3 support stencil, the three closest, coplanar hyper-cell centers (F_1, F_2 and F_3) are used to calculate the velocity components at the nodes-C, by using the above mentioned inverse distance function, as shown in Fig. 4.7. Finally, the velocity components at the IB nodes are calculated from the nodes-A and C as described in [83]. The pressure field needs to be reconstructed at the IB nodes, p_b, only if the immersed body is moving, due to the hybrid staggered/non-staggered layout. In such a case, the pressure at the IB nodes can be obtained after discretizing Eq. (4.63) and enforcing Neumann condition:

$$p_b = p_c + \mathbf{n}\frac{\mathbf{U}^n - \mathbf{U}^{n-1}}{\Delta t} l_{bc} \tag{4.64}$$

where l_{cb} is the distance between the nodes-A and B (Fig. 4.7), the superscripts n and $n-1$ denote the current and previous time steps and p_c is the value for pressure at node-C which can be calculated following the above mentioned approach to reconstruct the velocity field. More details about the implementation of the immersed boundary method can be found in Angelidis *et al.* [4].

4.8 Performance on parallel cluster

On a parallel computing cluster, Message Parsing Interface (MPI) is used to communicate across different processors. Each communication call comes at expense of extra computational time. Reducing the number of MPI communications is a critical aspect of increasing the compute time efficiency of any parallel code. Because of the monolithic nature of unstructured grid implementation and multiple levels of cell refinement, information required for computations from the neighboring cells is more than the structured case in CURVIB. Absence of a structured cell geometry makes it difficult to optimize the grid partitioning. This results in more MPI communications and higher over all execution time. It is proposed that changes in data structures which minimize the number

of MPI (Message Parsing Interface for parallel computer) communications and hence decrease the execution time of the code are critical for performance improvements of unstructured solvers on parallel computers. This is done by using a data structures for defining the neighborhood information. Referring to Fig. 4.3, the data structure named *cellConnectivity* holds the information about the neighbors not only in terms of global indices but also the local index numbering in the local vector on each processor. The structure is described in Fig. 4.8.

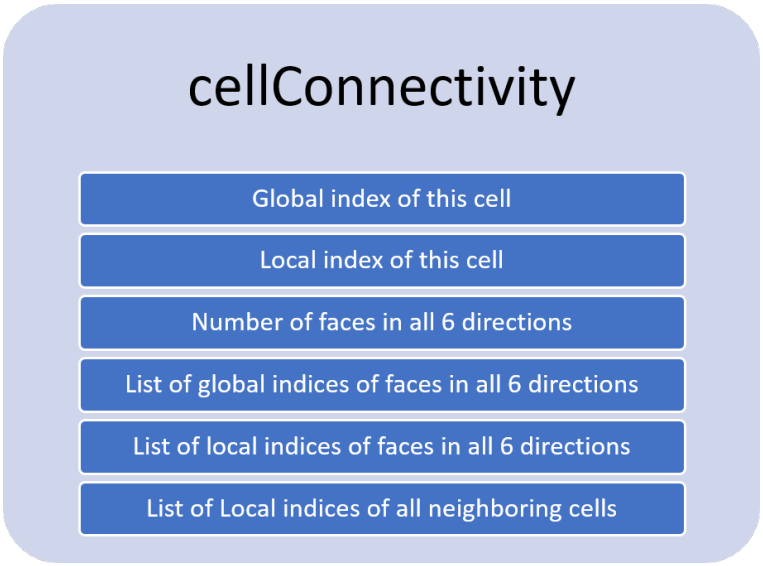

Figure 4.7: cellConnectivity data structure for each cell describing its position in the grid and details of neighboring cells and faces.

The values in the structures are populated at the beginning of the run only once and saved for every cell in an array of *cellConnectvity* data structures. The size of this array on each processor is total number of local cells plus the number of cells in ghost layer (belonging to other processors that are) required for computations. The calculation of local indices in the local vectors (along with ghosted cells) is obtained by an inverse mapping from global to local indices. The inverse mapping is not scalable over large number of processor because each local processor searches in the global vector [84].

Chapter 5

Validation of numerical method

In this chapter the numerical methods are validated against standard test cases and results from previously published works. Each of the different test cases are described in separate sections below.

5.1 Open channel flow

In this section the VFS flow solver is used to validate the code for a fully-developed flow in a long open channel. Incompressible fully-developed turbulent flow in a square duct is a popular canonical flow problem studied by many investigators. An interesting phenomena that is challenging to reproduce in numerical simulations is the presence of secondary flow structures specially at the mixed-boundary corner i.e. the corner where the corner where free surface and the sidewalls of the channel meet. Such secondary flows are also common around obstacles in a river flow [6]. The production and dissipation of turbulence are higher near the wall compared to the bulk of the flow. Near the free surface dissipation is non-zero but very small compared to the bulk. The production of turbulence is negligible near the free surface. This disparity near the no-slip wall and free surface corner and the anisotropy near the boundaries leads to anisotropy and results in the secondary flows are a result of anisotrpy. Therefore, turbulence models which do not account for the anisotropy cannot inherently reproduce the secondary flow.

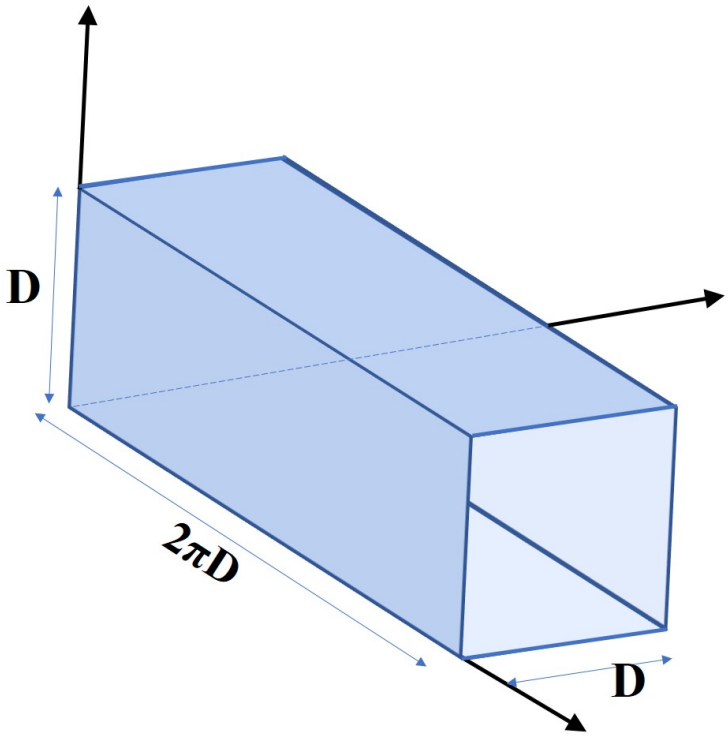

Figure 5.1: Domain for periodic open channel flow simulation in a square duct.

5.1.1 Computational Setup

One of the test case of Broglia *et. al.*'s [6] open-channel duct flow was chosen for simulation. They performed calculations at several Reynolds number, of which, the one with the highest Reynolds number is chosen. For this case the Reynolds number based on the side of the duct D and friction velocity u_τ is $Re_\tau = 1000$. $Re_b = 17130$ based on side of duct and bulk mean inflow velocity (U_b). The computational domain, as shown in Fig. 5.1, is a duct of cross section of $D \times D$ and streamwise length $2\pi D$. As shown by [], the streamwise length of $2\pi D$ is enough to contain the longest eddy in the flow for a duct of size D. The computational grid for this case is also shown in Fig. 5.2. The grid has 301, 197 and 197 points in the streamwise (z), vertical (y) and spanwise (x) directions, respectively, and approximately 1.2×10^7 grid points in total. In the z direction, the grid points was distributed uniformly whereas in the x

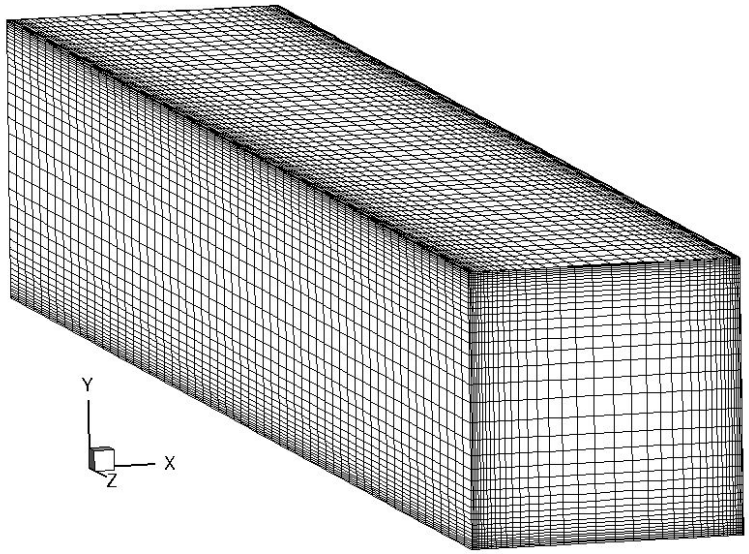

Figure 5.2: Computational grid used for periodic open channel flow simulation in a square duct. Every 5th grid lines are shown for the purpose of clarity.

and y directions, grid points were clustered close to the wall such that the first grid point off the wall was $x^+ = 5.5$ and $y^+ = 5.5$ wall units away from the wall boundary. In order to simulate the fully developed flow in a very long channel periodic boundary conditions are used in the streamwise direction of the domain. At the top free surface, symmetric boundary conditions were imposed. At the rest of the three boundaries, no-slip boundary condition was imposed.

The Navier Stokes equations were solved on the computational grid using the method described in Sec. 4.5. Equations were integrated in time until the total Kinetic energy of the computational domain is stabilized indicating that the fully developed flow conditions have been reached. The simulations were run for another ***25*** eddy turnover times (one eddy turnover time is the time for mean flow to travel across the computational domain). The simulations were further averaged over cross-sections in the streamwise direction to achieve better statistical averaging by increasing the sample size.

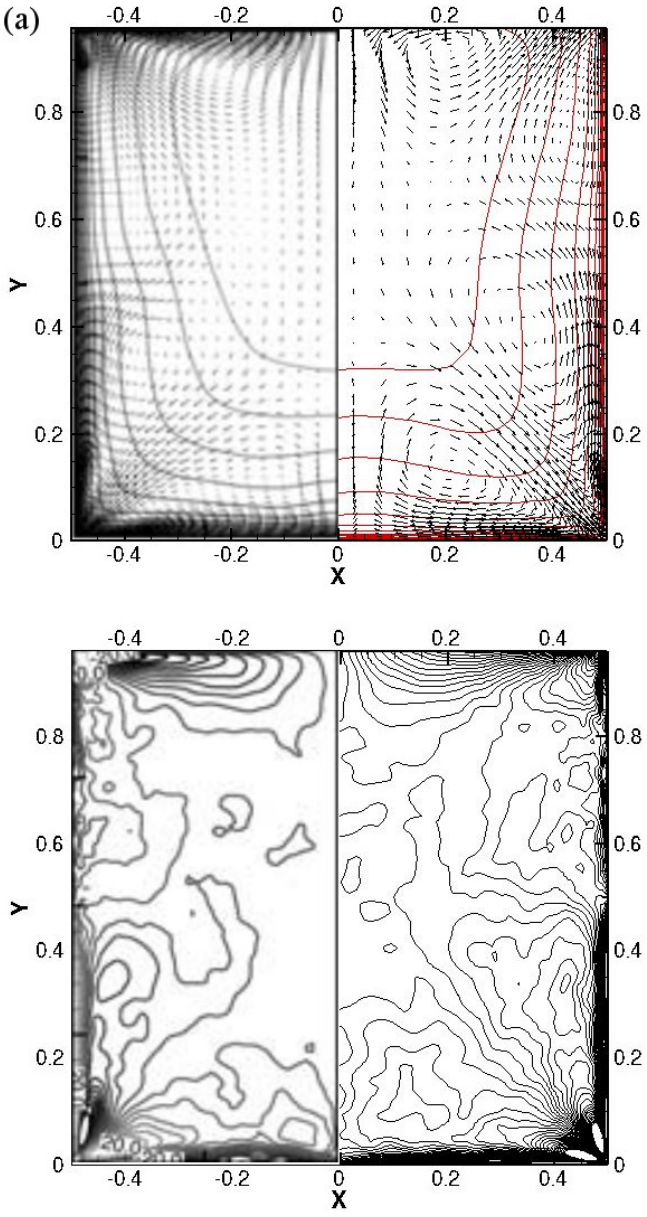

Figure 5.3: Open channel flow results: contours of (a) mean streamwise velocity and (b) mean streamwise vorticity in a plane perpendicular to the streamwise flow direction. Left half shows contours from [6] and right half are results from present LES calculations.

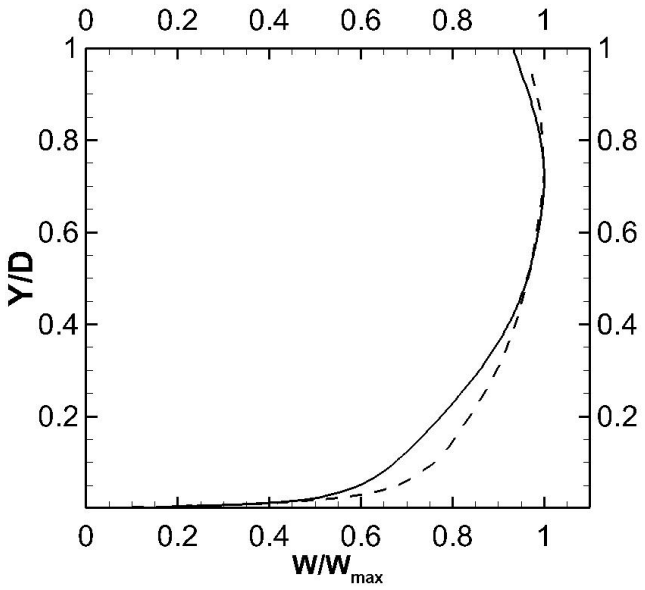

Figure 5.4: Open channel flow results: Comparison of streamwise velocity in the vertical direction at the central plane. Dots are from [6] and line is from results from present LES calculations.

5.1.2 Comparison

The contours of averaged results are shown in Fig. 5.3. The mean streamwise velocity contours are qualitatively similar behavior. It is difficult to compare exact contour levels because the number of contours levels were not specified in the results of [6]. The pattern of in-plane vectors also show similar pattern. The plots for streamwise vorticity also show similar levels of qualitative agreement showing the important characteristics of the flow. The extrema of the vorticity occurs near the fixed walls because of the no-slip wall which acts as a source of vorticity in the flow. Near the bottom corner of the domain, the counter rotating vortex pair can be seen. In the central region of the duct, local extrema of vorticity exists. The secondary flows near the corner of the ducts can also be seen. The wall-wall corner and the wall-free surface corner both show secondary flow circulation but are different from each other. The secondary flow in the wall-free surface corner is composed of an inner and an outer mean secondary flow region. The inner secondary flow is weaker and convects fluid from the free surface region towards

the corner, whereas, the outer secondary fluid convects momentum from the wall region towards the free surface.

For more quantitative comparison, the mean streamwise velocity profile is plotted in the mid-plane in vertical direction i.e.$X = 0$ plane (Fig. 5.4). The velocity profile agree with each other well, specially in the log layer. There is some discrepancy closer to the wall which could be attributed to the coarser grid used for present LES.

5.2 Flow past an isolated model turbine

This section presents the validation of the actuator line model and the unstructured Cartesian grid flow-field solver. The wind tunnel experiments of Chamorro and Pórte-Agel [7] with an isolated miniature turbine model of a wind turbine is chosen for simulation. Their experiment has also been previously simulated using numerical models by Wu and Pórte-Agel [85] and by Yang *et al.* [8] using actuator models. As shown in the Fig 5.5, the diameter of the model turbine was $D = 15\,cm$ and hub-height was $h = 5D/6$. The turbine was rotating during the experiments with a Tip Speed Ratio (TSR) $\lambda = 4.1$. Reynolds number based on the incoming velocity at the hub height and the turbine diameter was $Re = 4.2 \times 10^4$.

The computational domain for present simulation has dimensions of $5D$, $3D$ and $20D$ in the spanwise (x), vertical (y) and streamwise (z) directions, respectively. The miniature turbine for this simulation is modeled using actuator lines using NACA0012 profiles [86] as used previously by Yang *et al.* [8] in their simulation. The numerical method employed is the Cartesian unstructured grid solver described earlier in 4.6

The initial starting grid had 51, 31 and 136 grid points in x, y and z directions, respectively resulting in a grid with 2×10^5 cells. Grid points were distributed uniformly in all three directions. Simulation is first performed with this initial grid (*grid I*) without any refinement. Subsequently, the initial grid is refined up to two levels using local grid refinement procedure to produce *grid II*. The resolution of of grid I gives approximately 10 grid-points per turbine diameter. The refinement is carried out in a region defined by a cylinder. This cylinder extends in the streamwise direction from $2D$ upstream to $14D$ downstream of the turbine location. The axis of this cylinder coincides with the turbine.The final refined grid II consisted of total 1.7×10^6 cells giving

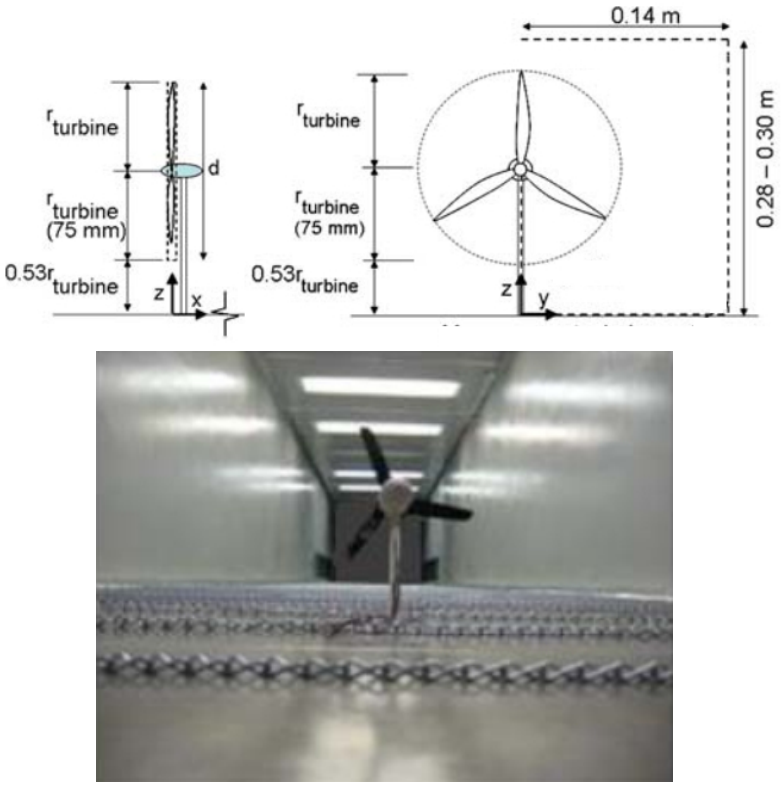

Figure 5.5: Wind tunnel experiments of Chamorro and Pórte-Agel [7] with a miniature model of a wind turbine. Schematic of the model wind turbine – side and front views (top figure); photograph of wind tunnel with the miniature turbine (bottom figure).

a resolution of 40 points per turbine diameter in spanwise and vertical, and 28 points per turbine diameter in streamwise direction. An equivalent Cartesian grid with uniform distribution of gridpoints corresponding to the resolution of the two level refined grid II would consist of 1.3×10^7 cells. The computational domain of Yang *et al.*'s simulation [8] studying the same problem was $30D$, $12D$ and $3D$ in the streamwise, spanwise and vertical directions, respectively. The grid used for this simulation was had non-uniform distribution of grid-points with 481, 241 and 121 grid-points in the streamwise, spanwise and vertical directions, respectively, having a resolution of 40 points per diameter.

Free-slip boundary conditions were imposed at the top boundary as well as the two side walls in the spanwise (y) directions. At the bottom wall, wall modeling approach of

[87] is implied to account for the insufficient wall-resolving grid resolution in near-wall region. At the streamwise exit boundary, Newmann outflow boundary condition is used whereas the inlet is fed with a pre-computed fully developed turbulent flow. A separate LES with periodic boundary condition was performed to obtain this fully-developed turbulent flow. Time step for the simulations was set to $\Delta t = 0.001D/W_h$ where W_h is the incoming velocity at the hub-height of the turbine.

In Fig. 5.6 (a), the vertical profiles of mean streawise velocity are plotted in a central plan bisecting the domain at 4 different downstream distances from the turbine location. Similar profiles from the experiment of Chamorro and Pórte-Agel [7] and simulation of Yang *et al.* [8] are also plotted for comparison. The present simulation shows good agreement with the previous simulation and the experimental measurements. The velocity deficit in near the hub region in the near-wake of the turbine is under-predicted by the actuator line model results. This discrepancy of actuator line model is well documented and observed in other previous actuator line calculations as well [11, 8]. This is caused because in actuator line model, the nacelle is not modeled. The velocity deficit caused by the presence of the nacelle obstructing the flow is not accounted in the model giving rise to lower velocity deficit in simulation. The streamwise turbulence intensity profile on central bisecting plane is compared in Fig. 5.6 (b) with the experiments and previous computations. The results from present calculation show good levels of agreement for turbulence intensity with the previous computations and experiment. The prediction becomes better as we move downstream in the turbine wake. As with the mean streamwise velocity, the turbulence intensities are also affected in the near wake due to absence of nacelle and tower in the computations. Similar trends are observed in the prediction of the Reynolds shear stress component in the streamwise-vertical component with overall acceptable prediction in the wake but more accurate in the far-wake.

Overall, the simulations showed good comparison with experiments except the near wake discrepancies due to missing nacelle geometry. Actuator line model provides an excellent way of modeling axial turbines in a computationally less expensive simulation. Combining the actuator model with the local mesh refinement gives us a powerful way to less expensive simulation of wake prediction capturing the essential dynamics in the wake.

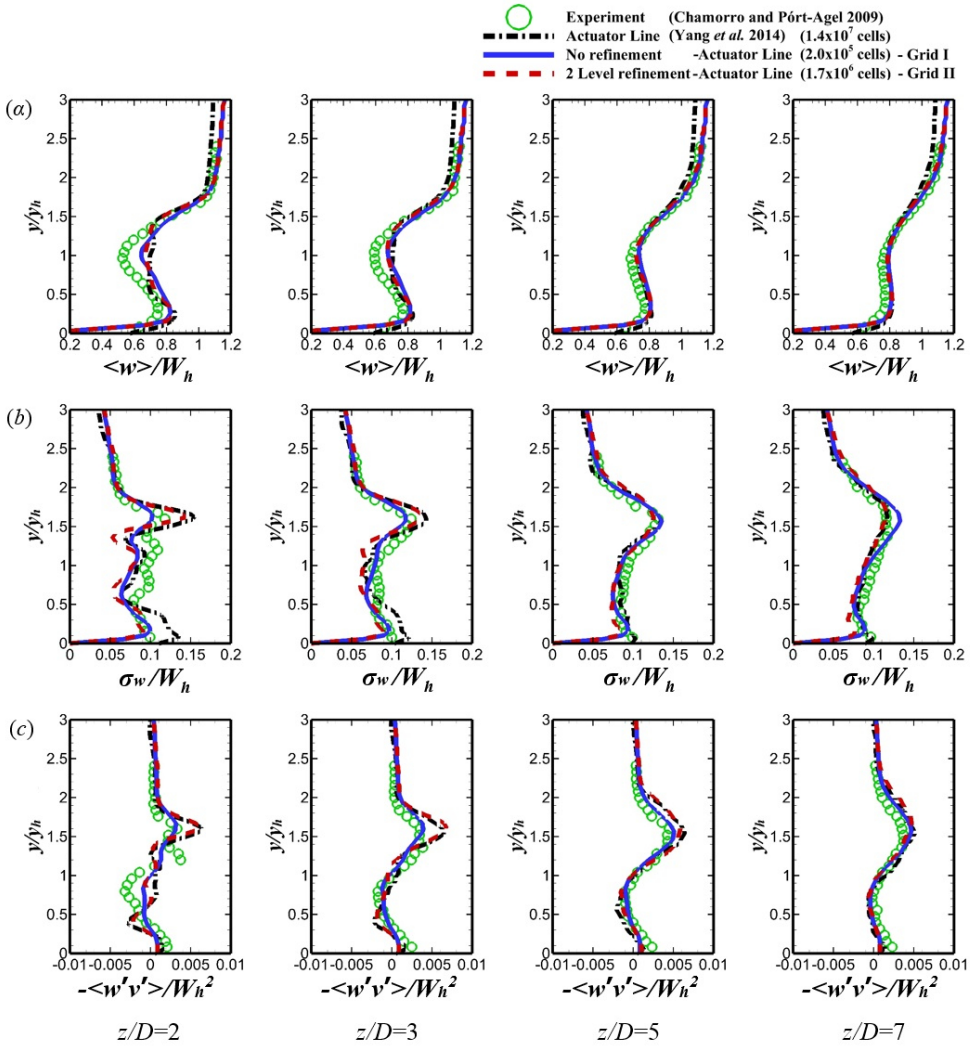

Figure 5.6: Comparison of the vertical profiles of mean flow quantities, at different locations downstream the wind turbine [7], calculated on a uniform Cartesian grid $51 \times 31 \times 136$ without refinement (grid I) and on a 2-level refined grid adapted around and in the wake of the wind turbine's rotor (grid II), against previous experimental measurements [7] and numerical simulations [8]. (a) Streamwise velocity, (b) streamwise turbulence intensity, and (c) Reynolds shear stress component. Here σ_w is the streamwise turbulence intensity, v and w are the instantaneous velocities in the y, and z directions, respectively, and W_h is incoming velocity at the hub height. The prime symbol denotes fluctuating quantities and <...> indicates the time averaging operation. (Figure adapted from [4]

5.3 Flow past an array of model wind turbine

In this section we model a miniature wind farm to illustrate the ability of flow solver to replicate flows with multiple axial turbines. The incompressible Navier-Stokes equations is solved on locally refined unstructured Cartesian grids using method described in section 4.6. Large-eddy simulation of multiple wind turbine wakes is carried out with the AL parameterization. The experiments of Chamorro and Porté-Agel [9] are chosen for the propose of this simulation. These experiments were also simulated using LES method earlier by Yang *et al.* [88].

Experiments were performed by Chamorro and Porté-Agel [9] at SAFL wind tunnel with 18 miniature wind turbines to form an aligned wind farm of 3 rows each with 6 aligned turbines in streamwise direction. The streamwise and spanwise spacing between the turbines are 5D and 4D, respectively. The miniature turbine used for this experiment are the same $D = 15\,cm$ diameter model turbine as in the previous section 5.2. The incoming wind velocity profile in the wind tunnel was such that velocity was $U_h = 2.1\,m/s$ at the hub-height. The boundary layer depth of the incoming profile was $0.5\,m$ and the free-stream velocity was $3\,m/s$. The turbines were rotating at tip speed ratio at $\lambda = 4.1$. The Reynolds number based on boundary layer depth and the free-stream velocity was $Re_\infty = 1.12 \times 10^5$ where as $Re_D = 23500$ based on the hub-height velocity and the turbine diameter. The computational domain to simulate the wind farm is $5D$, $12D$ and $33D$ in the spanwise (X), vertical (Y) and streamwise (Z) directions, respectively. The computational grid for this case had 120, 60 and 330 grid cells in the X, Y and Z directions, respectively. The grid was refined to 1 level in a cylindrical region such that its axis is aligned with the axis of the middle column of turbine and its diameter is $1.4D$. The refinement region extends from $1D$ upstream of first turbine to $5D$ downstream of the last turbine in the row (see Fig. 5.7.

In Fig. 5.8 the mean streamwise velocity in the wake is shown for the central row of turbines. The velocities are compared with experimental measurements along streamwise direction in the central plane at three different heights – (a) at the top-tip height, (b) at the hub-height and (c) at the bottom tip height. Excellent agreement is obtained for velocity profile at the top tip height of turbines. The profile at hub-height shows overall good agreement. For initial turbines, immediately downstream

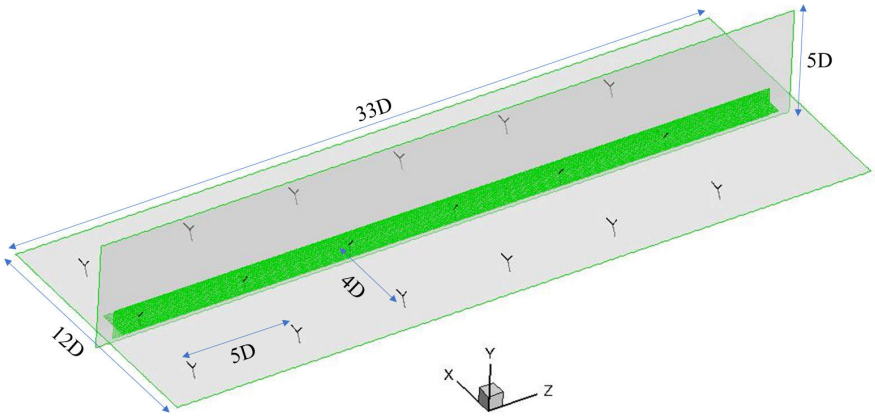

Figure 5.7: Computational domain and refinement for miniature wind farm simulation using actuator line model. The green mesh shows the region of 1 level refinement in the domain.

of the turbine, velocity is over-predicted. The lack of nacelle in actuator line model creates acceleration at the hub height leading to the over-prediction in the near wake. This under-prediction was also seen in the single turbine simulation previously. At the bottom tip location, velocity is over predicted for first 3 turbine wakes. For the last 3 turbines, excellent velocity prediction is obtained in the wake.

5.4 Flow past an isolated hydrokinetic turbine

(This section is adapted from and published in [4])

In this last simulated validation case the potential of the Cardesian unstructured grid refinement is illustrated. LES of a hydrokinetic turbine is carried out while resolving the turbine via the Immersed Boundary method (rather than parameterizing with the AL method). All geometrical details of the turbine, including the blades, nacelle and the tower are resolved. The experiment of Chamorro *et al.* [10] involve a very complex hydrokinetic turbine geometry and has also been studied numerically using the CURVIB method on structured Cartesian grids by Kang *et al.* [11].

The model turbine with diameter $D = 0.5\,m$ was placed in the main channel of the St. Anthony Falls Laboratory (SAFL) of the University of Minnesota. This channel is $2.75\,m$ wide and $85\,m$ long and the mean flow depth of the water (H) during the

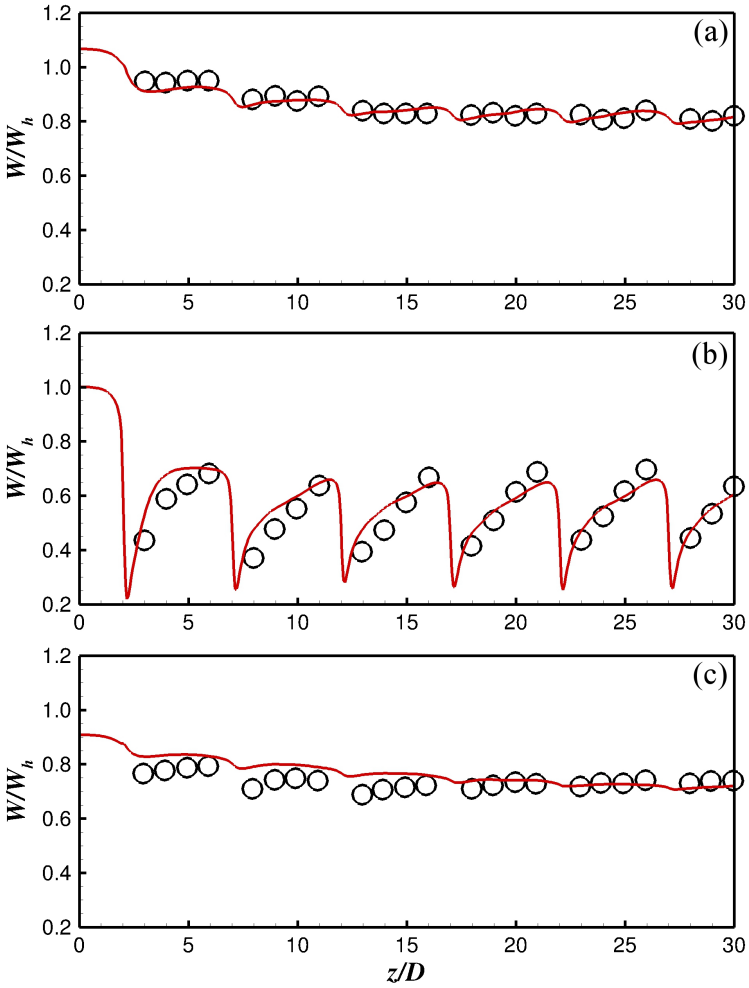

Figure 5.8: Comparison of mean streamwise velocity for miniature wind farm simulation at the central plane at (a) top-tip height, (b) hub height and (c) bottop-tip height. Lines represent results from present LES and circles are results from Chamorro and Porté-Agel [9]

experiments was $1.15\,m$. The turbine was located in the center of the channel so that the flow was fully-developed before it encounters the turbine. The bulk mean velocity in the channel was $U = 0.4\,m/s$. The Reynolds number based on bulk mean velocity and turbine diameter was $Re = 1.7 \times 10^5$. The turbine was rotating with an angular speed of $\omega = 9.43 rad/s$ about its axis, resulting in a TSR of $\lambda = 5.89$. More details of the experiments can be found in [10].

Similar to [11], a subsection of the main channel $9D$ long (z) , $5D$ wide (x) and $2.3D$ deep (y) is chosen as computational domain. Inside the computational domain, the rotating center of the turbine is placed at (0,0.8D,0) and the base of the pylon is at (0,0,-0.3D). The inlet is fed with a fully developed channel flow pre-computed from a separate LES of periodic channel flow. The channel of this LES had same cross section as the computational domain for turbine simulation. The two channel side walls and the bottom bed were assumed to be hydrodynamically smooth. Wall-modeling approach of Wang and Moin [89] was used to reconstruct velocity boundary conditions at all turbine surface and channel walls; the details of implementing the wall model in the context of the Immersed Boundary method can be found in [82]. At the free surface of the domain, zero-flux and free-slip boundary conditions are employed.

The primary uniform Cartesian grid for this case has N_x=126, N_y=58 and N_z=451 grid nodes (N_x, N_y and N_z are the number of grid nodes in x, y and z, respectively) resulting in a resolution of $25 \times 25 \times 50$ cells per rotor diameter, along x, y and z directions, respectively (level zero). This is locally refined near the turbine rotor by applying two levels of refinement around and in wake of the turbine, as shown in Fig. 5.9. The resulted refined grid had maximum resolution of $100 \times 100 \times 200$ cells per rotor diameter, along x, y and z directions, in the immediate vicinity of the turbine and a total of 8×10^7 cells. The simulations were first run for 25 revolutions until the total kinetic energy of the domain reached a quasi-steady state. Subsequently, the results were time averaged for another 55 rotor revolutions.

Figure 5.10 presents the instantaneous contours of the streamwise velocity on the x=0 and y/D=0.8 planes across the hub. It is evident that the energetic, slowly precessing low streamwise velocity region originates in the immediate vicinity of the nacelle, as was also identified by Kang *et al.* [11] who extensively studied its importance on the far wake development. The simulations also capture the onset of far wake meandering

that manifests itself as large-amplitude, low-frequency lateral fluctuations starting at approximately 3D downstream of the rotor. These findings are in excellent agreement with the findings of Kang *et al*. [11] regarding the rich coherent dynamics of the turbine wake and the importance of accurately resolving the details of the turbine nacelle for capturing such dynamics (Fig. 5.10).

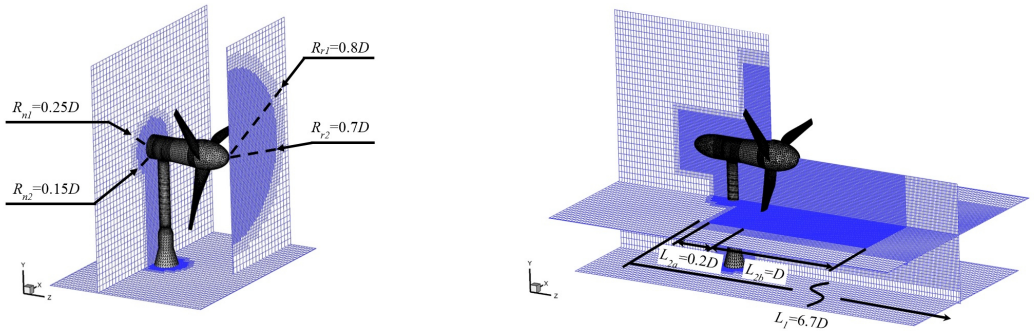

Figure 5.9: 2-level local mesh refinement adapted around and in the wake of a hydrokinetic turbine [10]. A primary uniform Cartesian grid $126 \times 58 \times 451$ is refined resulting in a maximum resolution of $100 \times 100 \times 200$ cells per rotor diameter in the vicinity of the turbine and 8×10^6 computational cells. The hydrokinetic turbine is discretized using a triangular mesh of 1.1×10^4 elements.

In Fig. 5.11a, the vertical profiles of the mean streamwise velocity are compared against experimental measurements [10] and simulations of the same case using the AL approach and previous geometry resolving LES [11]. The 2-level turbine resolving LES calculations agree well with the experimental measurements of [10]. Discrepancies between our results and the measurements may be attributed to the fact that the precomputed LES of fully developed channel flow fed at the inlet performed on the coarse primary grid to avoid any interpolation at the inlet of the domain. Also, further grid refinement is expected to improve velocity deficit prediction. Comparison with the AL calculations of [11] reveal that the over-prediction of the streamwise velocity in the near wake region of the turbine which is inherent in AL models [8, 11] is avoided by resolving the details of the hub and nacelle geometry. Our results also compare also well with the geometry resolving simulations of [11] who solved the same problem on a structured grid using the CURVIB solver [82]. Remarkably, with the locally refined unstructured Cartesian grid, the same level of agreement is achieved by using 20 times smaller number

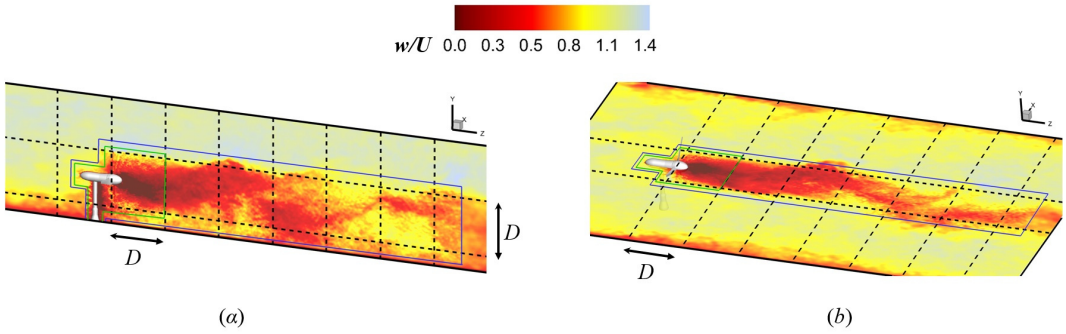

Figure 5.10: Contours of the instantaneous streamwise velocity w, normalized by the bulk velocity U, on planes across the hub: (a) x=0; (b) y=0.8D, for the geometry resolving LES around a hydrokinetic turbine [10] with tip speed ratio λ=5.89 at $Re = 1.7 \times 10^5$. Calculations are performed on a 2-level refined mesh and the inlet is fed with a fully developed channel flow pre-computed from a seperate LES. The blue and green solid lines indicate the regions where the 1^{st} and 2^{nd} levels of refinement applied, respectively.

of computational cells.

The computed vertical profiles of the turbulence kinetic energy (TKE) are shown in Fig. 5.11b. It can be observed that the pockets of high TKE that emanate from the nacelle and the tip vortices merge together and the TKE at upper tip height suddenly starts to increase when z>3D, in agreement with the study of [11]. The over prediction of the computed TKE levels in the near weak region around the hub height may indicate that higher grid resolution is needed. However, in the far wake (z>3D) our calculations are in very good agreement with the experimental measurements of [10], while the geometry resolving calculations of [11], who used very fine stretched Cartesian grid, under-predict the levels of turbulence kinetic energy. It is demonstrated that with our method the induced turbulence mixing can be accurately resolved on locally refined grids. Even though the AL simulations predict correctly the TKE levels on a coarse structured grid [11], the inherent weaknesses of the actuator line parameterization concerning the accuracy of near wake calculations and the non-grid independent solution of such methods have been discussed in [8, 11].

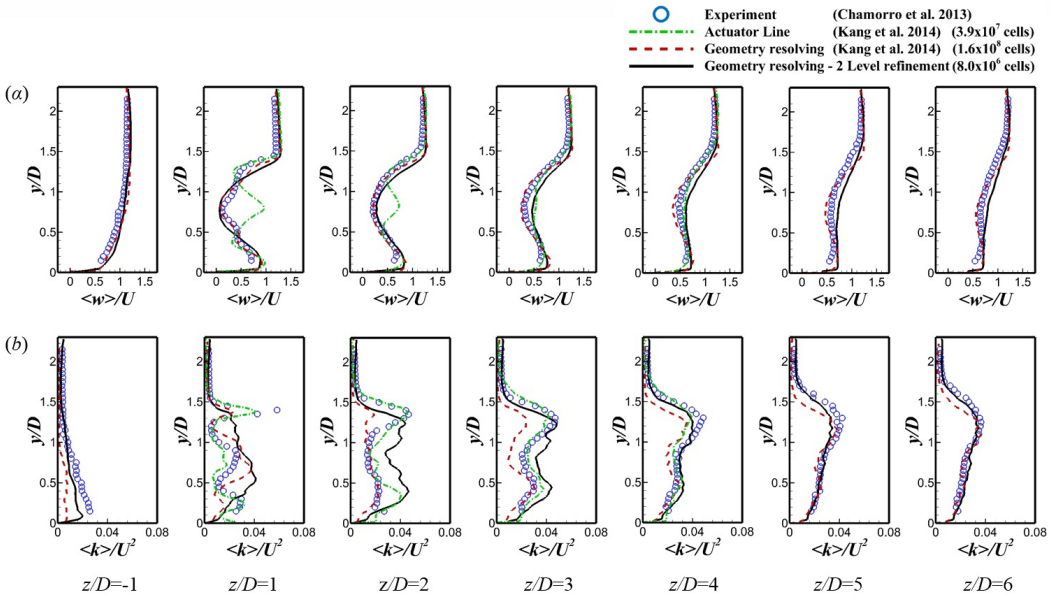

Figure 5.11: Comparison of the vertical profiles of mean flow quantities, at different locations downstream the hydrokinetic turbine [10], of geometry resolving LES computed on a 2-level refined grid, against previous calculations [11] and experimental measurements [10]. (a) Streamwise velocity, (b) turbulence kinetic energy. Here w and k are the instantaneous streamwise velocity and the turbulence kinetic energy, respectively, and <...> indicates the time averaging operation.

Chapter 6

Wake past TriFrame of turbines

Adapted from Journal Article:

Wake characteristics of a TriFrame of axial-flow hydrokinetic turbines, Saurabh Chawdhary, Craig Hill, Xiaolei Yang, Michele Guala, Dean Corren, Jonathan Colby, Fotis Sotiropoulos, *Renewable Energy*, 2016. (In review)

6.1 Introduction

In the many of the computational works discussed in the review, turbine parametrization was used to save computational cost involved in resolving the detailed geometry of a turbine. However, it was shown by Kang *et al.* [11] that the classic actuator disc and actuator line models without a model for the nacelle cannot accurately predict the velocity deficit in the near-wake, wake meandering and turbulence intensity in the far wake. The geometry-resolving model using immersed boundary method, on the other hand, captures the turbine wake dynamics for both near- and far-wake regions, and the computed results agree well with the measurements

An effective way to develop arrays of hydrokinetic turbines in river and tidal channels is to arrange them in conjunction, which is convenient for installation and maintenance of the turbines underwater. However, to the best of our knowledge, there are no studies on the wakes of turbines in conjunction available in literature that use a fully resolved

geometry of turbines. In this chapter, we employ the numerical method, i.e. LES module of the VFS code (see Section 4.5), resolving every geometrical details of the turbine, as in Kang *et al.* [11], together with experiments done by colleagues at SAFL, to study a TriFrame[1] of turbines, or simply TriFrame, which is defined as a layout where three turbines are mounted together at the apexes of a triangular frame (Fig. 6.1 (a)). The resulting arrangement is equivalent to two rows in a staggered fashion. TriFrames are an effective way to develop arrays of hydrokinetic turbines in river and tidal channels because of convenient installation and maintenance of the turbines underwater. The objective of this work is to study the wake characteristics of the three turbines in a TriFrame configuration and evaluate the feasibility of using such system as a building unit for turbine arrays.

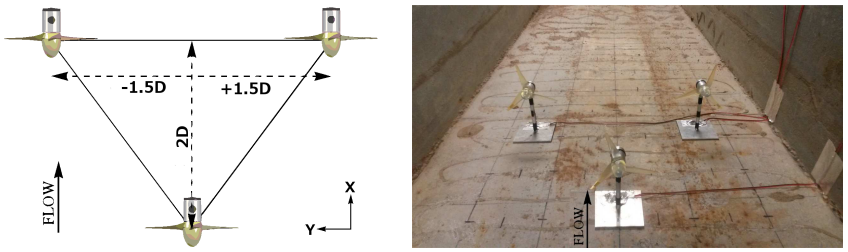

(a) (b)

Figure 6.1: (a) Sketch of TriFrame geometry used in the experiments and computations (D = turbine diameter = $0.15m$); (b) TriFrame of small scale model turbines placed in the laboratory flume at Saint Anthony Falls Laboratory (SAFL).

This paper is organized in the following fashion. In Section 6.2, the experimental and computational setup is described. Section 6.3 gives the details about domain splitting method used in the simulations. This is followed in Section 6.4 by discussion of the results obtained.

6.2 Test Case: TriFrame in Laboratory Flume

6.2.1 Experimental Setup

To study the wake of a TriFrame of axial-flow turbines, three model turbines were placed in a laboratory flume at Saint Anthony Falls Laboratory (SAFL). The channel

[1] *TriFrame* is a trademark of Verdant Power Inc.

was $0.9\,m$ wide, $8\,m$ long, and utilized a three axis automated traversing carriage to position different instruments to monitor water surface elevation and 3D instantaneous velocity. The miniature three-bladed axial-flow hydrokinetic turbines (Fig. 6.1 (b)) with rotor diameter, $D = 0.15\,m$, were installed in the channel. Additional details of the turbines used, including geometry, data acquisition techniques, and methods for determining tip-speed ratio can be found in Hill *et al.*[90, 91, 92]. Average flow depth was $H = 0.28\,m$ and average volumetric flow rate $Q_w = 0.068\,m^3/s$ resulting in a bulk approaching velocity of approximately $U_b = 0.27\,m/s$ and a mean hub height velocity of $U_{hub} = 0.32\,m/s$. Reynolds number based on the bulk mean inflow velocity U_b and turbine diameter D is $Re = 4.1 \times 10^4$. Using the same parameters, Froude number for the prescribed hydraulic condition was $Fr = 0.16$. The hub height of all three turbines was at $H_{hub} = 0.135\,m$ above the channel bottom. The upstream turbine (T1) in the first row was placed approximately $7\,m$ downstream of the channel inlet and was rotating with an averaged angular speed of $\bar{\omega} = 19.1\,rad/s$ while the two downstream turbines (T2, T3) in the second row were tangential slightly faster with $\bar{\omega} = 19.5\,rad/s$. Because the turbines did not have precise and constant angular velocity control, their angular velocity varied slightly in time due to unsteadiness in the approach flow; however, the mean tip speed ratio was $\lambda \approx 4.5$ for the first row turbine (T1) and $\lambda \approx 4.6$ for the second row of turbines (T2, T3). Here, tip speed ratio is defined as the ratio of the rotating speed at the blade outer tip and the incoming hub height velocity (U_{hub}) in the experiment (i.e. $\lambda = \bar{\omega}r/U_{hub}$, where r is the radius of the turbine rotor.). The blockage induced by the upstream turbine ($\approx 7\%$) created a slight acceleration on the lateral sides, thus resulting in an increased angular velocity for the downstream turbines. All three turbines rotated counter-clockwise looking downstream. An acoustic Doppler velocimeter (ADV) sampling at $100\,Hz$ was used to measure the three velocity components at several points at hub height, H_{hub}, in a plane parallel to the channel bottom. A second experiment using a single turbine but with the same hydraulic condition was also completed. These data are compared to the wakes of a TriFrame turbine configuration.

6.2.2 Computational Setup

Simulations were performed for both a TriFrame of turbines and a single isolated turbine for comparison. In order to save computational time, near-wake and far-wake simulations were carried out separately. The near-wake domain contains the turbines while the far-wake domain starts at the outflow of the near-wake domain as seen in Fig. 6.2. The streamwise length of the near-wake and far-wake domains is 9D and 12D, respectively. The velocity time-series from near-wake simulation is sampled at $x = 8D$ from the near-wake simulation and fed to the far-wake simulation. This amounts to a one-way coupling between the two computational domains. This one-way coupling is acceptable because convection of wakes to further downstream locations dominates the flows around 7D downstream from the TriFrame. Further validation is provided in Section 6.3 by comparing flow-field in the overlapping region. The TriFrame of turbines is placed in the center of the flume such that the rotating center of the upstream T1 turbine (or the only turbine for single turbine case) is located at (2D, 0, 0.9D), 2D downstream from the inlet plane. The second row turbines (T2, T3) are located as per Fig. 6.1(a). For the near-wake simulation, fully developed turbulent flow condition is prescribed at the inlet boundary. To achieve this, a separate precursor channel flow simulation is run with periodic boundary conditions in the streamwise direction to obtain a fully developed turbulent inflow. The cross section of this channel is the same as the flume. Time-series of the velocity on a cross section from this simulation are saved and introduced as the inlet velocity boundary condition for the near-wake simulations. The inflow for the far-wake simulation, on the other hand, is provided by the outflow of the near-wake simulation using time series of velocity vector extracted at each point on the plane $X = 8D$ (marked as section AA' in Fig. 6.2) saved in the near-wake simulation. The bottom and side walls of the flume had a small roughness height corresponding to the transition roughness regime. Since no roughness model is available to model this regime, the walls were assumed to be smooth. This assumption is not expected to significantly affect the velocity field near the turbines far away from the wall region. The top free surface of the channel, in both near- and far-wakes simulations, was modeled as rigid lid. Since the free surface level in the experiments did not change more than 3.5% of the flow depth, the rigid lid assumption will be an acceptable modeling approach.

At the exit of both near- and far-wake domains, Neumann boundary conditions are imposed. On the bottom bed and side walls, the first off-wall grid node was approximately 32 and 58 wall units away from the wall, respectively, in all cases. Since these points lie outside of the laminar region of the boundary layer, a wall-modeling approach was used (as described earlier in Section 4.3.1).

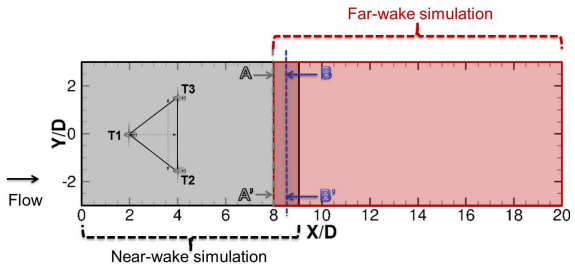

Figure 6.2: Simulation was performed in two parts - near-wake and far-wake. Section AA' is position where velocity was extracted in near-wake and fed to far-wake simulation. Comparison of velocity is made at section BB' for validation (see Fig. 6.4).

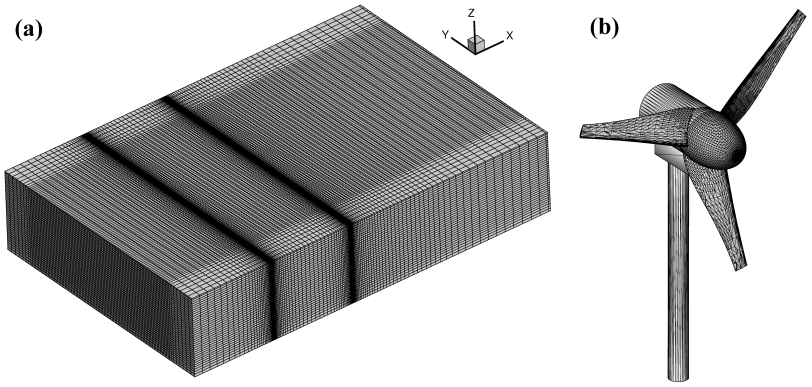

Figure 6.3: (a) Background grid for newar-wake simulation with TriFrame. Every fifth grid line is shown in all three direction. (b) Turbine geometry represented by unstructured triangular meshes.

The size of computational domain for each simulation is presented in Table 6.1. The table also lists number of grid points N_x, N_y and N_z in the X, Y and Z directions, respectively. The grid was stretched such that points were clustered in the region of the turbines as well as immediately downstream of the turbines. Fig. 6.3 shows background grid for near-field simulation with TriFrame. Same figure also shows turbine

represented by unstructured triangular mesh. In the near- and far-wake domains, the grid is stretched in the spanwise (Y) and vertical (Z) directions so that more points are clustered in the region near the turbines. The Y spacing ranges between D/100 and D/40 whereas Z spacing range between D/100 and D/75 where minimum spacings occur close to turbine and maximum spacings occur away from the turbine. These values do not change in the streamwise direction for both near-wake and far-wake simulations. For streamwise (X) grid spacing in the near-wake simulation, the grid is stretched such that near the turbine, the X-spacing is D/400 so that the blade thickness is resolved by the background grid cells. Very far away downstream from the turbine location, this spacing grows to D/25. In the far-wake simulation, the X-spacing has uniform value of D/50. For grid sensitivity studies, we rely on the earlier published works ([11, 93]) using the same code. They showed that, using immersed boundary method, the spatial resolution employed in the present work can give a reasonable agreement with the measurements of torque generation [93] and wake of the turbine [11]. The size of the time step was $\Delta t = 7.3 \times 10^{-4} D/U_b$ for all simulations. Simulations were run until the total kinetic energy of the whole computational domain converged to an asymptotic value which took approximately $1.5 - 2$ flow-through times or $15 - 20$ rotor revolutions of the first (T1) turbine in TriFrame (or single turbine). Subsequently, the results were time averaged for another 180 rotor revolutions for the TriFrame near-wake simulation and 75 revolutions for the single turbine near-wake simulation. For the far-wake simulations, averaging period was 180 rotor revolutions of T1 turbine in the TriFrame case and 63 rotor revolutions for single turbine case.

6.3 Domain splitting method

Both near- and far-wake characteristics of a TriFrame of turbines are important for developing TriFrame based turbine arrays. However, it is very expensive to simulate both the near- and far-wake locations in a single simulation using a sharp interface immersed (IB) boundary method because of the additional computational cost from identifying fluid, IB and solid nodes at every time step in the IB method, and reconstructing the left-hand-side matrix in the Poisson solver. In order to reduce this computational cost,

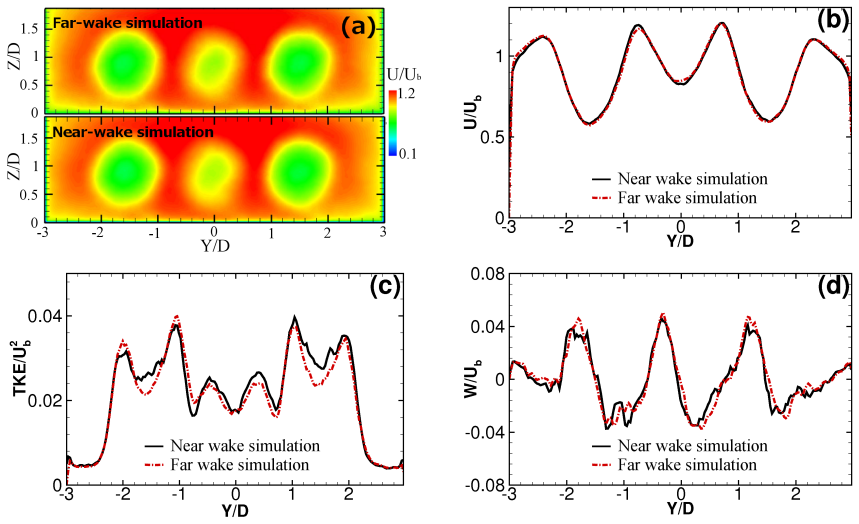

Figure 6.4: Comparison of flow field in section BB' of Fig. 6.2. (a) Normalized mean streamwise velocity U/U_b; (b) Spanwise profile of streamwise velocity at hub height; (c) Spanwise profile of TKE at hub height; (d) Spanwise profile of mean vertical velocity at hub height.

in this work we employ a domain splitting technique to simulate the near-wake and far-wake separately. In this technique, the velocities on a plane normal to the streamwise direction near the outlet of the near-wake simulation are saved at every time step. The saved velocity fields are then fed into the far-wake simulation as inflow conditions. The computational setup for the current simulations using this domain splitting technique will be presented in Section 6.2.2. Validation of this technique will be shown in Section 6.3.

The section between $8D$ and $9D$ is common between both simulations allowing for validation of the two-domain approach. Time averaged flow-field from both near- and far-wake simulations is extracted at section BB' at $8.5D$ (shown with blue dashed line in Fig. 6.2) and compared in Fig. 6.4. The contours of mean streamwise velocity from the two simulations match with each other well such that they differ by only 2% on average and 10% at most. Plots of mean velocity components and turbulence kinetic energy (TKE) in spanwise direction at the hub height approach each other, confirming the validity of the two domain technique.

6.4 Results and Discussion

In the following section we discuss the results of the experiments performed at SAFL with a TriFrame of turbines and the subsequent LES. Both mean flow and turbulence statistics are presented below.

6.4.1 Time-averaged flow field

In Fig. 6.5, time-averaged streamwise velocity profiles are plotted from both the experimental measurements and LES prediction along the span of the domain in the hub height plane at different downstream locations. Velocity deficit is created downstream of all three turbines. Simulation predictions show good agreement in the region downstream of the turbines. The peak in velocity deficit is captured accurately for both rows of turbines. Further downstream, the velocity is under-predicted by the LES. Velocity at the center line of the turbine wakes is within 7% of experimental value. Closer to the wall, towards the outer boundary of the wakes, the discrepancy is close to 10% which can be attributed to the discrepancy in the inlet profiles near walls.

The turbulence kinetic energy (TKE) in Fig. 6.6 shows a similar trend. Most of the TKE in the flow is generated due to the presence of the turbines. Similar to what is obtained in the measurement as well as observed by Kang *et al.*[11], the LES prediction shows multiple peaks in TKE created by each turbine. The peaks in TKE are well predicted in the near wake but under-predicted (by up to 25%) in the far wake downstream region.

The vertical velocity component (due to the wake rotation) profiles in the same plane are plotted in Fig. 6.7. The incoming flow has little to no vertical velocity component at hub height. The flow past the first turbine near the blades has a significant vertical velocity component which is accurately predicted by LES. Further downstream, the vertical component weakens and the LES prediction is not as accurate as in the near wake. Unlike LES, the incoming flow in the experiment has slight non-zero vertical velocity at hub height. This difference is propagated and seen downstream (until $\approx 1D$). This difference aside, vertical velocity from LES compares well with the experiments.

Next, contours predicted by the simulations are plotted in a streamwise-vertical plane normal to the channel bed and passing through the center of the turbines. In Fig.

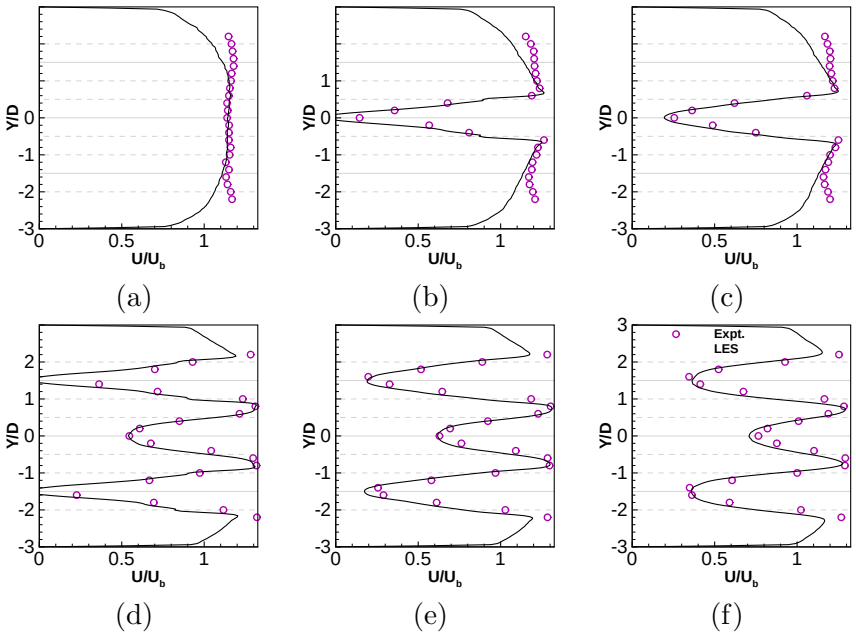

Figure 6.5: Comparison of streamwise velocity past the TriFrame of turbines at distances (a) 1 D upstream and (b) 0.5 D, (c) 1 D, (d) 2.5 D, (e) 3 D, (f) 4 D downstream of the first turbine (T1) in a horizontal plane at the turbine hub height.

6.8 the contours of time averaged streamwise velocity are shown for the three turbines of the TriFrame. Turbine numbers correspond to those indicated in Fig. 6.2. The contour plots show the shape of the wake and its recovery. There is a strong deceleration of the flow downstream of the turbine rotor and the hub. The wake is different for the first row and second row turbines with the latter showing lower recovery rate. The white lines on the plot mark zero streamwise velocity contour indicating presence of reverse flow in the vicinity of the hub. The transverse velocity contours in Fig. 6.9 show the compound wakes with an inner wake associated with the hub and an outer wake associated with the rotor. At approximately 2 D to 3 D downstream of turbine the two wake structures merge into one. The TKE (Fig. 6.10) shows contours similar to what was seen in Kang *et al.* [11]. Two regions of TKE generation exist - the tip of the rotor blades and the hub. These regions of TKE extend downstream, interacting close to the outer rotor shear layer. It is interesting to note that the wake of the upstream turbine shows significantly lower levels of TKE than the downstream ones.

To further analyze the differences between the wakes of different turbines in the

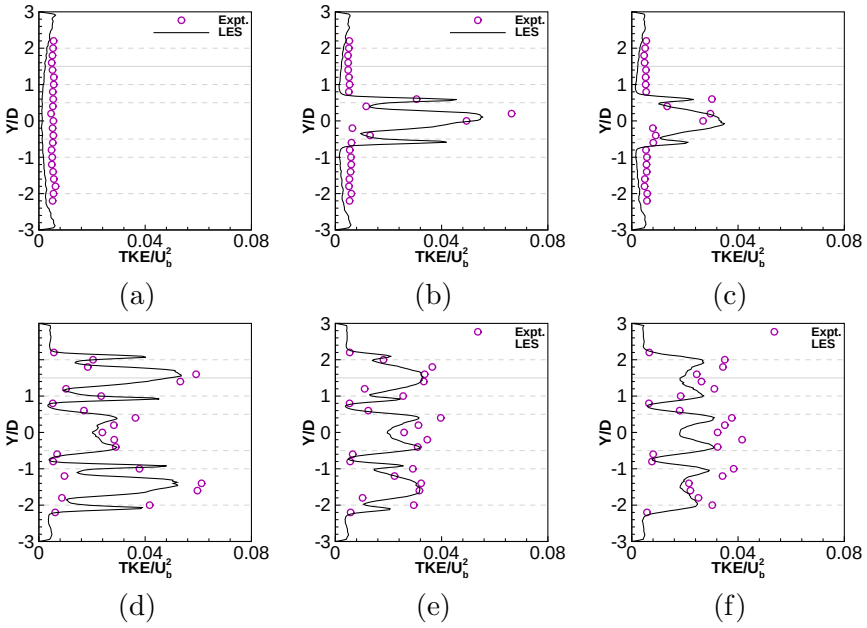

Figure 6.6: Comparison of turbulence kinetic energy (TKE) past the TriFrame of turbines at distances (a) $1\,D$ upstream and (b) $0.5\,D$, (c) $1\,D$, (d) $2.5\,D$, (e) $3\,D$, (f) $4\,D$ downstream of the first turbine (T1) in a horizontal plane at the turbine hub height.

TriFrame, contours of streamwise velocity and TKE are plotted on the wall parallel plane at hub height in Fig. 6.11. It is evident from this figure that the spanwise extent of the wake of the first turbine (T1) narrows starting at $2D$ downstream from the turbine and recovers at a much higher rate than the wakes of the other two turbines. In this region of wake constriction, the streamwise velocity is higher and the TKE levels are lower than the two downstream turbine wakes. These findings, attributed to the Venturi effect induced by turbines T2 and T3, have also been reported in experiments of Chamorro *et al.* [94] on a laboratory scale staggered wind farm. Simulations of Ammara *et al.* [95] also observed flow acceleration between two turbines in staggered configuration in their simulations.

The spanwise variation of streamwise velocity and TKE for the far-wake simulations are shown in Fig. 6.12. In the previously discussed Fig. 6.5, large momentum deficits were observed in the near wake, specially within $0.5D$ of the turbines where the streamwise velocity is negative. In the far wake, after $10\,D$ downstream, most of the momentum has recovered and the velocity profile of the superwake of the TriFrame of

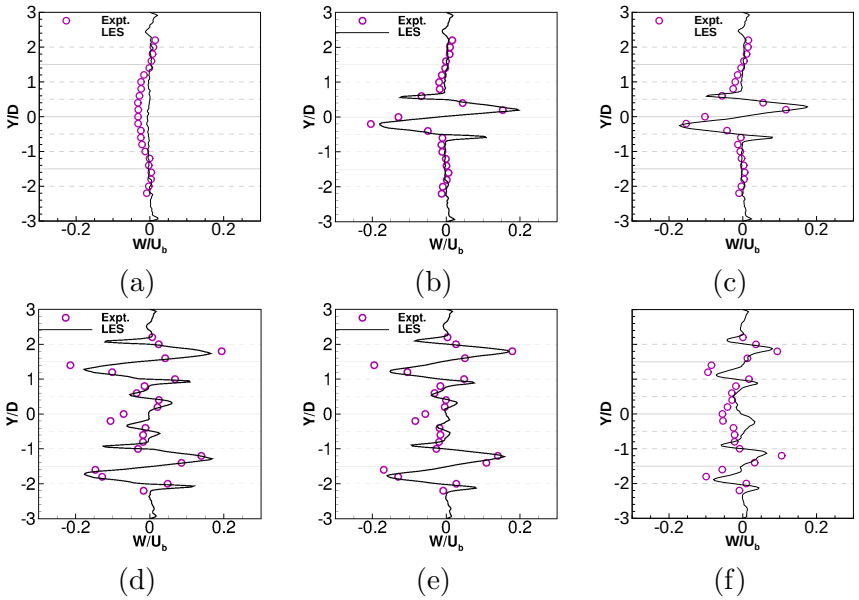

Figure 6.7: Comparison of vertical velocity past the TriFrame of turbines at distances (a) $1\,D$ upstream and (b) $0.5\,D$, (c) $1\,D$, (d) $2.5\,D$, (e) $3\,D$, (f) $4\,D$ downstream of the first turbine (T1) in a horizontal plane at the turbine hub height.

turbines changes very little. Fig 6.12(b) shows that the TKE generated by turbines in the near wake (see Fig. 6.6) decays in the wake slowly. Beyond $10\,D$, the TKE profiles of the superwake change very slowly.

6.4.2 Comparison with single turbine wake

To compare the wake of a TriFrame of turbines with that of a single turbine, a separate experiment and a separate LES were performed with an isolated single turbine in the same flume under the same conditions. The velocities from this experiment were also measured at hub height at different downstream locations in the near wake.

Fig. 6.13 and 6.14 illustrate the streamwise velocity and TKE, respectively, at certain distances downstream from the position of each of the three turbines in TriFrame and the isolated single turbine. For T2 and T3 TriFrame turbines in plots of Fig. 6.13 and 6.14, positive Y represents the locations near the channel center and negative Y represents locations near the channel wall. This is not applicable to the other two turbines since they have symmetric wall conditions on both sides in the spanwise direction.

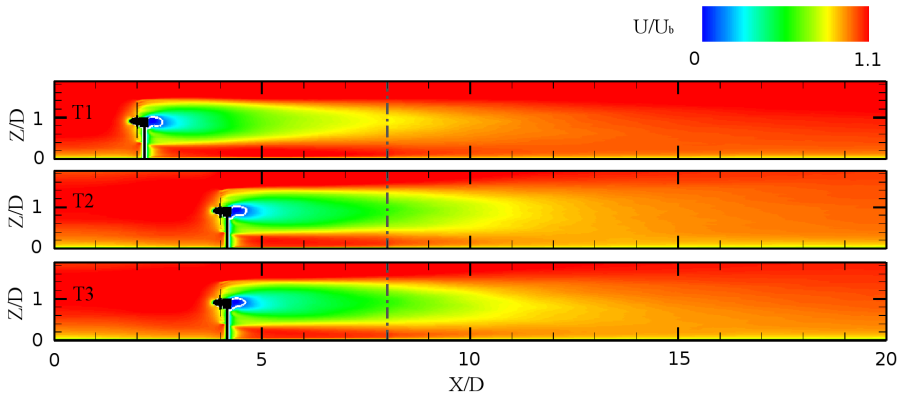

Figure 6.8: Contours of time averaged streamwise velocity, U, normalized by bulk mean inflow velocity, U_b, in the vertical plane passing through the center of the rotor for the turbines T1, T2 and T3. White line marks the contour of $U/U_b = 0$. Dash-dot line shows the start of far-wake simulation.

As can be seen from Fig. 6.13, the streamwise velocity profile for all turbines look very similar at $1\,D$ where the wake from the upstream turbine in the TriFrame is not yet influenced by the two downstream turbines. Further downstream ($2\,D$ to $3\,D$), the wake of the upstream turbine T1 of the TriFrame recovers much faster than the isolated turbine and the two downstream TriFrame turbines because of the Venturi effect. Beyond $3\,D$ downstream, the wake recovery of the first turbine (T1) occurs at nearly the same rate as the other turbines. On the other hand, the spanwise profiles of velocity of the two downstream turbines of the TriFrame and the isolated single turbine still look very similar to each other. The difference between the T1 turbine wake and the other turbines diminishes as we move downstream. At $12\,D$ and beyond, this difference is very small and the mean wake for all turbines has mostly recovered. At $15\,D$, the T1 turbine wake has completely recovered. For the two downstream TriFrame turbines, the streamwise velocity is nearly symmetric within the wake, yet the streamwise velocity out of the wake is larger near the channel center than near the channel walls. The T2 and T3 turbines recover at a rate similar to that of the isolated turbine for the region within the wake i.e. within spanwise distance of approximately $0.5\,D$ centered at turbine rotor. In regions far from the center the recovery is faster for T2 and T3 turbines.

Lower TKE levels in the wake will result in less fatigue loading on the downstream turbines in the array. Therefore, it is important to discuss the spatial evolution of TKE

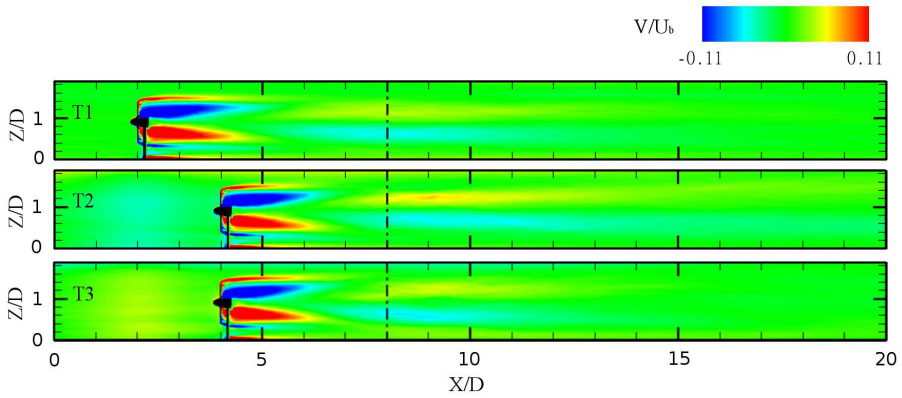

Figure 6.9: Contours of time averaged transverse velocity, V, normalized by bulk mean inflow velocity, U_b, in the vertical plane passing through the center of the rotor for the turbines T1, T2 and T3. Dash-dot line shows the start of far-wake simulation.

in the wake. Fig. 6.14 highlights the spanwise profiles of TKE at different downstream locations, illustrating the effect of turbine-turbine interactions on TKE levels. After 2D, the TKE of the T1 turbine wake is significantly lower than both T2 and T3 turbines (between 17-23% lower) and the isolated turbine (23% lower) in regions near the rotor tip (marked with dashed grey lines in the plots). In the inner wake region, the TKE levels for each of the turbines are comparable to each other for much of the wake except between $4\,D$ and $8\,D$ when T1 turbine inner wake also shows lower TKE (by 16-40%) than the other turbines. The difference in TKE levels continues to diminish and profiles of all wakes look similar at $12\,D$ and beyond where values are within 4% of each other. In Fig. 6.15 we plot the time-averaged TKE contours on Y-Z planes (wall-normal, perpendicular to flow) located at 2D, 3D and 4D downstream of the respective turbines First, the TKE from the first turbine in the TriFrame is lower than the other three turbines at all three downstream locations. At 2D and 3D, the intensity of the maximum TKE from the two downstream turbines in the TriFrame are very similar to that of the single turbine. At 4D, on the other hand, the TKE in the wake of the two downstream turbines in the TriFrame are higher and distributed in a wider region, which is significantly different from that of the single turbine.

To understand the Venturi effects in the superwake, we define a special wake function

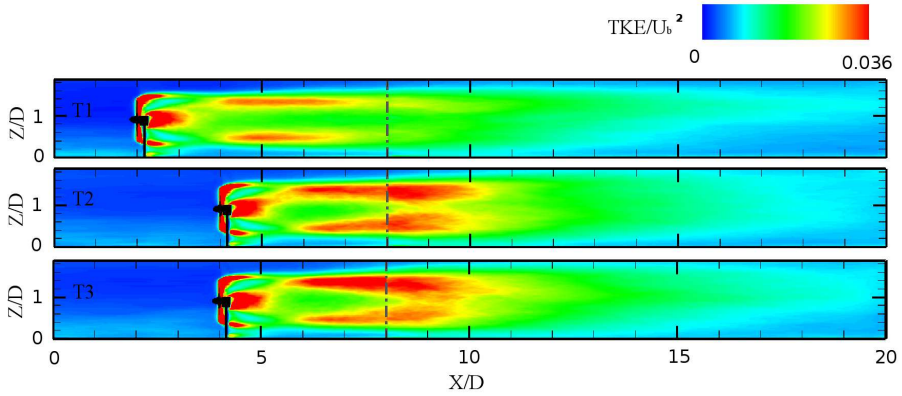

Figure 6.10: Contours of TKE normalized by the square of bulk mean inflow velocity in the vertical plane passing through the center of the rotor for the turbines T1, T2 and T3. Dash-dot line shows the start of far-wake simulation.

Φ using the following relationship:

$$\Phi(x,y) = \frac{U(x,y,z_c) - U(x,y_c,z_c)}{U_{hub,in}} \tag{6.1}$$

where $U(x,y,z)$ is the time-averaged streamwise velocity any point in space, (x_c, y_c, z_c) is the location of the center of turbine rotor and $U_{hub,in}$ is the incoming hub height velocity intercepted by the turbine. In Fig. 6.16 we plot Φ at different distances downstream from the turbine rotor for the single turbine and T1 turbine of TriFrame. Plots of $\Phi(x,y)$ for T2 and T3 turbines are not shown for succinctness. The maxima near the rotor tip region defines the spanwise extent of the mean wake of the turbine. The locus of these maxima in Φ is also shown in the plot. This locus represents the shape of the mean wake. In Fig. 6.16 (c), the locus of maxima for the single turbine and the TriFrame turbines are collectively shown in the XY plane at hub height. It shows that the wake of all turbine in the TriFrame follow that of the single turbine until $2\,D$ downstream distance. After this distance, the turbines T2 and T3 are encountered and the Venturi effect causes the T1 wake to constrict. This is shown by the kink in the locus of T1 turbine. The locus for T2 and T3 turbines also depart from the single turbine case, although the T2 wake is most similar. The wakes of T2 and T3 turbines also differ from each other in spite of the apparent symmetry of the setup. This asymmetry originates from the fact that all three turbines rotate in the same (-X) direction introducing an

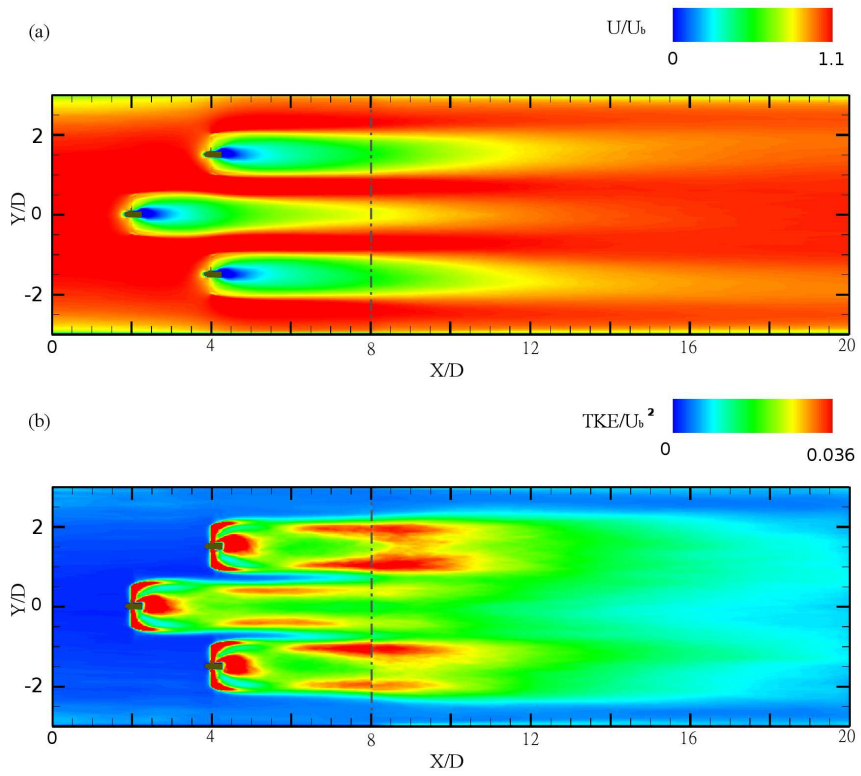

Figure 6.11: Contours of time averaged normalized (a) streamwise velocity and (b) TKE in hub height plane for the three turbines. Dash-dot line shows the start of far-wake simulation.

inherent asymmetry. Also note that the side-wall is present on different side of turbine for T2 and T3 with respect to rotation direction.

Recovery in the superwake near the hub region of the TriFrame and its comparison with single turbine is shown in Fig. 6.17. The average over a disc of diameter D_{avg} ($D_{avg} = 1.1D$ for streamwise velocity and $D_{avg} = 1.4D$ for TKE) and along the axis of the turbine was obtained for the quantities (see Fig. 6.17 (a)). Averaging diameter was chosen based on the gradients of quantities in the radial directions. Discontinuity in averaged quantities in the streamwise direction, especially for (c) the streamwise derivative, is found at the joint location of the near-wake and far-wake simulations. To avoid possible misconceptions, the corresponding parts are removed in the plots. In (b), the spatial average of streamwise velocity over the disc is normalized using

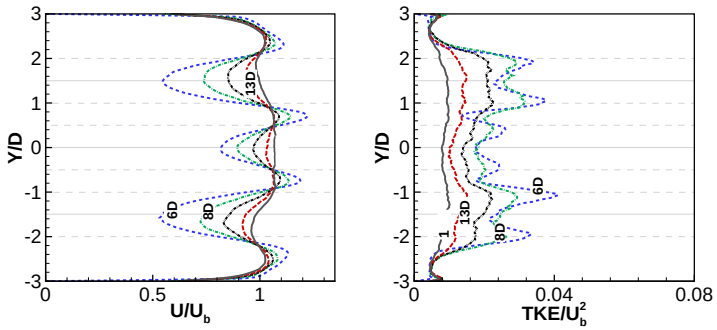

(a) (b)

Figure 6.12: Profiles of (a) time averaged streamwise velocity and (b) TKE in far wake of TriFrame of turbine at several downstream distances (as labeled on plot) measured from the location of first row turbine (T1).

the corresponding value at 1D upstream of the concerned turbine. Among the three TriFrame turbines, the upstream T1 turbine recovers much earlier than the T2 and T3 turbines. The two downstream turbines are, however, similar in recovery (within 2%) to that of the single turbine case. As evident in the plot of recovery rate (c) (obtained by taking the streamwise derivative of the values in velocity recovery plot (b)), the most significant difference in recovery rate is between 1D and 4D downstream of the turbines, i.e., just after the the second row of turbines in the TriFrame are encountered by T1 turbine. Beyond 10D, the rate of recovery for all turbines is slow and comparable to each other (9-12% of maximum recovery rate of T1 turbine). The disc-averaged TKE plot (d) in the wakes of the turbines reveals a similar trend. The two downstream turbines of TriFrame, T2 and T3, and the single turbine have TKE levels within 2% of each other throughout the wake but T1 turbine wake has dampened TKE levels in the near wake. However, in the far wake (beyond 10D downstream), the TKE levels for all turbines are similar (within 3%).

6.4.3 TriFrame deployment in an array

A large scale power producing array of turbines can be constructed by deploying multiple TriFrames of turbines at a site. This means successive TriFrames are in the wake of preceding ones. Since the power production by axial hydrokinetic turbines is proportional to the cube of incoming velocity, a speedier recovery of the wake means better

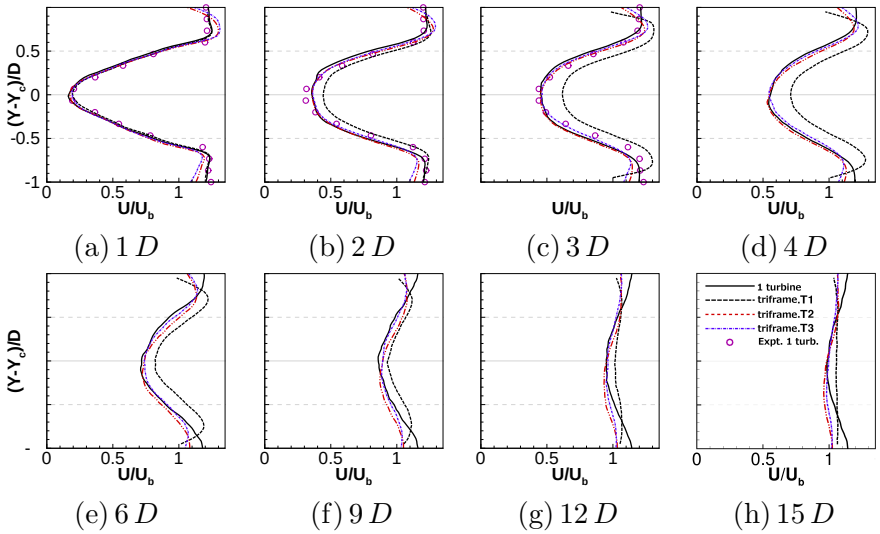

(a) 1 D (b) 2 D (c) 3 D (d) 4 D

(e) 6 D (f) 9 D (g) 12 D (h) 15 D

Figure 6.13: Comparing wakes past turbines in TriFrame with the wake past isolated single turbine. Streamwise velocity comparison downstream from the position of turbine in a horizontal plane at the turbine hub height (a) through (h). *1 turbine* is from isolated single turbine simulation and *Expt. 1 turb.* is from corresponding experiment. (Y_c denotes Y coordinate of the center of the turbine.)

performance for the downstream TriFrames. From the above results of the simulations, it is clear that each of the turbines in the TriFrame has different wake characteristics. Fig. 6.16 describes the averaged spatial evolution of their wake and differences with single turbine. The flow accelerates between the two downstream turbines resulting in an early recovery of the upstream T1 turbine compared to the single turbine wake. Table 6.2 compares the percentage of upstream velocity, averaged over a disc (see Fig. 6.17(a)), recovered for each of the turbines at distances 5D, 8D, 10D and 15D downstream of turbine. At 5D downstream of the turbine, T1 turbine has recovered 81% of the incoming flow whereas the isolated turbine wake has recovered only 70% by this distance. Due to the slowing recovery rate (Fig. 6.17(c)) it takes another 5D (total of 10D downstream) for the single turbine to recover up to 81%, at which point T1 turbine has recovered approximately 90% of the upstream value.

Consider two TriFrames placed in an array in an aligned manner as shown in Fig. 6.18. For the second TriFrame $\Delta 2$, the incoming velocities for T4 is lower than T1 (of first TriFrame $\Delta 1$) by fractions listed (as percent) in column 3 of Table 6.2. Similar

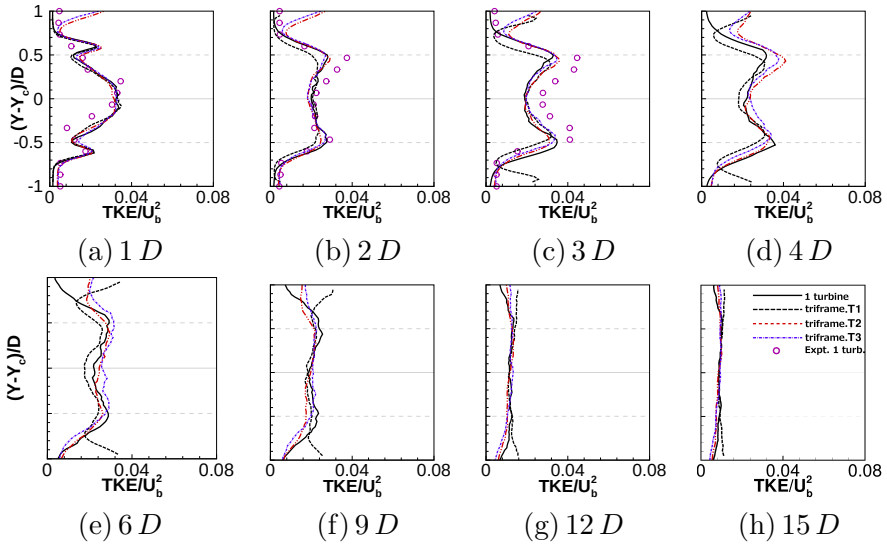

(a) 1 D (b) 2 D (c) 3 D (d) 4 D

(e) 6 D (f) 9 D (g) 12 D (h) 15 D

Figure 6.14: Comparing wakes past turbines in TriFrame with the wake past isolated single turbine. TKE comparison downstream from the position of turbine in a horizontal plane at the turbine hub height (a) through (h). (Y_c denotes Y coordinate of the center of the turbine.)

fraction for T5 over T2 and T6 over T3 is in the next column. The fifth column in the table $(P_{T4} - P_{ST2})/P_{ST2}$ represents the amount of additional power that T4 turbine of TriFrame $\Delta 2$ generates as compared to ST2 turbine a of single turbine array instead of TriFrames ($P_{\#}$ denotes the power produced by turbine/TriFrame index # as shown in Fig. 6.18). If the distance between the successive units (x) is 5D, the upstream turbine (T4) of second TriFrame ($\Delta 2$) can generate up to 37.9% more power. Owing to different velocity recovery, the power production of a single turbine in the wake (ST2 in Fig. 6.18(b)) will be different from that of the turbines in array of TriFrames (T4 - T6 in Fig. 6.18(a)). The last column in Table 6.2 gives the error in TriFrame power production estimate (of $\Delta 2$) if the individual turbine wakes of the TriFrame $\Delta 1$ were simply modeled as single turbine wakes. If the spacing between successive TriFrames is 5D, this error could be up to 17%. However, if the spacing is large (15D), less than 5% error in power production results.

The fluctuating components of velocities in the incoming flow are responsible for fatigue loading on the turbine blades. Long term exposure to fatigue loading compromises the structural integrity of the turbine with severely damaging effect on its performance

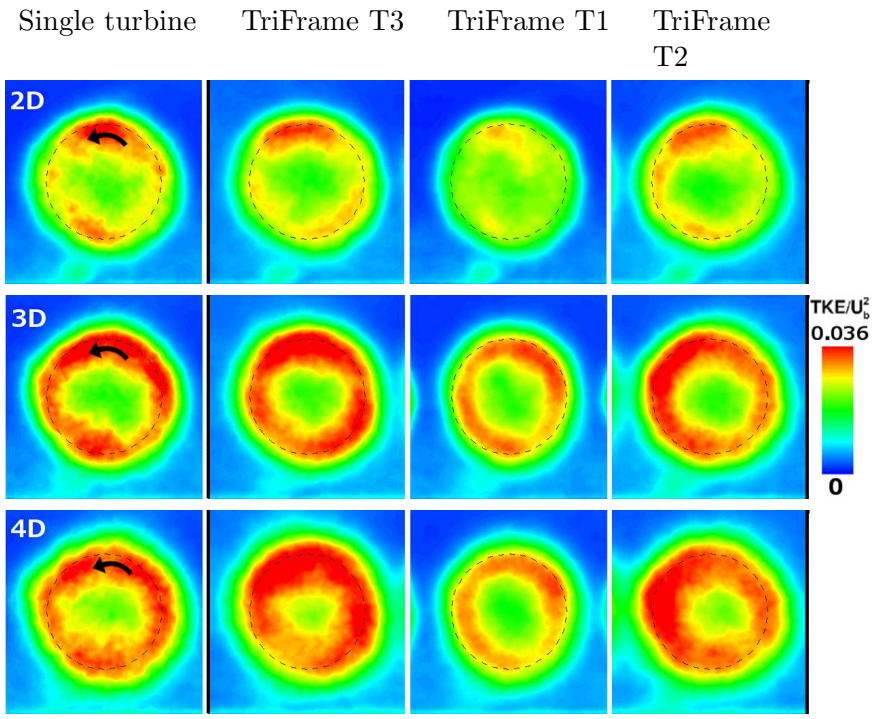

Figure 6.15: TKE contours on wall-normal (Y-Z) planes perpendicular to flow at $2\,D$, $3\,D$ and $4\,D$ downstream of turbines. Arrow shows direction of rotation for all turbines and dashed circle marks projection of area swept by turbine rotor. TriFrame turbines T1, T2 and T3 are as defined in Fig. 6.2. Channel side-walls are indicated by black lines on contour figures for T2 and T3.

and safety. Therefore, it is important to analyze the turbulence in the incoming flow for the turbines in an array. Even if the incident flow on first turbine (or first TriFrame) of the array has little to no incoming turbulence, the rotating turbine produces significant levels of turbulence for the downstream turbines of the array. In case of a TriFrame of turbines, lower levels of TKE in the wake of T1 turbine were observed as compared to the single turbine (ST1) wake (see Fig.6.17(d)). The disc averaged TKE at 5D for T1 wake is 10% lower than that of the isolated turbine. At 10D, the averaged TKE for all turbines (T1, T2 and T3) are 4% lower than the ST1 wake whereas at 15D they are within 2.5% of the corresponding ST1 value. We therefore demonstrate that for an array deployment of MHK turbines, the interaction between wakes has to be properly resolved in a TriFrame simulation to provide a better prediction of generated power. As seen in

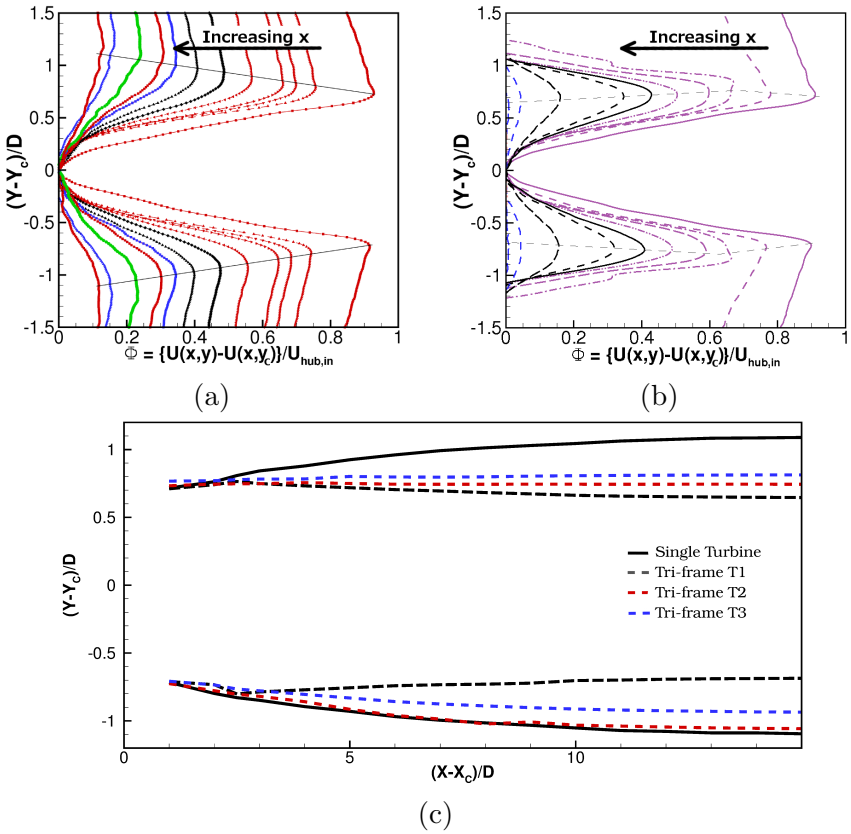

Figure 6.16: Special wake function plots for (a) Isolated turbine; (b) T1 turbine in TriFrame; (c) Boundaries of the turbine wakes computed using the locus of maxima of special wake function for all turbines. For turbines T2 and T3, negative ordinate values represent locations close to the wall and positive values are locations close to channel center.

aforementioned calculations of the power generation estimates (values in Table 6.2), the power produced by TriFrame of turbines could be underestimated if wake-interaction effects are unaccounted.

Simulation	X/D range	Y/D range	Z/D range	N_x	N_y	N_z
TriFrame: Near	[0,9]	[-3,3]	[0,1.87]	592	521	184
TriFrame: Far	[8,20]	[-3,3]	[0,1.87]	601	521	184
1 Turbine: Near	[0,9]	[-3,3]	[0,1.87]	592	521	184
1 Turbine: Far	[8,20]	[-3,3]	[0,1.87]	601	521	184

Table 6.1: Details of simulation grids used for TriFrame case and isolated single turbine (1 turbine) case. "Near" and "Far" denote near-wake and far-wake simulations, respectively.

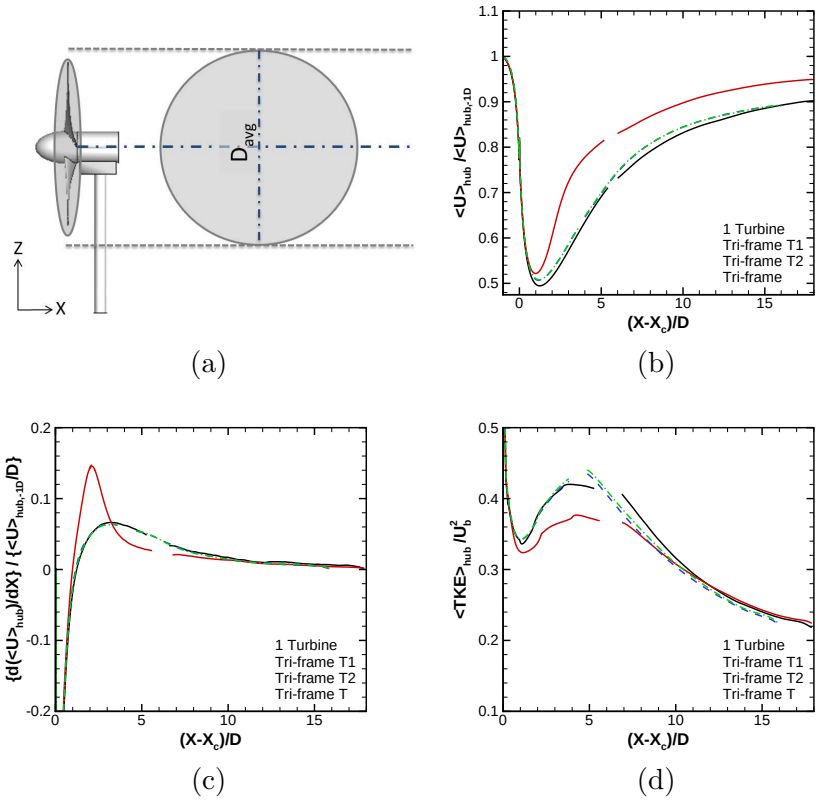

Figure 6.17: Characteristics of the TriFrame turbine wakes in comparison with the single turbine wake using the disc-averaged quantities. (a) A schematic showing computation of the disc-averaged quantities at spanwise-vertical discs with diameter $D_{avg} > D$ along the rotor axial direction at different streamwise locations, and (b) disc-averaged streamwise velocity ($D_{avg} = 1.1D$), (c) wake recovery rate computed using the disc-averaged streamwise velocity, and (d) disc-averaged TKE ($D_{avg} = 1.4D$) at different streamwise locations.

x	Single Turbine	TriFrame T1	TriFrame T2,T3	$\frac{P_{T4}-P_{ST2}}{P_{ST2}}$	$\frac{P_{\Delta 2}-3\times P_{ST2}}{P_{\Delta 2}}$
5D	69.1%	81.0%	69.7%	37.9%	17.0%
8D	79.1%	86.8%	80.7%	24.7%	11.2%
10D	83.1%	89.7%	84.4%	20.5%	8.7%
15D	85.5%	93.8%	88.8%	16.0%	4.7%

Table 6.2: Recovery of velocity in the wakes of different turbines at downstream distances 5D, 8D, 10D and 15D from the turbine. P_{T4} and $P_{\Delta 2}$ denote power produced by T4 turbine and total TriFrame power of $\Delta 2$, respectively, for a second downstream TriFrame in the wake. $P_{\#}$ denotes the power produced by turbine/TriFrame # as in Fig. 6.18. (See A for evaluation of P_{T4}/P_{ST2} and $P_{ST2}/P_{\Delta 2}$)

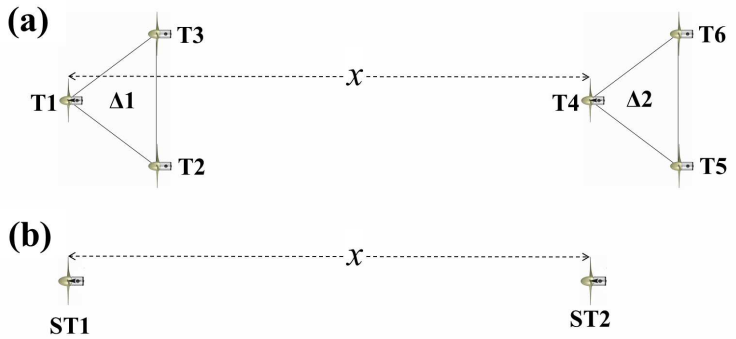

Figure 6.18: Array of MHK turbines consising of (a) TriFrame configuration with TriFrames $\Delta 1$ and $\Delta 2$ and (b) single turbines ST1 and ST2 separated by x distance.

Chapter 7

Field scale simulation of hydrokinetic turbine array in East River, NY

In this chapter the details of a field-scale study of MHK turbine array in natural marine environment is discussed. The study is part of a National Science Foundation's partnership-for-innovation project for the deployment of hydrokinetic turbine array in the East River in New York City by a small company, *Verdant Power Inc.* This project is formally known as the *Roosevelt Island Tidal Energy (RITE)* (see www.theriteproject.com). The electric power produced by the array is proposed to be supplied to the Roosevelt island. It is the first MHK energy project to be licensed by the Federal Energy Regulatory Commission (FERC) (License number 12611) to produce grid-connected electricity.

energy from the channel.

7.1 The Roosevelt Island Tidal Energy (RITE) project

The map in Fig. 7.1 shows the FERC licensed boundary, within which, the turbines are to be installed. Verdant Power has developed a Kinetic Hydro-Power System (KHPS) turbines that will be used to extract These turbines are $5\,m$ in diameter with three

Figure 7.1: A map showing the RITE project boundaries where the turbines of array are to be installed. Copyright of Verdant Power Inc. [12]

Figure 7.2: Deployment of KPHS turbines by Verdant Power at RITE site in the East River [12]

blades for the rotor. Fig. 7.2 shows images from successful deployment tests of KHPS at the RITE site. The rated power generation capacity of these machines is 56; kW which varies with the actual water velocity at any given instant. The nominal generated power in the doployment tests was reported to be around $35\,kW$ [12] They have successfully performed deployment of individual turbines and TriFrame at the site. The proposed plan is to deploy up to 30 turbines in the East Channel of the East River in several phases with constant testing and environmental monitoring. Each triangle represents proposed location of a TriFrame of turbine in multiple stages from A to C. Underwater cables from each unit connect to the onshore controls which connect to the electric grid.. The average annual production from the array is estimated to be between $1680 - 2400\,MWh$ [12]. The electricity produced will power the buildings on the Roosevelt Island through the grid.

7.2 Description of the river site

The deployment site for the RITE project as ascertained under the FERC license was a reach of the East Channel of the East River. A part of this reach was chosen for simulations. For the purpose of the simulations, bathymetry data from an old survey (Survey-H11353) by National Oceanic and Atmospheric Administration, U.S. Department of Commerce (NOAA) in 2004, is initially used. This survey provided data on

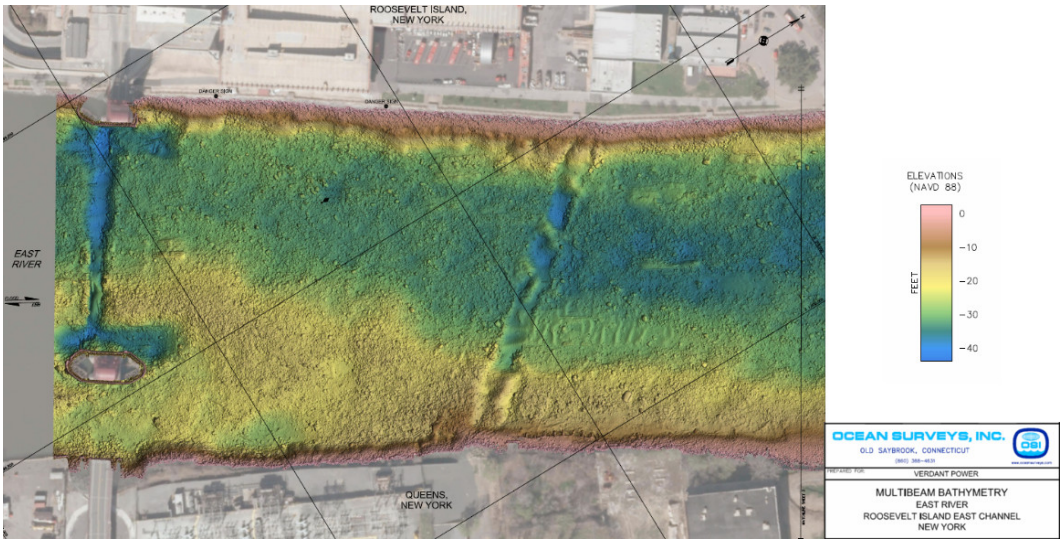

Figure 7.3: Detailed bathymetry survey of a section of East Channel of the East River performed by Ocean Surveys Incorporated (OCI) in 2015.

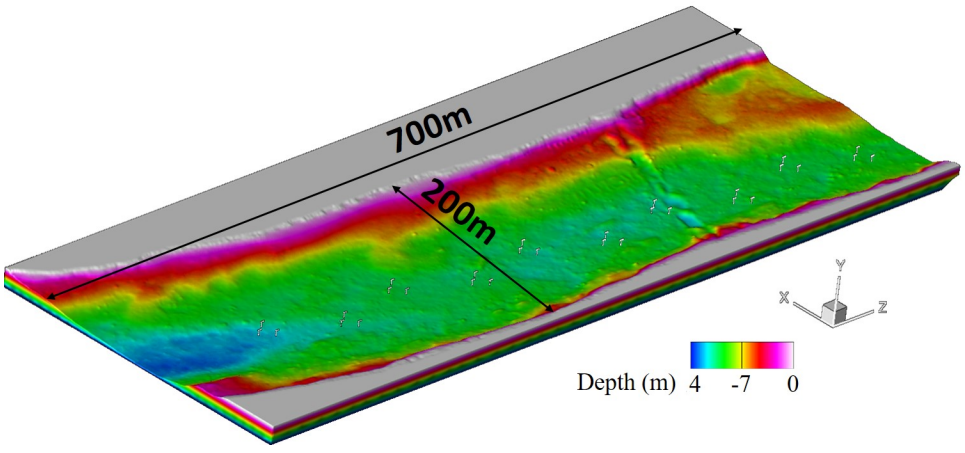

Figure 7.4: Digital elevation model of the channel section to be simulated

a grid of $2\,m \times 2\,m$. A more recent high-resolution bathymetry survey, on a grid of $0.5\,ft \times 0.5\,ft$, was performed by a vendor Ocean Surveys Incorporated (OCI) in 2015. The results of this survey are as shown in Fig. 7.3. Using this bahtymetry survey a digital elevation model of the river was created. Some areas where survey data was discontinuous, were truncated and/or interpolated to provide continuous and smooth elevation. The simulated reach and the digital elevation model are shown in Fig 7.4. The reach is $720\,m$ long and $200\,m$ wide. The width of the channel in this reach varies between $320\,m$ and $180\,m$. The flow depth varies between $2\,m$ and $13\,m$. Most common depth over the reach is approximately 10m.

East River is a tidal channel which means that it starts and ends in ocean and the flow is driven by the tides. The flow is pulsating with a time period of 12 hours. Thus, the flow direction is changing every 12 hours. In spite of pulsating nature of the flow, it is possible to treat the flow as unidirectional for the purpose of our study for the following 2 reasons: (1) the time scale (12 hours) of flow pulsation is much larger than the time taken for the hydrodynamics within the simulated section to attain a steady state; the simulations were run for a total of $900\,s$ and (2) the turbines in the flow are allowed to yaw so that they are facing the primary flow direction. The tidal channel bed is made of rigid bed-rocks.

7.3 Simulation of East River with baseline flow

In this section we performed the river flow simulation at the nominal inflow value without the inset turbines. The baseline simulation will provide a reference of river flow to see the effect of installing the array of turbines in the river. The unstructured Cartesian grid refinement method, described earlier in section 4.6, was used to carry out the LES. The simulations results are then compared with the field measurement in terms of vertical velocity profile measured using Acoustic Doppler Current Profiler(ADCP).

7.3.1 Computational setup

A Cartesian box of size $720\,m$, $14\,m$ and $270,m$ in the streamwise (Z), spanwise (X) and vertical(Y) directions, respectively, was chosen as the computational domain. This digitally reconstructed section of river constitutes immersed boundary in computational

domain of the simulation. Necessary extrapolation of missing data points in the survey was done to complete the bathymetry. The shore-line for the river was extracted using ArcGIS mapping tool from a satellite map made available within the tool. This ensured that the physical shore-line of the river are accurately captured in the computational domain. The bathymetry was then extended outside of the river boundaries to span the computational domain in the XZ plane. Finite positive depth ($1\,m$) was assigned to on-shore region in the land. Lastly, the outlet boundary section was extended by extruding the outlet section by $100\,m$ in the streamwise direction so as to increase the total size of the domain by this amount. This was done so that the outflow boundary does not have any effect on the flow in the river domain because of the artificial reflections associated with Newman boundary condition. For the purpose of representation of results, this portion is always excluded since it is not part of the physical domain.

Fig. 7.5 shows the immersed boundary mesh of the river used in the computation. The background computational domain is also shown. The bottom bed was treated as rigid bed with no sediment transport since it is made of bed-rock. The sediment transport was not modeled in the flow. A wall modeling approach, as described earlier, was used for boundary condition on the bed. The side-walls of the domain do not take part in the solution of equation because of the immersed boundary between the fluid and the walls. At the inlet boundary of the domain, a fully developed turbulent inflow profile was specified. This was obtained in a precursory LES with periodic boundary conditions. The cross-section of the precursory simulation was same as the cross section at the inlet. Domain for this simulation was obtained by extruding the inlet cross-section in the streamwise direction. At the downstream outlet boundary of the domain, Newman boundary conditions were imposed for all three velocity components. The free surface of the river is treated as rigid lid.

The nominal flow rate in the river and representative velocity based on the ADCP-measurements by Verdant Power were approximated to be $3.28 \times 10^3\,m^3/s$ and $2\,m/s$, respectively. From the bathymetry survey, the modal depth in the channel is approximately $H = 10\,m$. Using the above values of velocity and depth, the Reynolds number in the river is 2×10^7 which is typical for environmental flows. The computational grid was discretized to have 360, 40 and 1036 cells in the X, Y and Z directions, respectively, and total of 1.49×10^7 grid cells. Grid points are distributed uniformly in all three

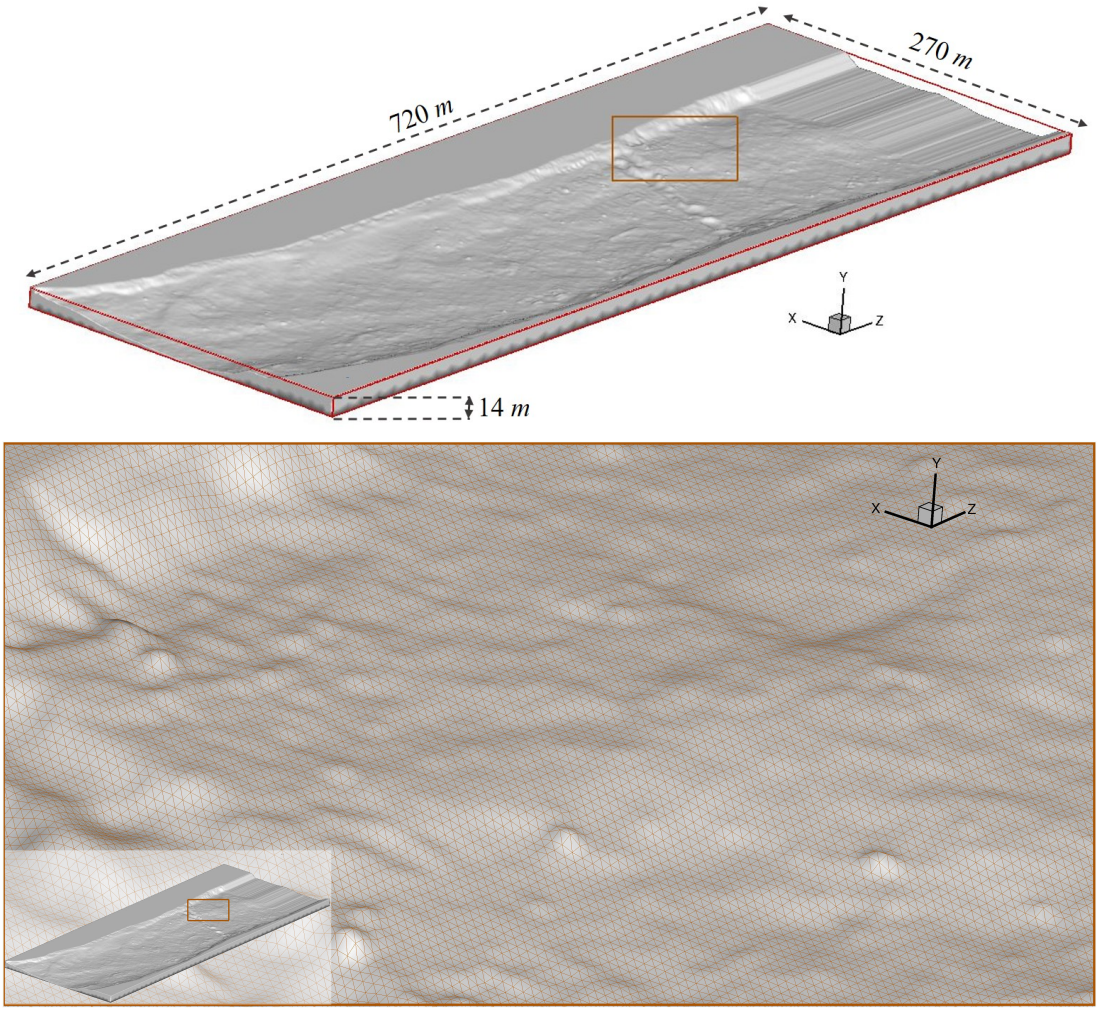

Figure 7.5: Top: Computational domain and immersed boundary. Bottom: Portion of river bathymetry represented as immersed boundary unstructured triangular mesh.

directions. The grid resulted in spacing of $0.75\,m$, $0.35\,m$ and $0.7\,m$ in the X, Y and Z directions, respectively. The non-dimensional time step was $\Delta t^* = 0.001$ where non dimensional time is defined as $t^* = tW_b/H$ where H is the representative flow depth and W_b is the bulk inflow velocity. This Δt^* gave a Courant-Friedrichs-Lewy (CFL) number is less than 1. The simulations were run until the total kinetic energy in the domain is converged. Subsequently, the flow-field was averaged for approximately 3 flow-through times where a flow-through time is defined as time taken to travel the streamwise extent of the domain at velocity W_b. The simulations were run on 264 processors of HPC clusters composed of Intel 2.4 GHz processors.

7.3.2 Results and comparison

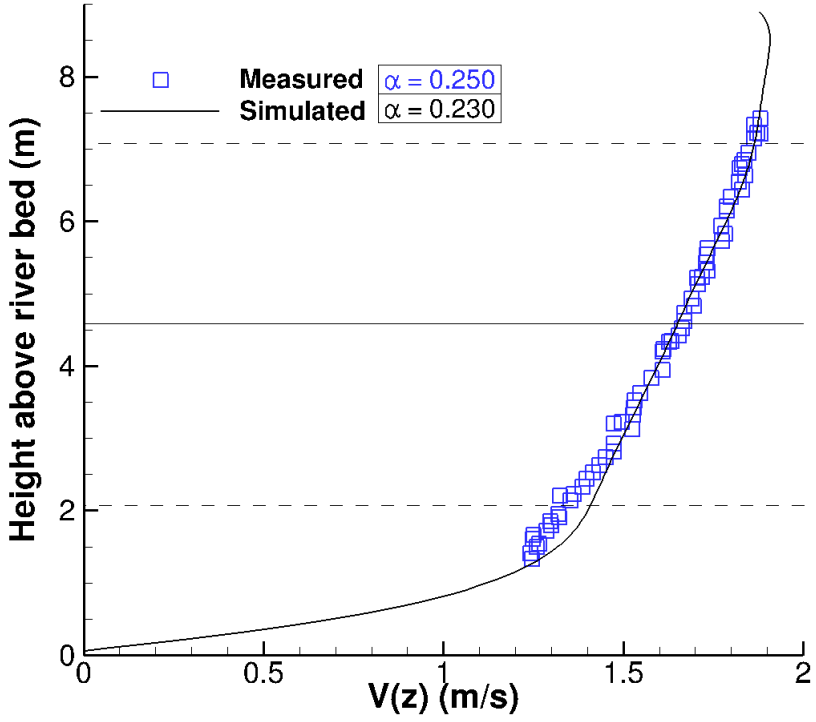

Figure 7.6: Comparison of computed and measured velocity in the East River. Horizontal solid line denotes hub-height position if a turbine were to be placed here. Dashed lines show rotor-tip position of the turbine.

The velocity profile was measured at a location in the river using ADCP along the depth, hereafter known as ADCP-N location at (588987.03 E, 4513118.35 N) in the Universal Transverse Mercator (UTM) coordinate system.Figure 7.6 shows comparison of computed mean velocity with the field measurements in East River provided by Verdant Power Inc. The computed time-averaged velocity profile obtained at ADCP-N location is shown with black line. The overall shape of the profile is in excellent agreement with the measured velocity profile. The power law ($u = Ay^{\alpha}$) index is $\alpha = 0.25$ for measured profile and $\alpha = 0.23$ for simulated profile. Near the top free surface, as expected, the velocity profile shows a dip. The velocity at the hub height of a turbine if it were to be installed at this location is $1.65\,m/s$. Unfortunately, due to the nature of site, it is extremely difficult to obtain detailed measurements (turbulence statistics, etc.) in the field. In the limit of available data and considering the variability of the processes involved, it can be argued that simulations are in good agreement with the measurements.

Average streamwise velocity contour plot at the free surface (Fig. 7.7) shows high velocity in the region where turbine-TriFrames are proposed to be installed. The instantaneous contours of the vertical (Y) vorticity show that the unique geometry of the river shoreline gives rise to the vortex shedding in the several regions of the simulated reach. More results for this case are shown in next section in comparison with the turbine array simulation.

7.4 Simulation of East River with the turbine array

In this section the LES of 10 TriFrame of axial hydrokinetic turbine inset in the river is performed. Using the Generation 5d (Gen5d) design of Verdent Power KPHS axial hydrokinetic turbine, an array of 30 turbines was placed in a section of East River as shown in Fig. 7.8 The Gen5d turbine are $5\,m$ in diameter and the hub height is 4.58 above the base of the tower. This height is fixed due to the construction of the tower component of the tower and is uniform for all turbines. The depth of the turbine is variable depending on the depth of channel at the individual turbine installation location. All turbines are installed in TriFrame units; the details of TriFrame arrangement is discussed in detail in Chapter 6. The geometrical configuration of turbines in a TriFrame

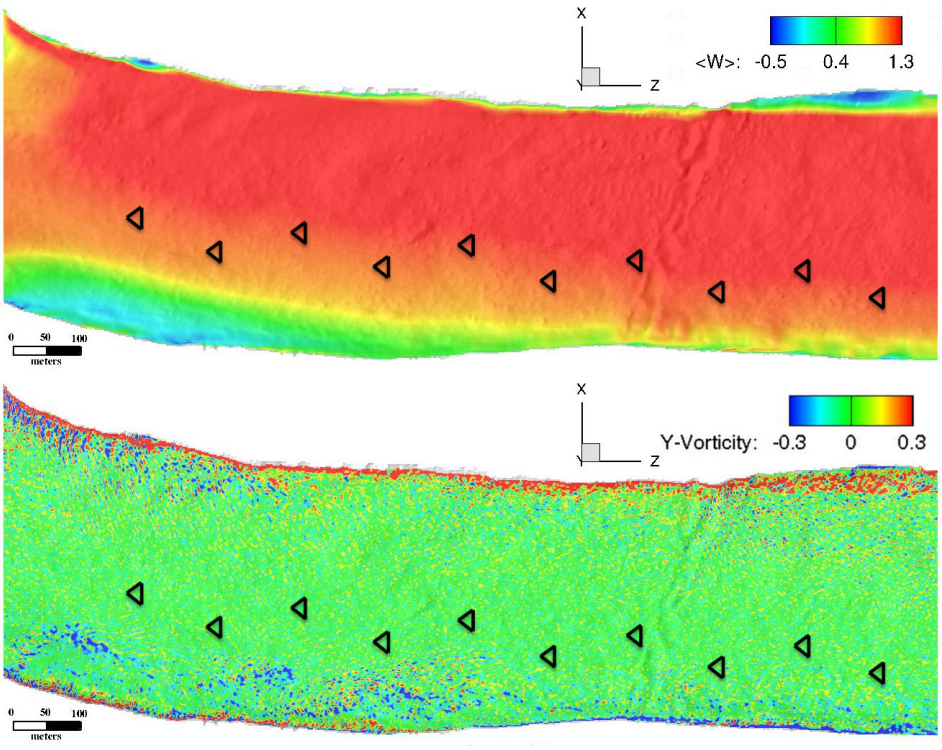

Figure 7.7: Contours of average velocity magnitude at free surface of East River. Blue triangle are proposed locations of TriFrames of turbines. (velocity is in m/s and verticity is in s^{-1})

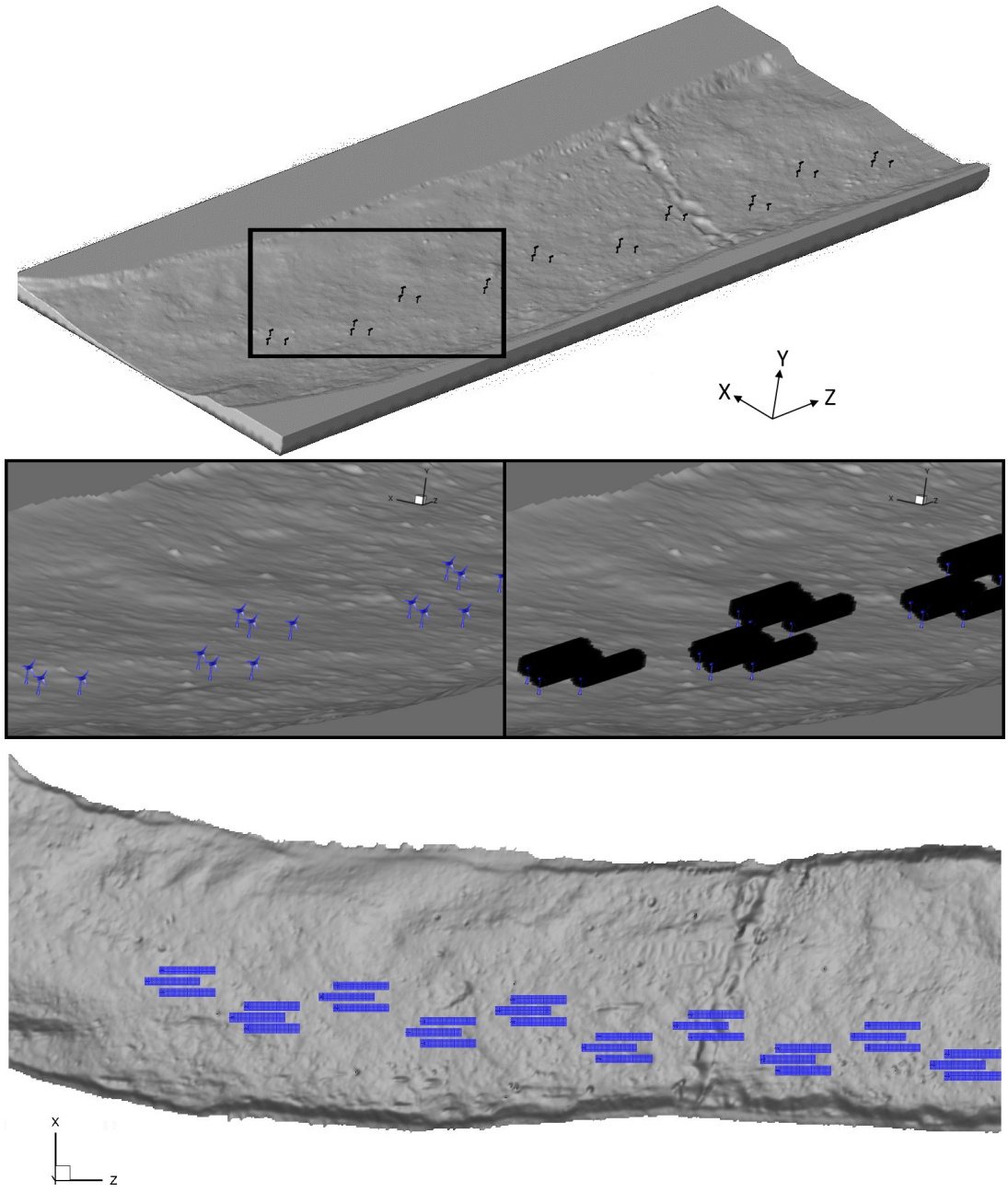

Figure 7.8: Contours of time-averaged streamwise velocity at free surface of East River. Blue triangle indicate the proposed locations of TriFrames of turbines. This simulation was done without turbine.

is shown in 6.1. The location of the TriFrame units was proposed based on the project proposal and is not shown here for copyright concerns.

The computational grid for this simulation is derived form the one used for baseline case in previous section i.e. the initial starting grid was a structured grid with 360, 40 and 1036 cells in the X,Y and Z directions, respectively. This grid was then refined locally so that higher resolution is obtained in the wake region of the turbines. The local refinement was cylindrical in fashion with the central axis of cylinder aligning with the center of the turbines. The radius of refinement region was 1.2 times the turbine diameter D. Refinement region extended from 1D upstream of turbine location to 7D downstream of the turbine. The grid refinement procedure added approximately 10^6 cells, resulting in the post-refinement grid having 1.59×10^7 number of Cartesian cells. The grid cells were all Cartesian and the cell aspect ratio was 2.1:1:2 for all grid cells. The local resolution in the turbine wake was $0.375\,m$, $0.175\,m$,$0.35\,m$ in the X, Y and Z directions, respectively, which corresponds to 14, 29, 15 points per turbine diameter. Such a grid resolution is known to acceptable results for the turbine modeled with actuator line model [3]. Details of the actuator line model are discussed in Chapter 4. The rest of the flow and boundary conditions were same as used for base line flow simulation in the Section 7.3.1. The simulation was run until the total kinetic energy in the domain is converged which happened in approximately 1.2 flow-through times. The flow-field was then averaged for another 5 flow-through times.

7.4.1 Results

Figure 7.9 shows the contours of time-averaged streamwise velocity at the free-surface of the channel. The results from the baseline simulation without turbines is also shown using the same contour levels for comparison. The baseline simulation shows that the velocity at free-surface is higher in the upper half (as per orientation in the figure) of the river. The velocity distribution is greatly affected by the strong deceleration in the lower left corner of the XZ plane in the figure. A strong wake with low velocity is observed. This particular flow feature is caused by the kink in the geometry upstream of the simulated section of the channel. It's effect on the simulated section is caused because of the shape of the precursory simulation for generating the inflow. The domain for inflow generation channel was generated by extrusion in the streamwise (Z) direction.

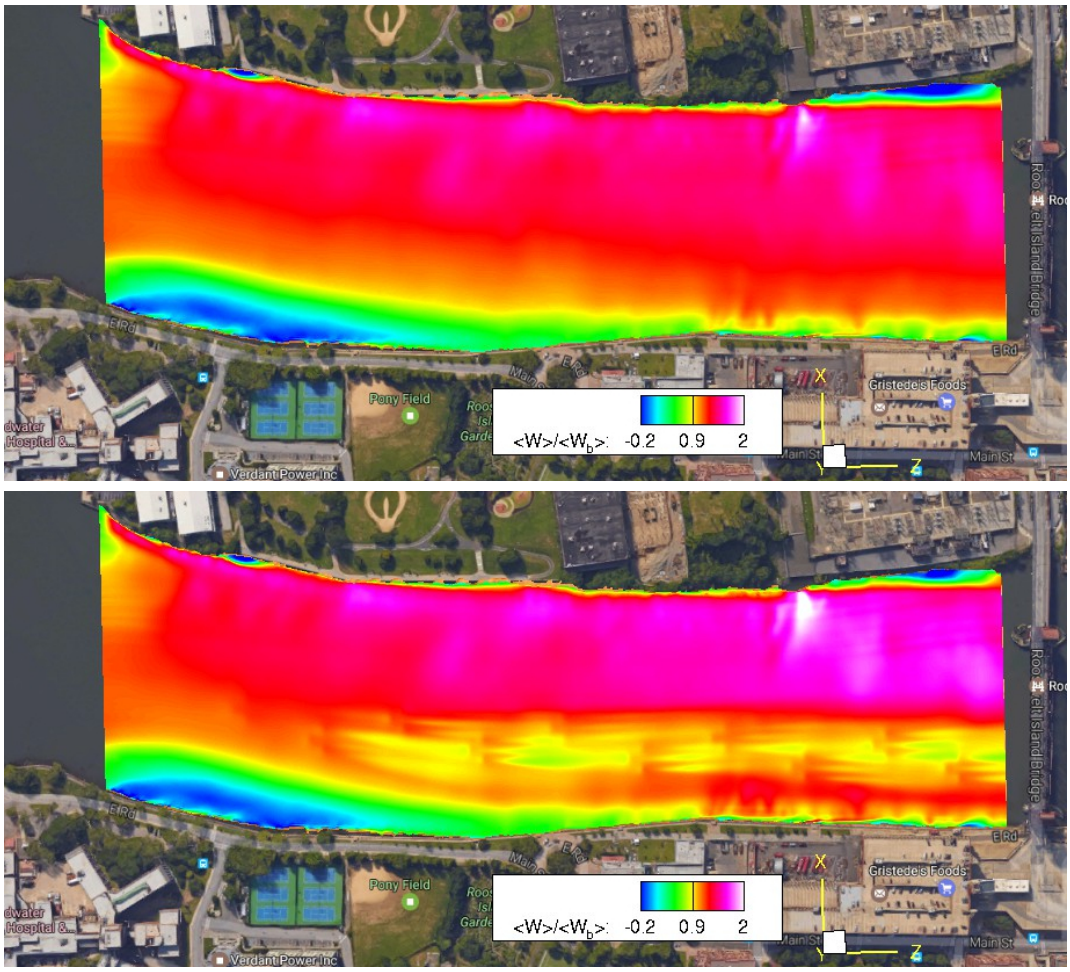

Figure 7.9: Contours of time-averaged streamwise velocity at free surface of East River (top) without turbine array and (bottom) with turbine array.

This is a reasonable approximation because the channel is upstream of the inflow section is straight at the end of curvature. This was necessitated because bathymetry data was available only for a limited channel reach. Ideally, the simulated channel reach should extend upstream of present channel. More bathymetry survey is required to better model the reach. The contours from the simulation with turbine array show a similar trend as the baseline case with high velocity in the upper half of the river. There is a weak signature of the turbine wakes shown as reduced velocity on the free-surface of the channel. This wake is more pronounced for the TriFrames in the middle of the array. The first 2 TriFrames barely show any effect on the free surface. The hub height of the turbines in these TriFrames is much lower compared to the other TriFrames. This is evident from the digital elevation model showing depth contour in the river (Fig. 7.4).

In the next two figures, Fig. 7.10 and 7.11, the contours of time-averaged velocity are shown in planes $7\,m$ and $5\,m$ below free surface. The hub of the upstream turbines are around $7\,m$ whereas the downstream turbines are around $5\,m$ In the top figure from simulation without turbines, a noticeable feature of the bathymetry is on the bottom-left corner where a ridge is seen to contribute to the slow velocity wake in this region discussed earlier. In both these sections $7\,m$ and $5\,m$ deep, the wakes of the turbines are clearly visible. The wakes of first 3 TriFrames, specifically the first and second, do not align with the axis of rotation. This indicates that the yawing mechanism of the turbines should turn them in the primary incoming flow direction which is not in Z directions for these turbines. The yawing mechanism was not modeled in present case, hence we see the wake alignment departing from the axis of rotation. The overall wake of the array suggests that the staggering of the 10 TriFrames is more efficient for energy extraction because of higher incoming flow momentum for the successive TriFrames.

Figure 7.12 shows the free surface of the river channel with time-averaged vorticity contours. Without the turbine array, there are no significant vorticity at the free surface for the scale shown here, except the vorticity generated by the wall. For the simulation with turbine array, the TriFrame seem to have very small effect on the vorticity values which is visibly only at the exaggerated scales chosen here. In Fig. 7.13 and 7.14, the time-averaged vorticity contours are shown at the XZ planes $7\,m$ and $5\,m$ below free surface of the channel. The wakes of the turbines show existence higher vorticity magnitude, which was absent when no turbines were installed. The vorticity magnitude

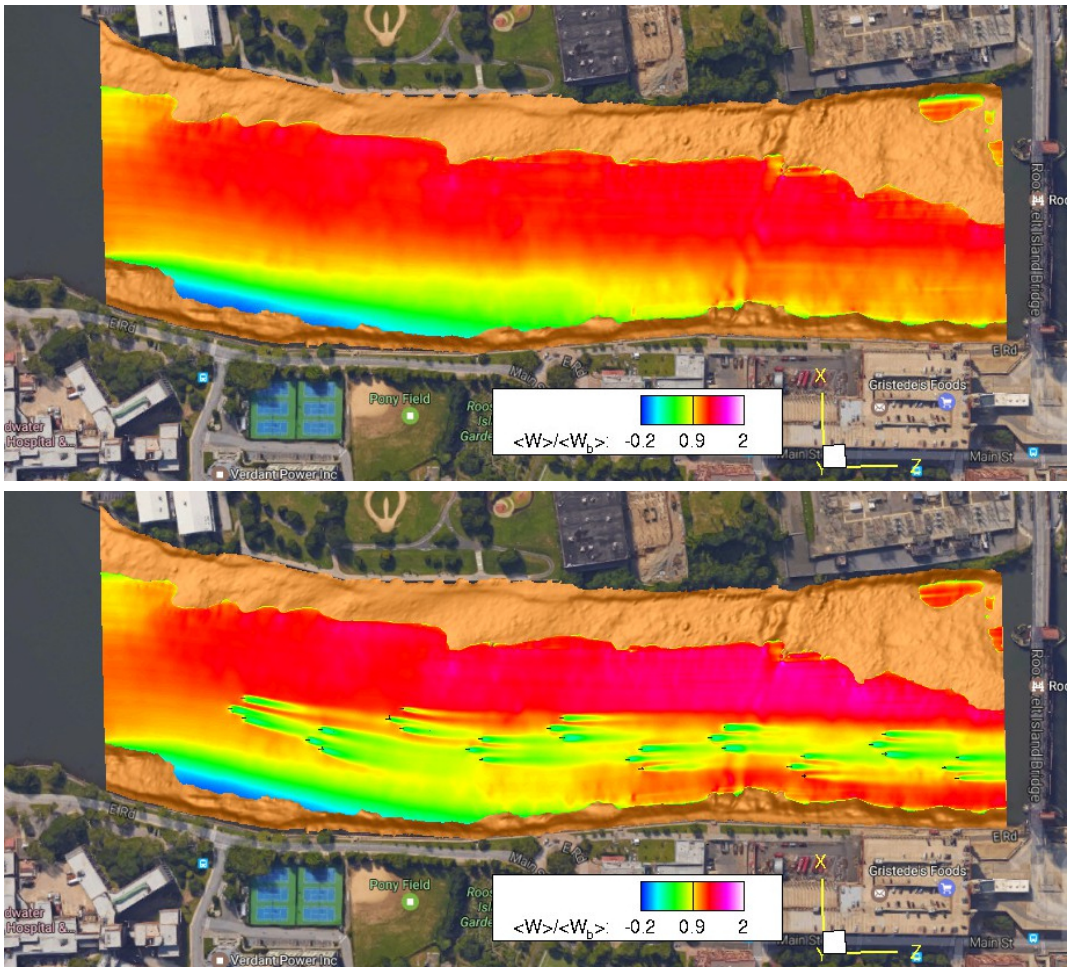

Figure 7.10: Contours of time-averaged streamwise velocity in an XZ plane at 7 m depth of East River (top) without turbine array and (bottom) with turbine array.

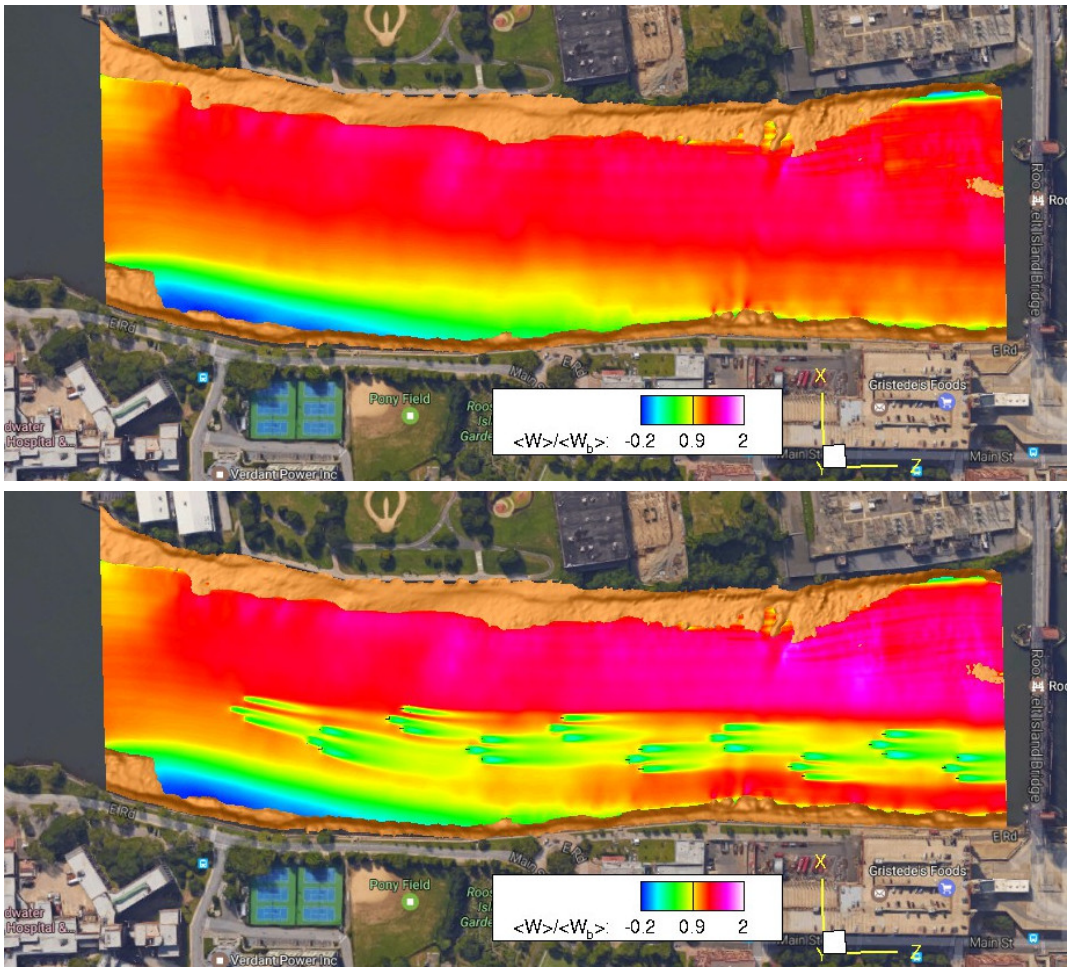

Figure 7.11: Contours of time-averaged streamwise velocity in an XZ plane at 5 m depth of East River (top) without turbine array and (bottom) with turbine array.

contours follow the low velocity wakes similarr to the streamwise vorticity distribution. Higher vorticity also exist near walls and other geometrical features in the river as seen in 7.14 near the downstream end of the channel.

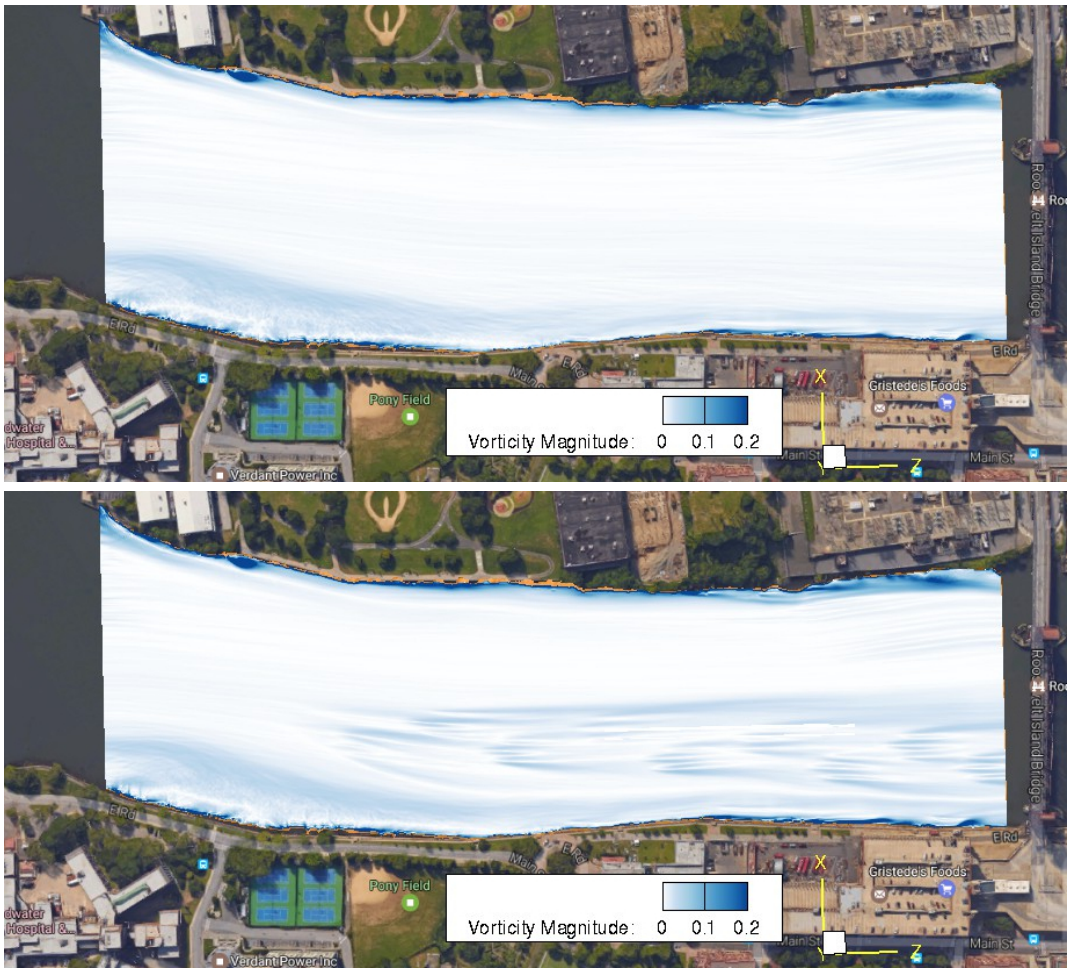

Figure 7.12: Contours of time-averaged vorticity magnitude normalized by W_b/D in an XZ plane at free surface of East River (top) without turbine array and (bottom) with 10 TriFrames of turbines installed.

Additionally, Fig. 7.15 shows contours of instantaneous streamwise velocity on a plane $7\,m$ below near at the hub-height of the first TriFrame. This contour plot shows the dynamics of the flow captured in the simulation. The large range of the scales present in the model can be seen. The $5\,m$-diameter turbine is orders of magnitudes

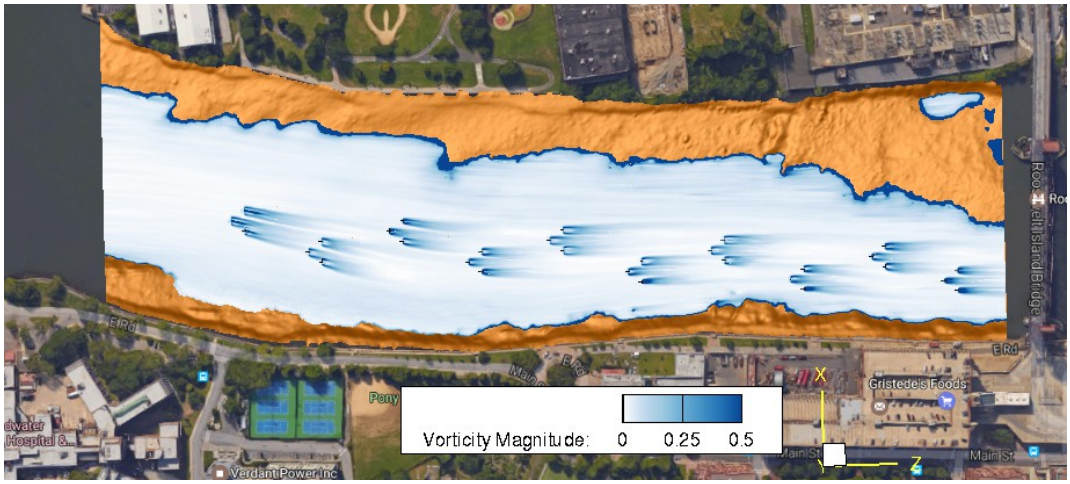

Figure 7.13: Contours of time-averaged vorticity magnitude normalized by W_b/D in an XZ plane at $7\,m$ depth of East River with 10 TriFrames of turbines installed.

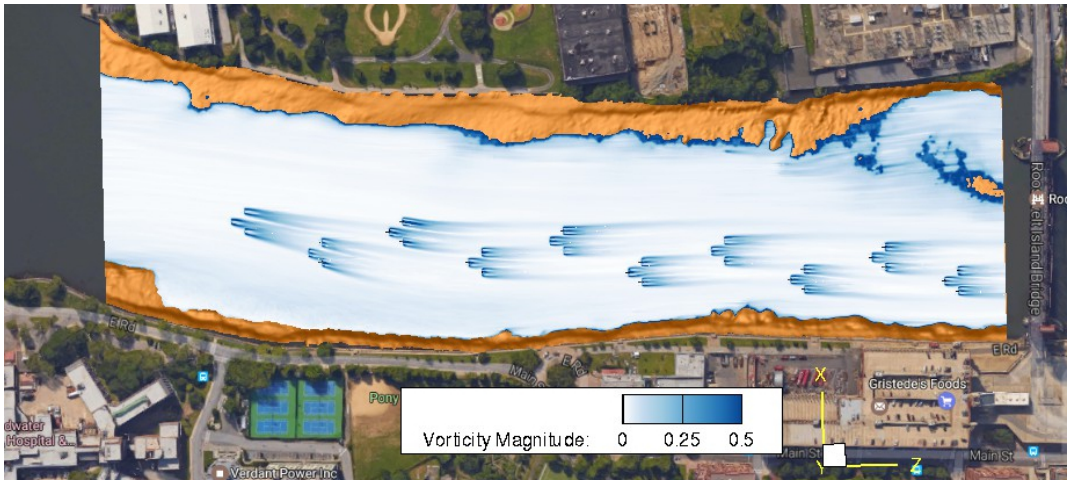

Figure 7.14: Contours of time-averaged vorticity magnitude normalized by W_b/D in an XZ plane at $5\,m$ depth of East River with 10 TriFrames of turbines installed.

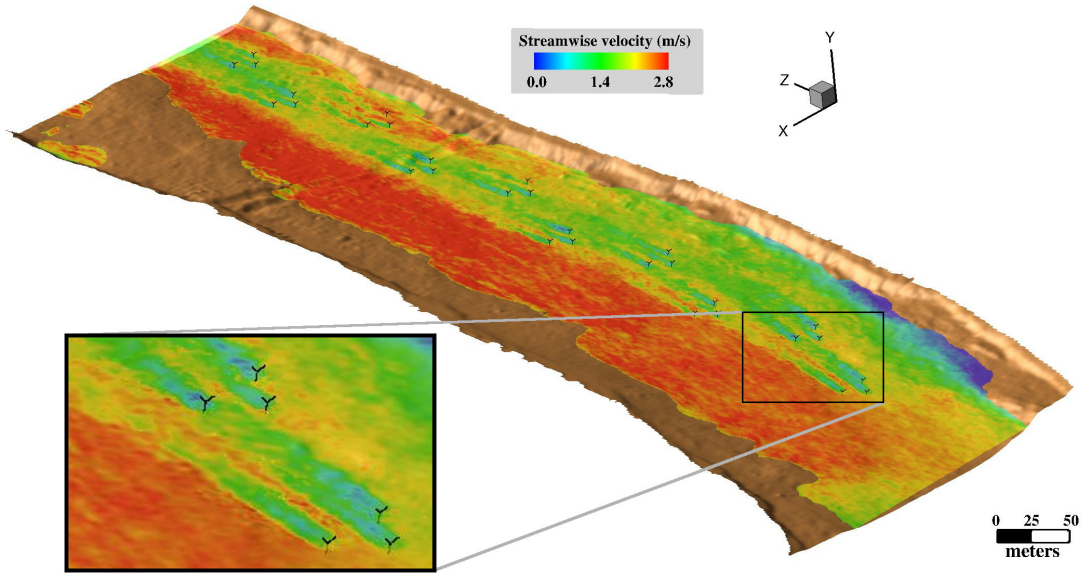

Figure 7.15: Contours of instantaneous streamwise velocity in an XZ plane $7\,m$ below the free surface of the East River with 10 TriFrames of turbines installed.

smaller than the dimensions of the river. Yet, the unstructured Cartesian grid enabled us to locally refine the grid and resolves the flow in the wake of turbines modeled by the actuator line model. The complex interaction of the scales resolved by the refined grid is shown in the inset figure for a smaller highlighted region. An uniform Cartesian with equivalent resolution in turbine wake would require 1.2×10^8 grid cells. Having faster calculation on such vast range of scales is only possible using multi-resolution modeling.

Chapter 8

Large eddy simulation of density current on sloping bed

Adapted from Journal Article:

Large eddy simulation of density current on sloping beds, Chawdhary, S., Khosronejad, A., Christodoulou, G., Sotiropoulos, F., *Physical Review Fluids*, 2017. (In review)

This research topic is not directly related to the title of the thesis but was performed as part of the Ph.D. as a separate research project and encompassed under the topic of environmental flow. The findings are discussed as an independent article in this chapter.

8.1 Introduction

Stratified flows, in the form of density (or gravity) currents, are capable of transporting material across long distances in natural geophysical flows. Such currents are formed as a result of mixing of fluids with differing density. The source of density difference could be either temperature difference, salinity, presence of suspended sediments or a combination of these factors. Examples of naturally occurring phenomena due to density currents include katabatic winds on the mountains, *haboobs* or dust storms, cold weather fronts under warmer air mass and thunderstorm outflow boundary [96]. Density current plumes

on sloping surfaces can arise in various natural and man-made situations. Currents of heavier bottom fluid commonly develop underwater on open slopes, spreading mostly laterally and sometimes vertically. They can also occur in rivers flowing into the ocean or industrial effluents merging in a river or lake, and advancement of saline under-currents in estuaries. Therefore, the study of density currents is important in evaluating impact of underflows on natural environmental flows and understanding of the conditions leading to their formation in nature.

The mixing due to density currents and its dynamics have been widely studied at laboratory scale under various conditions. These studies can be classified based on whether the density current develops on a horizontal plane or a sloping bed. Most commonly, density current is studied on a horizontal plane as a lock exchange problem, emulating a dam break wherein a vertical lock between two fluids of different densities is instantaneously removed. There are three separate phases of mixing following the lock release which are [97] (*i*) slumping phase, during which dense fluid slumps and moves with almost constant front velocity; (*ii*) inertial phase, during which flow is dominated by inertial and buoyancy forces; and (*iii*) viscous phase, during which flow is dominated by viscous and buoyancy forces. Hacker *et al.* [98] performed laboratory experiments with different aspect ratios of the lock and identified the density structures formed during the different phases of mixing. Breaking of Kelvin-Helholtz (KH) billows were deemed responsible for the spreading of stratified fluid from the density current head. Parsons and García [99] explored the similarity in density distribution in flow with higher Reynolds number. There are some early works which studied the two-dimensional (2D) gravity current on a slope (by continuously releasing a "line source" of dense fluid) on long gently sloping fresh-water flumes [100, 101, 102]. This action forms a dense underflow of gravity current spreading in vertical and streamwise direction, but is confined in the lateral direction. However, dense fluid released from a finite source on an open slope results in three-dimensional (3D) spreading, giving rise to a negatively buoyant plume, where lateral spreading is much more important than vertical (see Fig. 8.1). Experimental study on 3D spreading of density currents on slope was first performed by Hauenstein and Dracos [103] by releasing saline water from a point source on the sloping floor immersed in a fresh-water tank. Alavian [104] studied velocity and density distribution and the steady state plume-shape for different angles

of the sloping bottom bed. Several important conclusions regarding the structure of the plume were drawn most notable being the fact that the plume developed rapidly for some initial distance, and then became relatively constant in breadth. On mild slopes ($< 1/10$) the entrainment of ambient fluid was negligible and has well-defined plume boundaries. This study was followed by further experimental investigations of plumes on steep slopes only [13] wherein the behavior of density currents on an incline with respect to different parameters was systematically quantified. It was found that, unlike 2D gravity plumes, spreading of a 3D plume front is nonlinear. The spreading was highly dependent upon the buoyancy flux of dense fluid at the inlet, but only loosely dependent on inlet momentum flux. For similar inlet conditions, the spreading rate of the dense plume decreased with slope. With the help of experimental data and theoretical considerations, analytical expressions for the longitudinal and lateral spreading were developed. Choi and García [105] developed a relationship for spreading rate and verified it with their earlier experimental results (for slopes from 2° to 10°). Christodoulou and Tzachou [106] performed experiments for steep slopes to study unconfined 3D gravity currents at sufficiently high Reynolds numbers. The dense plume in all cases attained a "normal" width at some longitudinal distance after which the dimensions of dense current changed only marginally. This normal width correlated well with the buoyancy flux and reduced gravity. Using more experiments, Christodoulou [107] attempted to formulate the spreading laws relating the lateral and longitudinal spreading of plume in different regions of the dense plume. It was argued that the spreading laws do not depend on slopes for the range of slopes investigated (2° to 15°).

Laboratory experiments of density currents often require very large setups and sophisticated data acquisition equipment, whereas field measurements of 3D gravity currents are difficult to carry out because of their unexpected occurrence. Numerical simulations are effective tools for such problems but they are challenging due to the complex nature of these flows. A detailed anlysis of the dynamics of density currents' evolution is aslo possible owing to detailed temporal and spatial information from the simulated flow field. Following are some of the numerical investigations of density currents. Härtel et al. were the first to perform 3D direct numerical simulation (DNS) of the lock- release problem. The flow topology at the head of the dense current was analyzed to understand the lobe-and-cleft instability. The mechanism for instability formation was elucidated

with linear stability analysis. Cantero *et al.* [108] analyzed the propagation of the front of 2D and cylindrical gravity currents using highly resolved 2D and 3D simulations. The complex three dimensional structure nature throughout the head, body and tail of the current was identified. Tokyay *et al.* [109, 110, 111, 112] and Gonzalez-Juez *et al.* [113, 114] employed large-eddy simulation (LES) to investigate the interaction of gravity current past obstacles. Other notable 2D and 3D numerical works on lock-release gravity currents on a flat bed are [115, 116, 117, 118] and [119, 120, 121, 122, 123, 122, 124], respectively. Paik *et al.*'s [125] 3D unsteady Reynolds Averaged Navier-Stokes (RANS) simulations were also able to capture the intricate 3D flow structures such as the KH billows, breakdown of the billows (similar to the experiments of Hacker *et al.* [98]), lobe-and-cleft instabilities, and complex deformations of the density interface due to mixing. They noted that 2D approximation of density currents tend to under-predict the propagation of the dense front during the buoyancy-inertia regime. Tokyay and García [126] used LES to investigate the effect of inflow conditions on the propagation of density currents on mild (5%) slopes. The front velocity and structure of the current produced by continuous release of dense fluid from line source was studied. RANS modeling was used by Firoozabadi *et al.* [127] to simulate the density current plumes on extremely mild slopes. The steady state plume shape compared well with the experiments performed with sloping bed in a large tank. It was concluded from a large set of simulations and experiments that the inlet Richardson number has a profound effect on the structure of the density current. Other numerical studies on the density currents (on a slope) formed by a finite volume of fluid release instead of a continuous release [128, 129, 130, 131, 132]. However, these are not discussed here in detail since the focus of our work is density current formation due to continuous release (constant flux) of dense fluid from a finite source (as opposed to line source).

In this work we carry out LES of flow and density characteristics of 3D density currents down a sloping bed. We use the curvilinear framework which has been already extensively validated for buoyant [133] and non-buoyant [69, 37, 11, 29] flows. High-resolution LES in this work resolves intricate flow features and enable us to study the vortex formation at the genesis of a dense front near the inlet. This genesis is contrasted with an unstratified submerged jet to identify the role played by stratification on underflows. Frequency of large-scale structures is also identified via spectral analysis.

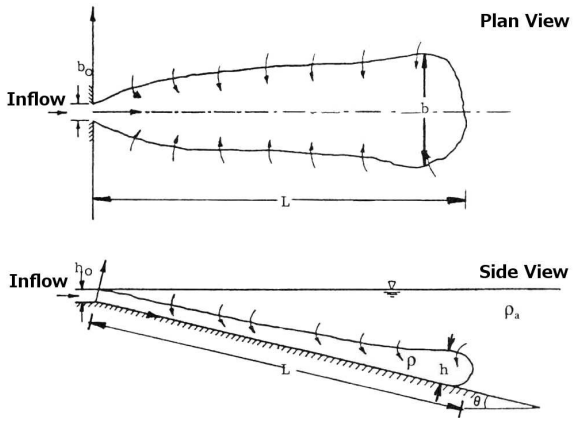

Figure 8.1: Schematic of a 3D spreading of negatively buoyant plume on a slope. Reproduced from Tsihrintzis and Alavian [13]

Remainder of this chapter is organized as follows. In sections 8.2 and 8.3, we describe the numerical method and experimental setup of the problem, respectively. This is followed by the description of the numerical procedure employed for the simulation in section 8.4. The results obtained from the simulation are subsequently discussed. Finally, we conclude the paper with a summary and discuss the areas of future research.

8.2 Numerical Method

We solve spatially filtered continuity and Navier Stokes equations with Bousinessq approximation to account for stratification. These governing equations, in which repeated indices imply summation while index values of 1, 2 and 3 correspond to X,Y and Z direction, respectively, are shown in non-dimensional form as follows [133]

$$J\frac{\partial U^j}{\partial \xi^j} = 0 \tag{8.1}$$

$$\begin{aligned}\frac{1}{J}\frac{\partial U^i}{\partial t} = \frac{\xi_l^i}{J}\{-\frac{\partial}{\partial \xi^j}(U^j u_l) + \frac{\partial}{\partial \xi^j}\left(Re\frac{G^{jk}}{J}\frac{\partial u_l}{\partial \xi^k}\right) - \frac{\partial}{\partial \xi^j}(\frac{\xi_l^j p}{J}) \\ -\frac{\partial \tau_{lj}}{\partial \xi^j} + Ri\,C\,(\frac{\delta_{i3}}{J})\}\end{aligned} \tag{8.2}$$

where $J = \left|\partial(\xi^1, \xi^2, \xi^3)/\partial(x_1, x_2, x_3)\right|$ is the Jacobian of the geometric transformation, x_3 is the vertical coordinate, $\xi_l^i = \partial\xi^i/\partial x_l$ are the transformation metrics, u_i is the i^{th} Cartesian velocity component, U^i=$(\xi_m^i/J)u_m$ is the contravariant volume flux, $G^{jk} = \xi_l^j \xi_l^k$ are the components of the contravariant metric tensor, p is the pressure, τ_{ij} is the sub-grid stress (SGS) tensor arising when LES filter is applied [29], δ is the Kronecker delta. Additionally, C is the concentration of dense fluid in volume fraction defined as [69]:

$$C = \frac{\overline{\rho} - \rho_o}{\rho_s - \rho_o} \tag{8.3}$$

where ρ_s is the density of the dense fluid at inlet, ρ_o is the ambient fluid density (the density of water at $20°C$ in the present case) and $\overline{\rho}$ is the density of the mixed fluid. All quantities in the equations are appropriately non-dimensionalized using ρ_o, u_{in}, the bulk velocity at the inlet and h_0, the height of the inlet. The non-dimensional numbers in the equations are Richardson (Ri) and Reynolds (Re) numbers, defined as:

$$Re = \frac{u_{in} h_0}{\nu}\ ; \qquad Ri = \frac{(\rho_s - \rho_o)}{\rho_o}\frac{g h_0}{u_{in}^2} \tag{8.4}$$

where ν is the kinematic viscosity of water at $20°C$ and g is acceleration due to gravity. The concentration field of the dense fluid is obtained by solving the following non-dimensional convection-diffusion equation:

$$\frac{1}{J}\frac{\partial C}{\partial t} = \frac{\partial}{\partial \xi^j}\left(Sc\frac{G^{jk}}{J}\frac{\partial C}{\partial \xi^i}\right) - \frac{\partial}{\partial \xi^j}\left(\frac{C U_j}{J}\right) \tag{8.5}$$

In the above equation, Sc is the Schmidt number of the dense fluid. Saline solution at $20°C$ was reported as $Sc = 700$ [134]. The SGS tensor (τ_{ij}), which appears after applying the spatial filter to the turbulence, is modeled using the Smagorinsky model [71]:

$$\tau_{ij} - \frac{1}{3}\tau_{kk}\delta_{ij} = -2\mu_t\overline{S_{ij}}, \tag{8.6}$$

where the eddy viscosity (μ_t) was further modeled by Smagorinsky as

$$\mu_t = C_s \Delta^2 |\overline{S}| \tag{8.7}$$

In Eq. (8.6) and (8.7), over-bar denotes spatial filtering operation, $\overline{S_{ij}}$ is the filtered strain-rate tensor, δ_{ij} is Kronecker delta, C_s is the Smagorinsky constant, Δ is the filter size (cube root of the grid cell volume in the present method) and $|\overline{S}| = \sqrt{2\overline{S_{ij}}\overline{S_{ij}}}$.

Smagorinsky constant C_s is dynamically calculated using the method of Germano *et al.* [31]. More details of the C_s calculation in the context of our numerical method can be found in Kang *et al.* [29].

The governing equations are discretized in space using a second-order central finite difference scheme and advanced in time using a second-order fractional step method [135, 29]. Iterative solvers implemented in Portable, Extensible Toolkit for Scientific Computation (PETSc) library are used for solving the discretized equations. Generalized Minimal Residual (GMRES) method is used to solve the linear system for the pressure-correction Poisson equation. Algebraic multigrid (AMG) is used as a preconditioner for the GMRES method to accelerate the convergence. The nonlinear discrete momentum equation is solved using matrix-free Newton-Krylov method. The inner iterations of the Newton-Krylov solvers also use GMRES method, but without preconditioning. The code is efficiently parallelized using PETSc library and Message Passing Interface (MPI) to exploit massively parallel computer clusters.

8.3 Experiments

Laboratory experiments have been carried out in the Hydraulics Laboratory of the National Technical University of Athens, Greece, using a bed at various slopes in a shallow $5m \times 7m$ tank. Details of the experimental setup and findings of those laboratory experiments have been published previously in [106, 107] and partially used in connection with numerical modeling efforts [136]. It was observed that the density currents show different characteristics depending on the slope and on the initial Richardson (Ri) and Reynolds (Re) numbers at the source. The most notable observation was that large-scale periodic disturbances resembling roll waves appeared for cases with low slope, low Re and high Ri. This is in agreement with similar observations by Tsihrintzis [137]. Two experiments were chosen for numerical simulation and are described in the following section.

8.4 Computational Details

We simulate two test cases denoted as cases A and B which correspond to experiments on slopes 5° and 15° to the horizontal, respectively. The computational domain consists of a shallow container with sloped bed ($L \times W$) inclined at θ degrees to the horizontal. Fig. 8.2 shows a schematic of the computational domain. As shown in Fig. 8.2, the width and height of the rectangular opening are $b_0(= 5cm)$ and h_0. Table 8.1 shows values of physical parameters for the two cases. Initially the domain is filled with ambient density fluid (water at $20\,^oC$). At $t = 0$, fluid that is slightly denser (saline water) is released from a rectangular inlet.

Case	θ	h_0 (cm)	u_{in} (m/s)	Q (cm^3/s)	$\Delta\rho/\rho$	L (m)	W (m)	Re	Ri
A	15^o	1.42	0.14	99.5	0.005	2	2.84	1989	0.03
B	5^o	1.17	0.085	50	0.030	4	3.51	1000	0.47

Table 8.1: Details of the two different cases in the present study. h_{in} represents the opening height of the inlet.

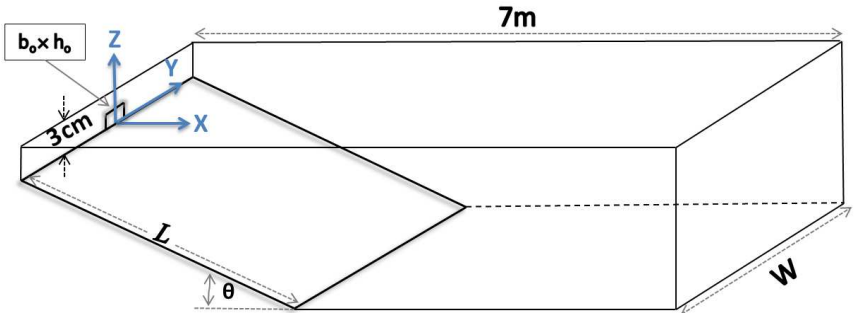

Figure 8.2: Schematic of the simulated cases. $b_0 = 5cm$ and h_0, L and θ are listed in Table 8.1

Case	N_x	N_y	N_z	Δz at inlet	u^*/u_{in}	Δz^+ at inlet
A	1301	841	51	$0.040\,h_{in}$	0.25	19.9
B	1501	501	71	$0.0143\,h_{in}$	0.47	6.72

Table 8.2: Grid details for cases A and B

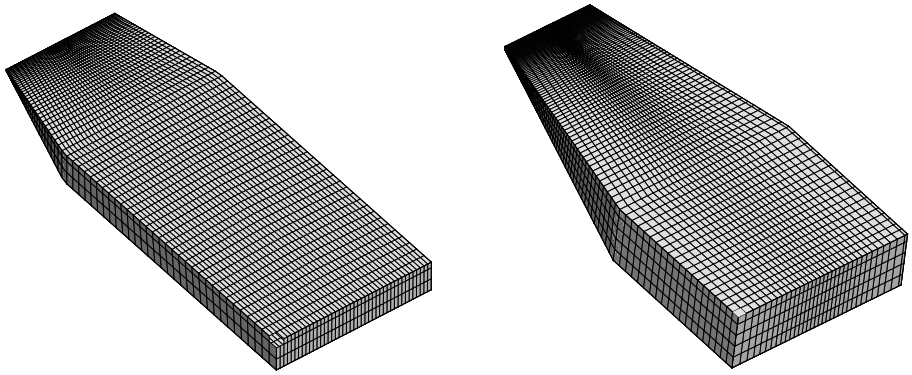

(a) Case A (b) Case B

Figure 8.3: Computational rid used for two cases. (a) Case A: every 20^th grid line is shown. (b) Case B: every 15^th grid line is shown. X:Y:Z is scaled to 1:1:3.

Body-fitted curvilinear grids were used in both the simulations. Table 8.2 gives details about the grids used in the simulations and Fig. 8.3 shows the grids. The grid lines follow the sloping bed in a diverging fashion to contain the density current plume to be generated. The horizontal portion of the tank follows at the end of the slope skewing the cells near the bottom of the slope. Grid points were distributed non-uniformly to cluster more points (in X and Y directions) near the inlet in order to capture the small scales produced as the buoyant flow enters the domain. The grid spacing was kept uniform in Z direction.

The inlet was fed with a uniform flow of volume flux Q introduced at $t = 0$. The top free surface boundary was treated as free slip. At the exit outflow boundary condition was used. The two side walls and bottom walls were treated as no-slip boundaries.

Simulations were run until time $t = T$, when the heavy density plume reached the far edge of the slope. At this time, a passive tracer was released, along with the denser fluid from the inlet. It was observed in the experiments that the plume shape of the tracer reaches quasi-equilibrium state ("steady state") after an approximate time $t = 3T$. Similar procedure was followed in the simulations to obtain the quasi-equilibrium shape of the tracer plume. That is, the simulations were carried out up until $t = 3T$ with the passive tracer introduced into the flow at $t = T$.

8.5 Results and Discussion

8.5.1 Plume shape at steady state

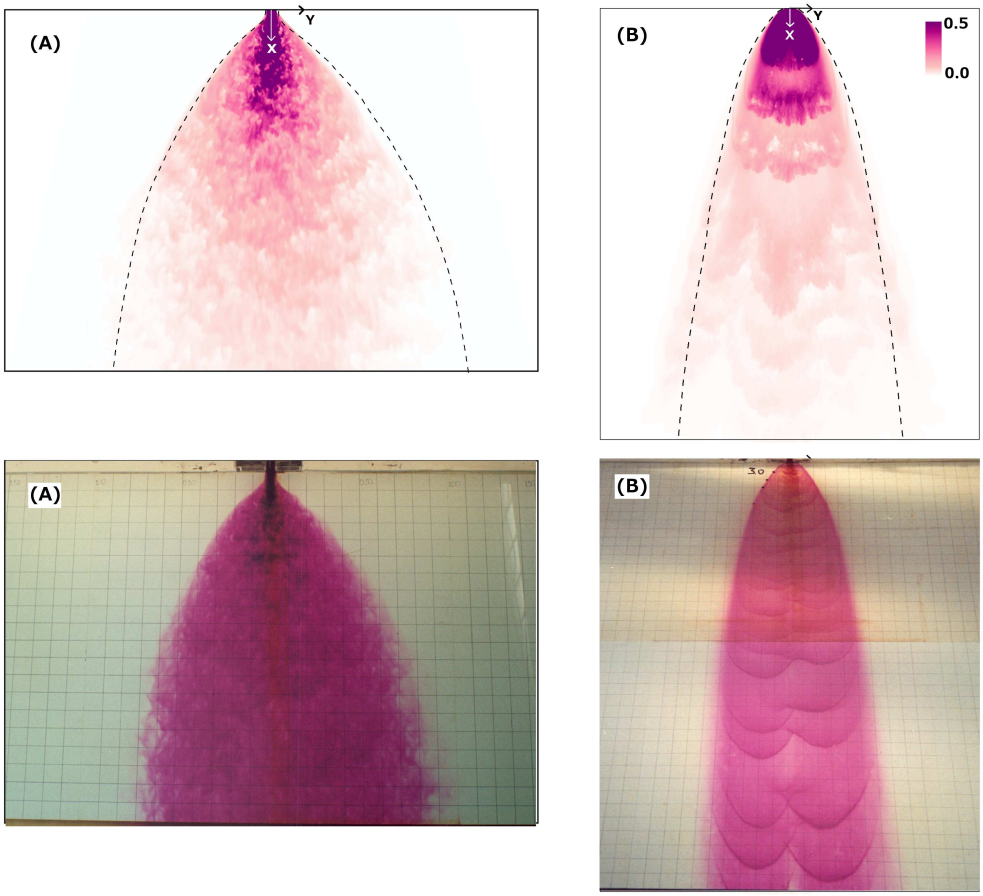

Figure 8.4: Comparison of computed (top) and measured (bottom) plumes at steady state for the two cases (as marked). Contours are levels of tracers released form the inlet. Dotted lines mark the shape of plume in the corresponding experiments. The contours in the computations denote the concentration of the dye in volume fraction.

Animations in Movie S1 and S2 show the computed instantaneous contours of tracer dye concentration released after quasi-equilibrium state of the dense plume is reached for cases A and B, respectively. The tracer contour levels in Fig. 8.4 show the computed shape of the density current plume on the slope for both cases. The dashed lines denote the visually identified boundaries from the corresponding experimental photographs.

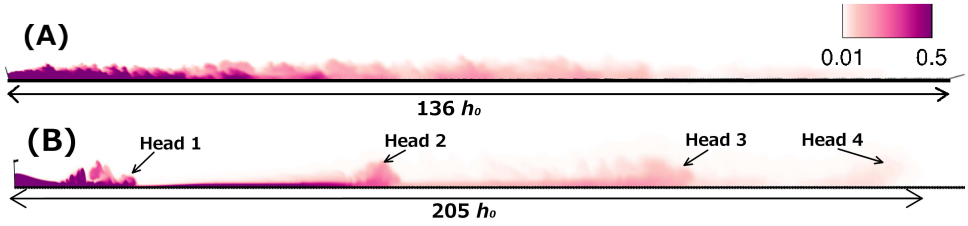

Figure 8.5: Tracer concentration contours in a cross-sectional $y = 0$ plane showing the structure of the current head $t = 200b_0/u_{in}$ after the tracer release was started. The contours denote the concentration of the dye in volume fraction. Contours in (B) are scaled 3 times in vertical direction for visibility.

When comparing the plume with experiments, it should be noted that an accurate comparison of contour levels with experimental images are not possible because of issues related to reproduction of corresponding dye visual. The plume shape and dye intensity in the experimental image is affected by the quality of ambient light, camera angle, and location. The color pixel at any point in the image is representative of the superimposition of all fluid elements from free surface to the bed. In order to plot the contours in simulation results, we obtained maximum dye concentration in the vertical direction for every point on the bed. In spite of the aforementioned limitations and approximations, for both cases, the simulated plume follows the experimental plume shape very well initially. However, for distances far from the inlet, the plume spreading is somewhat over-predicted. We also note that the experimental plume shape is slightly asymmetric in the Y-direction. This could be due to asymmetries or other spurious disturbances inherent in the experimental setup. The over-prediction of the current width away from the inlet was noted in previous numerical simulations with similar Richardson and Reynolds numbers ($Re = 1024, Ri = 0.28$) by Venetsanos *et al.* [136]. One striking difference observed between the A and B cases is in the range of scales of motion present in each case and visualized by the dye tracer. The case A appears to have multiple range of length scales, whereas case B shows prominent large scales which are approximately the size of the plume width. Due to this apparent difference in the range of scales, the density currents are often classified as either turbulent (case A) or laminar (case B) density currents. [106, 138]. This important difference between the two cases will be discussed further in subsequent sections of this paper. In Fig. 8.5,

the tracer concentration contours are plotted on the $Y = 0$ plane passing through the center of the inlet opening. The laminar case B shows multiple current heads which can be associated with the large-scale structures generated near the inlet (see subsection 8.5.5), and are compatible with the experimental observations mentioned in section 8.3.

8.5.2 Spreading of dense plume

As the dense fluid travels from the finite source (inlet opening) down the slope it entrains the lighter ambient fluid and spreads longitudinally as well as laterally while losing momentum. The nature of the spreading governing the equilibrium shape of the plume is dependent on several factors, such as bed slope angle (θ), Ri, Re, inlet buoyancy flux, and inlet momentum flux. The extent of lateral and longitudinal spreading of the dense plume on slope has been the subject of several studies [139, 107, 103, 13].

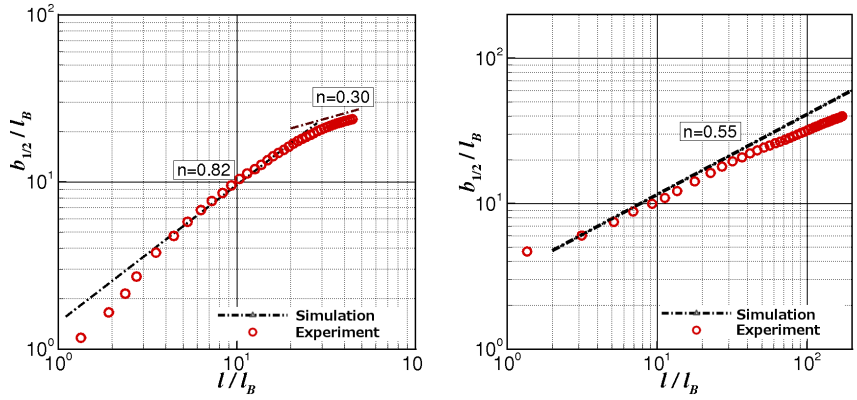

Figure 8.6: Spreading law for lateral spreading of the steady state dense plume. Left: Case A; right: Case B

Herein, we use our simulation results to obtain the shape of the plume and quantify its spreading rate. In Fig. 8.6, the computed plume half-width ($b_{1/2} = b/2$) is plotted as a function of the streamwise distance from the origin (l) in log-log scale. The lengths in Fig. 8.6 are normalized by the buoyancy length scale (l_B), which reads as follows:

$$l_B = (Q^3/B)^{1/5} \tag{8.8}$$

where $B = gQ\Delta\rho/\rho$ is the buoyancy flux at the inlet of the jet. For the conditions of the experiments A and B, the values of l_B are $4.58\,cm$ and $2.43\,cm$, respectively. Fig. 8.6

also includes our experimental results extracted from the dashed lines outlining the two plumes as shown in Fig. 8.4. Researchers have tried to extract a power law equation for the variation of plume's width versus its length, which in dimensionless form reads as follows:

$$\frac{b_{1/2}}{l_B} = A\left(\frac{l}{l_B}\right)^n \tag{8.9}$$

On a log-log scale, linear regions are identifiable in the plots, indicating the aforementioned power law. Based on the results of a large number of experiments on several slopes, Christodoulou [107] concluded that (i) at $l/l_B \approx 10$, the plume half-width reaches a value $b_{1/2}/l_B \approx 10$ irrespective of slope and source conditions; (ii) the power law indices expressing the lateral spreading as per Eq. 8.9 are estimated as $n \approx 1/3$ for $l/l_B > 10$ and $n \approx 1/2$ for $2 < l/l_B < 10$, being higher for larger slope. Using similarity arguments Hauenstein and Dracos [103] proposed a proportional relationship ($l \sim b$) between longitudinal and lateral spreading at steady state. However, the similarity solution has been invalidated theoretically as well as experimentally [105]. By means of theoretical considerations Horsch [140] showed that the spanwise width of a laminar density current flowing down an incline in the gravity-viscous dominated regime scales as the $7/9^{th}$ power of the longitudinal distance.

As seen in Fig. 8.6, the spreading results deduced from the simulation are in reasonable agreement with the respective experiments. In particular, in both cases the normalized half-width at $l/l_B = 10$ is very close to 10, i.e. the value suggested in Christodoulou [107]. The power law index $n = 0.55$ obtained from the simulation for case B is close to the value suggested for $l/l_B < 10$ in [107]. Additionally, the same value of $n = 0.55$ is found to hold for a dominant part of the range tested, including $l/l_B > 10$. On the other hand, the value $n = 0.82$ deduced from the case A simulation over most of the region ($2 < l/l_B < 28$) is quite close to the 7/9 power law suggested in Horsch [140]. Yet, it is considerably smaller than the experimental value for low $l/l_B < 4$. Another regime ($l/l_B > 28$), with $n = 0.30$ is identifiable at large distances, which is compatible with the suggested value of 0.33 [107].

The discrepancies between simulation and experiments at very low values of l/l_B, i.e. close to the source, can be attributed to small differences in the specification of idealized boundary conditions, such as constant velocity through the inlet as compared to real velocity non-uniformity in the experiment. At large distances, the experimentally

observed smaller rate of growth (which is consistent with an earlier numerical study [136]) may be due to a more predominant effect of bottom friction compared to the smooth wall assumed in the simulation, or even to inaccuracies in defining the visual boundaries at very low concentrations in the experiment.

8.5.3 Spectral analysis

Velocity time series data was collected for cases A and B on the plane of symmetry at several locations near the bed. Fig. 8.7 and 8.8 show streamwise velocity time series and its frequency spectra for these locations. At all four locations, the low frequency range show a constant decay of energy. For higher intermediate frequencies, the spectra exhibit $f^{-5/3}$ scaling, indicating the well-known inertial subrange, followed by fast decay in in the viscous dissipation region. The stretch of the inertial subrange region decreases as we move downstream. For case B, there is an identifiable peak in all of the spectra close to frequency $f = 0.05Hz$. This peak in frequency is better seen in the following Fig. 8.9. In this figure, we plot the pre-multiplied spectra i.e. frequency times power spectral density (PSD) of the streamwise velocity at four points for case B in the plane of symmetry, away from the bed but close enough to lie in the dense current. The streamwise distance and height above bed for the four points are - $(21h_0, 1.7h_0)$, $(33h_0, 2.0h_0)$, $(47h_0, 2.6h_0)$, and $(102h_0, 4.7h_0)$. In all four of the spectra considered here, the lowest frequency, corresponding to the largest structures, are the same (i.e. $St = 0.0122$). These structures are shed intermittently from the inlet, as could be seen in the movies S3 and S5, which visualize iso-surface of q-criteria (at $q = 0.01u_{in}^2/h_0^2$). One such large-scale structure is shown in Fig. 8.15 at $t^* = 30$ for stratified case.

8.5.4 Nonlinear time series analysis

The spectral analysis in the previous section shows appearance of pseudo-periodic large-scale structures (with $St = 0.0122$) shedding from inlet for Case B. Such coherent dynamics indicates potential for chaotic behavior in the system. Hence, the time series at point closest to inlet among all points for which time series was collected for case B, hereafter known as point B1, is subject to nonlinear analysis in order to determine *maximal Lyapunov exponent (λ)* for the system. It is a measure of separation rate of

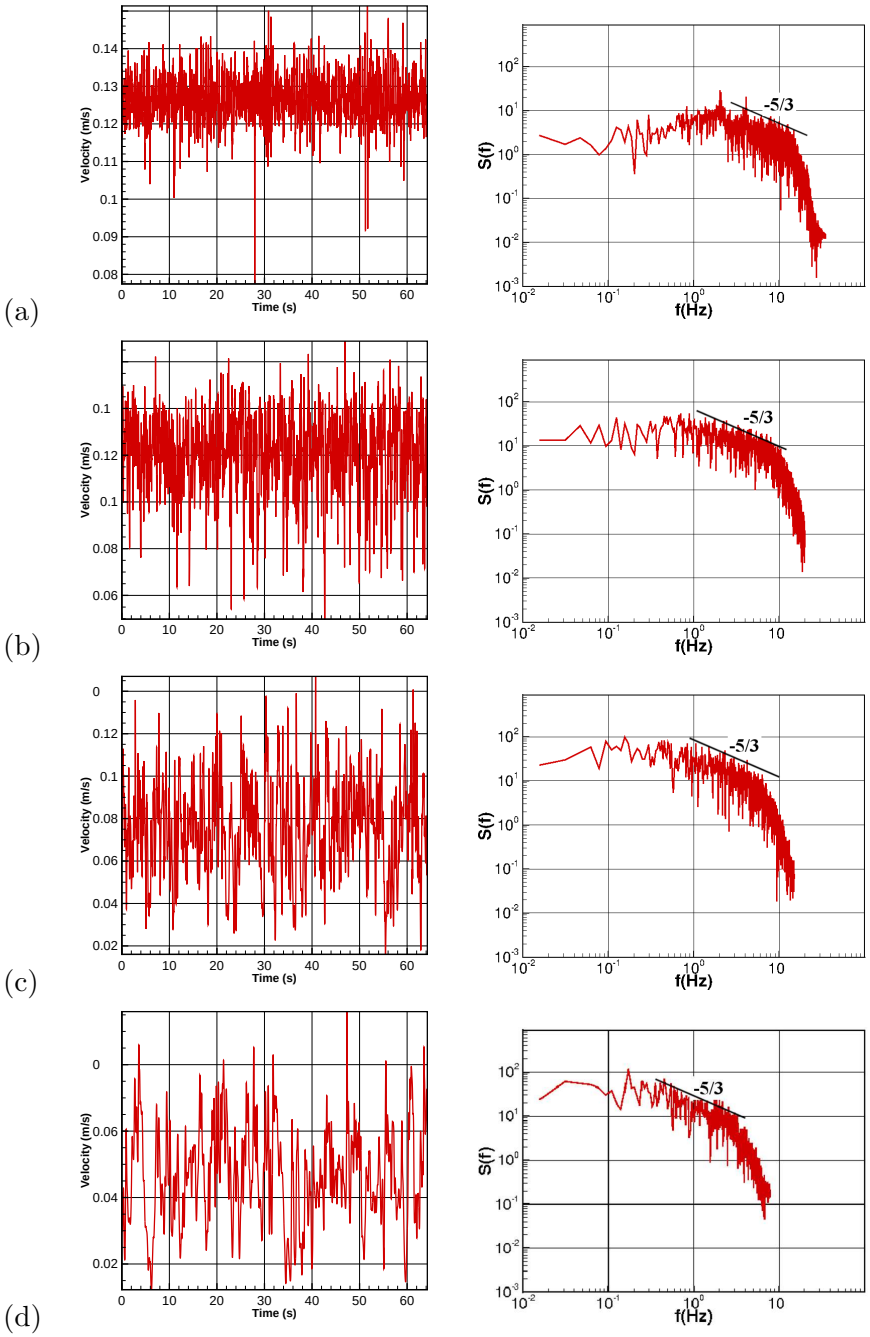

Figure 8.7: Time series and frequency spectrum of streamwise velocity at (a) $(6.3h_0, 0.37h_0)$, (b) $(13h_0, 0.54h_0)$, (c) $(22h_0, 0.78h_0)$, and (d) $(34h_0, 1.1h_0)$ for case A. The pairs denote streamwise distance and height above the bed.

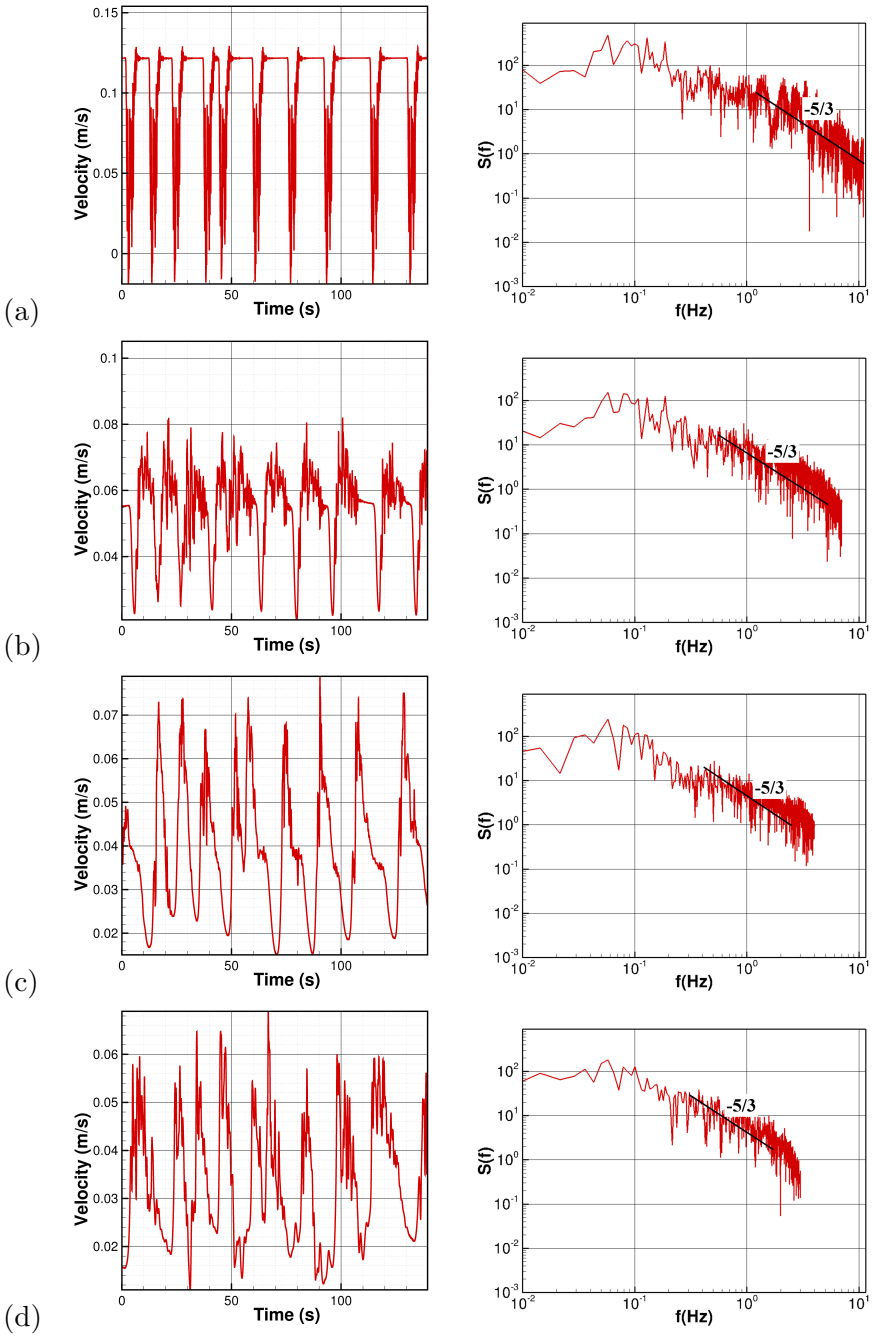

Figure 8.8: Time series and frequency spectrum of streamwise velocity at (a) $(12.5h_0, 0.22h_0)$, (b) $(33h_0, 0.35h_0)$, (c) $(65h_0, 0.55h_0)$ and (d) $(102h_0, 0.78h_0)$ for case B. The pairs denote streamwise distance and height above bed.

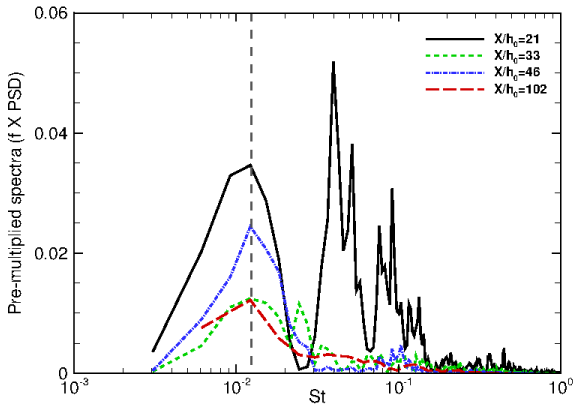

Figure 8.9: Pre-multiplied spectrum of streamwise velocity for four points in the dense plume showing prominent frequency of large-scale structures at $St = 0.0122$

trajectories in a phase space for a nonlinear system. Maximal Lyapunov exponent is used to ascertain the chaotic nature of a nonlinear dynamical system. A positive value of λ is signature of chaos. Packard *et al.* [141] argued that it is possible to obtain the phase space by measuring only a single observable using the method of delays. According to the method of delays, a phase space can be constructed by choosing phase coordinates given by:

$$[u(t), u(t+\tau)...u(t+(m-1)\tau)] \tag{8.10}$$

where τ is the time delay, m is the embedding dimension and $u(t)$ is time-series of streamwise velocity fluctuations. Both τ and m are quantities that need to be determined before estimating λ An optimum value of τ must be chosen to realize the correct phase space. Too small values of τ will give phase space vectors which are highly correlated with each other and hence do not provide new information (*redundancy* [142]). On the other hand, a value too large gives vectors that are seemingly uncorrelated (*irrelevance* [142]). We employ the method of "mutual information", as proposed by Fraser and Swinney [14], to determine the optimal value of time delay (τ) for phase-vector reconstruction. According to this method, optimal delay is one which provides new information with measurement of series $u(t+\tau)$, for a given series of $u(t)$. This is measured through the mutual information function $I(\tau)$. We use time series of streamwise velocity fluctuations $u(t)$ at the aforementioned point as the observable quantity. Using

this technique, values of mutual information (in bits) are plotted for different time delays in Fig. 8.10. The optimal lag is one corresponding to first minima in $I(\tau)$, in this case, for $\tau^* = \tau u_{in}/h_0 = 0.72$ for this series. For more details of the method, reader is referred to [14]. Next, the embedding dimension (m) is determined by plotting false nearest neighbors for various dimensions [143]. The true embedding dimension is one in which the false nearest do not decrease any further by choosing a higher dimension. In this case $m = 10$ reduces the false nearest neighbors to practically zero. But as we show later, the exact value of m does not significantly impact λ estimate (more so if we are interested in sign of λ). Hence, $m = 5$ is a good choice to proceed with analysis as it reduces the false nearest neighbors to under 10%. We come back to

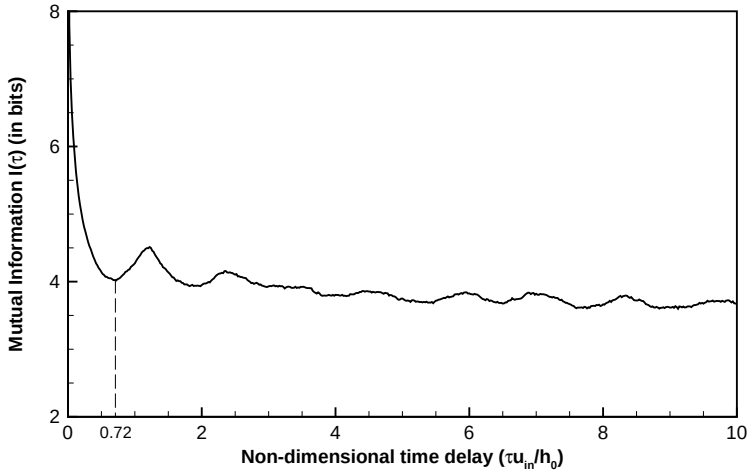

Figure 8.10: Mutual Information function for time-series at point B1. First minima on this plot gives optimal estimate of time delay [14].

explore the maximal Lyapunov exponent (λ) for the system. For any point s_n in phase space, the neighboring points at distance $\delta_0 < \epsilon$, become separated by become $\delta_{\Delta n}$ after Δn timesteps. In a chaotic system, this separation is exponential following an equation of form:

$$\delta_{\Delta n} \simeq \delta_0 e^{\lambda \Delta n}, \quad \delta_{\Delta n} \ll 1, \quad \Delta n \gg 1 \tag{8.11}$$

In the limit of $\delta_{\Delta n} \to 0$ and $\Delta n \to 0$, λ becomes invariant. To evaluate λ numerically, we employ the algorithm proposed by Kantz [144] which directly computes

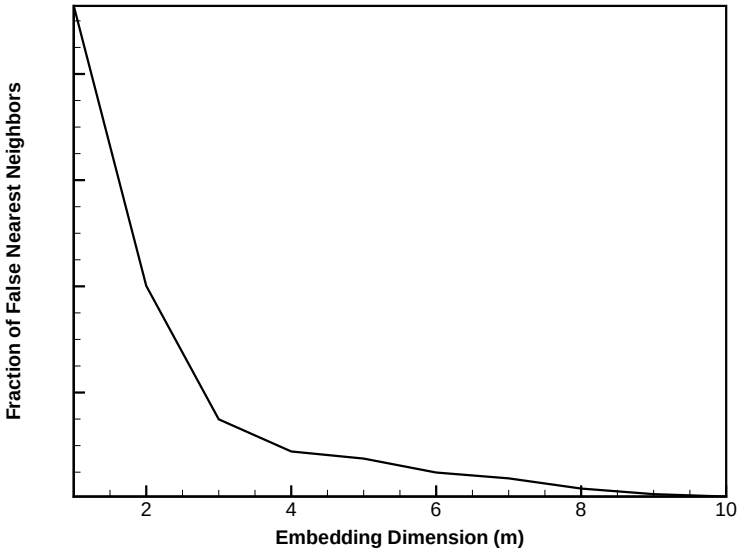

Figure 8.11: The fraction of false nearest neighbors as a function of the embedding dimension for time series at B1.

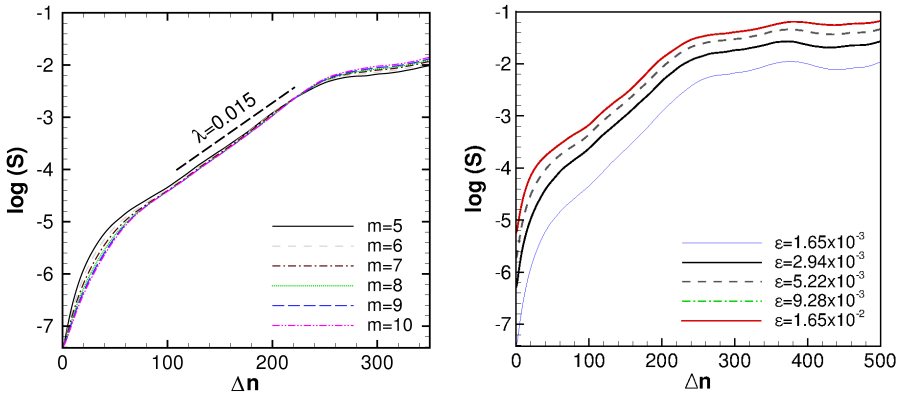

Figure 8.12: Estimation of maximal Lyapunov exponent for time series data at point B1. Log of average stretching factor vs time step for several embedding dimensions (left) and several ϵ neighborhood sizes (right). Linear portion in the plot represents exponential separation indicating $\lambda = 0.015$.

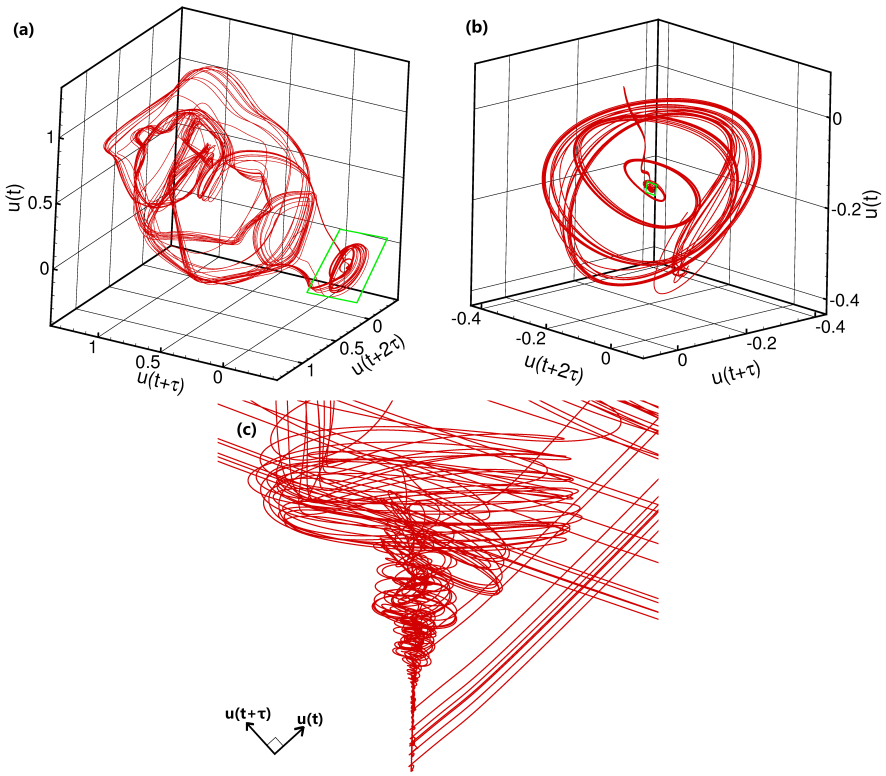

Figure 8.13: The time-delay reconstructed vectors are plotted in phase space. (a) and (b) 3D phase plot and (c) view of the attractor in a 2D plane. S6 (b) is the blow-up of green box in (a), while (c) shows the blow-up of green box in (b) in 2D.

the divergence of nearby trajectories in a time-delayed reconstructed phase space. Averaged separation distance over all the points are plotted for increasing Δn (Fig. 8.12). An exponential growth on this plot is indicated by a dashed line on the log-linear scale. To demonstrate the robustness of presence of linear region (and hence positive λ) in the system, we plot several values of m and ϵ. The linear portion in the plot can be well described by an exponential curve with exponent of 0.015 i.e. $\lambda = 0.015$. A positive λ and exponential separation supports the presence of chaotic regime.

The phase space resulting from time-delayed reconstruction consists of points as given by Eq. 8.10 for $m = 5$ and $\tau = 0.72$. 2D and 3D projections of phase space are plotted in Fig. 8.13. They all clearly show the existence of an attractor at approximately $u = -0.173$ units in all coordinates. Movie S6 further illustrates this attractor by following the time-series on 3D phase plot. In the movie, it is apparent that the phase space trajectories follow aperiodic path in twisted curves. In one particular view as shown in Fig. 8.13(c), the toroidal nature of the trajectories is visible. Furthermore, we plot the Poincaré sections in this view in two different planes in the phase space, P1 which passes through points (-0.1697 -0.1719, -0.1712), (-0.1724 -0.1721 -0.1697) and (-0.1725 -0.1698 -0.1709); and P2 which passes through (-0.16995, -0.16729, -0.16794), (-0.16987, -0.17221, -0.17139) and (-0.16914, -0.17129 , -0.16340). This Poincaré maps, as shown in Fig. 8.14 (a) and (b), resemble the ones obtained for chaotic cases in different problems studied in [16, 15] and reproduced in Fig. 8.14 (c) and (d).

Poincaré map plotted here is consistent with the others obtained for chaotic cases with a caveat that there are less number of points on this map than those shown from earlier works. A convincing way to strengthen the argument for multiple tori in phase space would be to have longer time-series data leading to more points in phase space and consequently denser Poincaré map. Due to the computationally expensive nature of simulations we could only run the simulation (and collect time-series) over limited time period corresponding to 1.5 flow-through times. (A flow-through time is defined as time taken by the heavy density plume to reach the far edge of the slope). Longer time series data is desirable but computationally expensive to obtain in the high fidelity LES. Nevertheless, with the available data, the Poincaré map and the phase portraits indicate the signature twisted tori which are characteristic of chaotic systems.

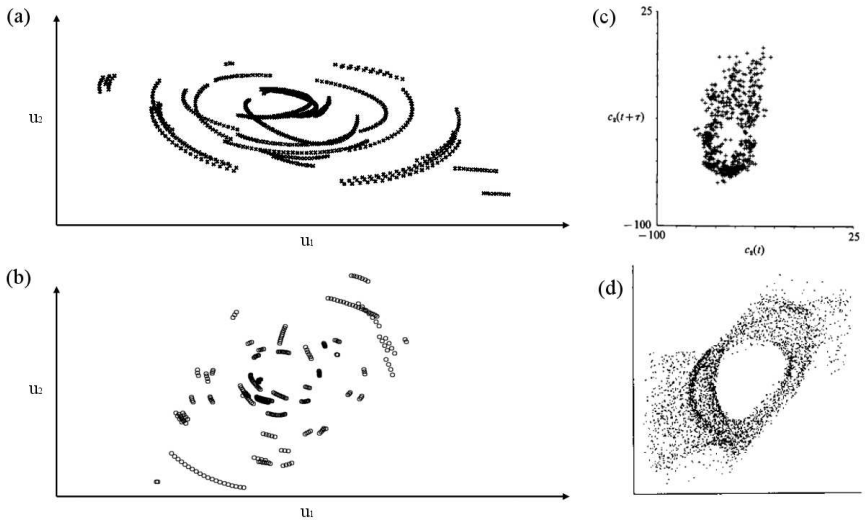

Figure 8.14: Poincaré maps in 2D planes (a) P1 and (b) P2 as defined in the text; (c) Poincaré map for the time variation of heat transport for weakly chaotic flow in a thermally driven, rotating fluid annulus [15] and (c) Poincaré map for weakly chaotic case for the time series of toroidal magnetic field [16].

8.5.5 Effect of Stratification on Coherent structures

To help us understand the effect of stratification on submerged jet, we look at the dynamics of the vortex formation close to the inlet immediately after the stratified jet is released. This is juxtaposed with a separate simulation with a similar setup (as Case B but without stratification). Fig. 8.15 shows the iso-surfaces of the q-criterion visualizing the vortical coherent structures in the flow near the inlet region. At $t^* = tu_{in}/h \approx 1$, in both cases, this value of q shows a single vortex which roughly follows the shape of the inlet. In a region immediately next to the jet inlet, regularly repeating, organized spanwise structures exist, revealing the laminar nature of the flow in this region. Further downstream, these organized structures start to break up as flow undergoes transition to turbulence. A swarm of hairpin-like vortices can be seen dominating the flow downstream of this region. For unstratified case, the flow acceleration is slow, owing to the absence of buoyancy. For $3 < t^* < 30$, this effect is seen in the longitudinal propagation of plume (see Movie S4). A striking feature of the stratified case, as evident from these figures, is the appearance of large-scale, C-shaped structures, which are found to

emanate aperiodically from the inlet and sweep through the entire plume (see Movies S3 and S5). One such large-scale structure can be clearly seen in Fig. 8.15 at $t^* = 30$. Fig. 8.16 and Movie S5 show several of these structures on the slope from top view long after the plume shape reached equilibrium.

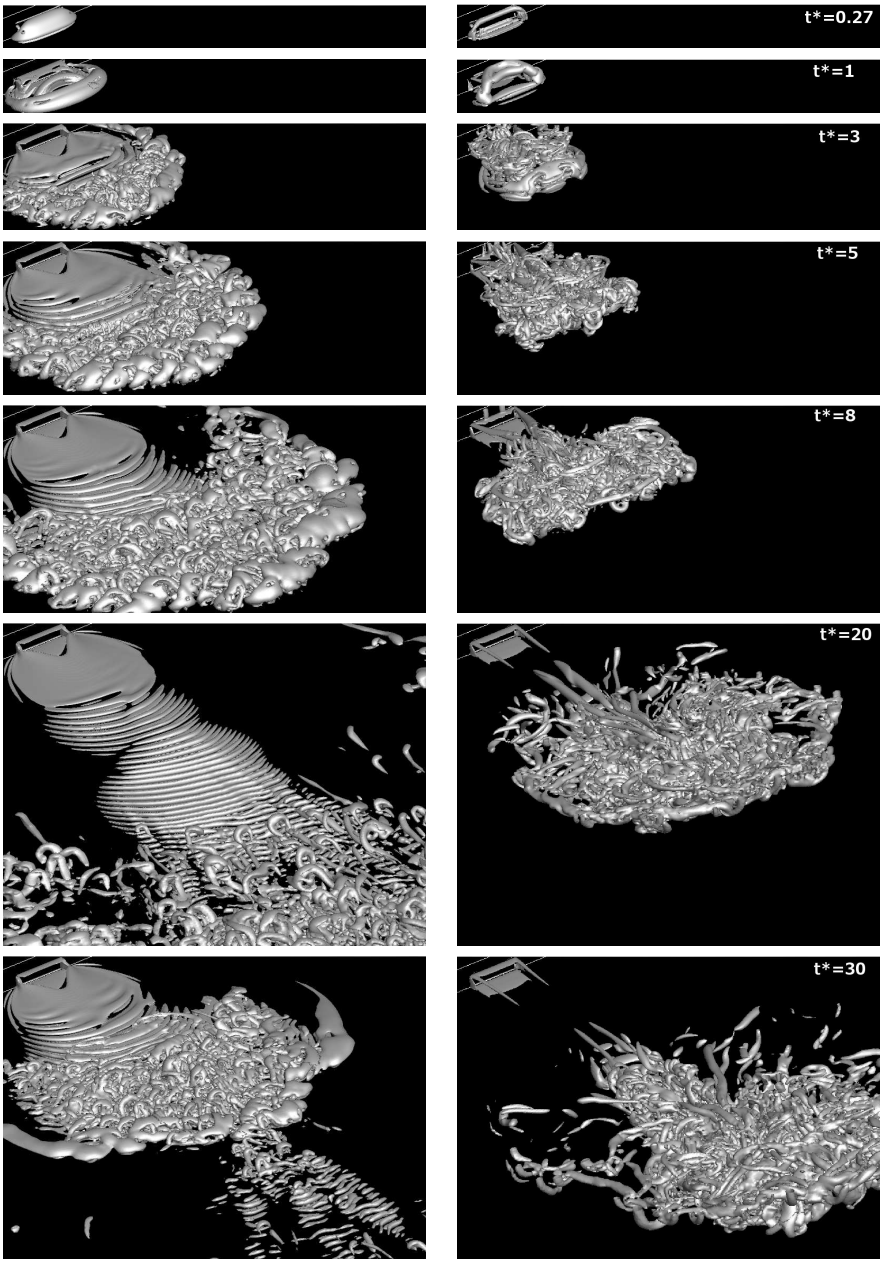

Figure 8.15: Iso-surfaces of q-structures visualizing vortical structures in stratified (left) and unstratified (right) submerged jet at non dimensional time $t^* = tu_{in}/h$ between 0 to 30

Figure 8.16: Iso-surfaces of q-structures on the slope after the plume reached quasi-equilibrium state for case B. Three different large-scale C-shaped structures are visible.

Chapter 9

Conclusion and summary

A review of previous related literature suggested that there are several published computational methods for a lower-order resource estimation at marine sites. But there was need for research for site-specific field-scale simulation for post-site-identification phase of MHK energy projects. In this dissertation, we used high-fidelity computational tools to study several issues of relevance for development and deployment of a multi-turbine array in the East River of New York City for a real-life MHK power project – Roosevelt Island Tidal Energy (RITE) project. We outlined a framework for design and modeling of an array of MHK turbines in the natural marine environment.

The deployment of turbines underwater was proposed by Verdant Power to be done in TriFrame configurations where turbines were placed in triplets at the vertices of a triangular frame. The TriFrames of turbines can then be used to rapidly deploy an array underwater. TriFrames are preferred configuration from underwater operation-and-maintenance point of view. We studied the hydrodynamics of turbines in a TriFrame configuration using model hydrokinetic turbines in an open-channel. Experiments were conducted by our colleagues at SAFL in a laboratory flume with a TriFrame consisting of 15 cm-diameter turbines. Subsequently, we performed geometry resolving LES based on the experiments. Geometry resolving LES is of special relevance to study interaction among hydrokinetic turbines because reduced order modeling techniques, such as actuator line/disc methods, cannot predict the near-wake accurately [11] since they do not model the nacelle and cannot capture the rich dynamics of the hub vortex. To the best of our knowledge, our work is the first time a geometry resolving simulation

was performed for a turbulent flow past multiple hydrokinetic turbines. The computed results were compared with the measurements from the laboratory experiments. The mean velocity and the turbulent statistics were accurately predicted in the wake of the TriFrame. Further analysis of the computed results revealed characteristic features of the TriFrame wake that could not be identified in a single turbine wake. In particular, the two rows of turbines in the TriFrame give rise to different wakes. For the upstream turbine in the TriFrame, the shear layer gets constricted after reaching the second row at 2D downstream distance. This is attributed to the Venturi effect which has been observed earlier in the experiments with wind turbines [94]. Consequently, flow acceleration is obtained in the region between the outer shear layers of the adjacent turbine wakes. The TKE levels are also lower in this region and the momentum deficit recovers faster for the upstream turbine. On comparison with a separate single turbine simulation, it was observed that the wake of the upstream turbine has higher velocity and lower TKE than the single turbine. The two second row turbines, however, produced higher TKE levels in the wake around the tip region in the near wake. In the farther wake after 5D, the TKE levels were similar. The general shape of the three wakes of turbines compared in Fig. 6.16 showed different characteristics. Since all three turbines rotate in same direction, the two downstream turbines (T2 and T3) are effected differently, resulting in the spanwise asymmetry of the superwake of the TriFrame (see Fig. 6.16). The faster momentum deficit recovery and lower TKE in the wake of the upstream turbine of the TriFrame are advantageous when using the TriFrame assembly to build a large turbine array. Higher TKE levels in some near-wake regions in the wake of the second row turbines will produces undesirable effect of higher fatigue loads on the downstream turbines in the array. If the TriFrames are used to build the array, the power produced by TriFrame is higher than three single turbines operating independently. The amount of excess power generated depends on the inter-TriFrame spacing in the array and increases with decreasing spacing. Therefore, estimating the power production of downstream TriFrame with three single turbines will underestimate the power by amount listed in last column of Table 6.2.

This simulation provided valuable insights regarding wake interaction in a multi-turbine array. Even though the simulations were performed at lab-scale, many general conclusions still remain applicable to other scales. In the future, these simulations

could be performed at higher Reynolds number representing field scale flows to more accurately quantify the role of Reynolds number on wake interaction. There is scope for further research of turbine-turbine interaction using the wake decomposition analysis. With the help of time-series data at locations in the wake, the wake meandering can be quantified for each turbine. It will be informative to perform a comparative study of wake meandering in a TriFrame versus an isolated turbine under same conditions.

As part of this dissertation, we also developed modules in a new generation Navier-Stokes solver on unstructured Cartesian grid with capability to locally refine the grid in the regions of interest. The local grid refinement enables multi-resolution simulations suitable for complex flows where vast ranges of flow scales are present. This method solves the full three-dimensional Navier Stokes equations on an unstructured grid having Cartesian cells of varying resolution. The fully unstructured approach eliminates problems with mass conservation but introduces challenge of defining neighborhood connectivity that works efficiently within a distributed computing memory architecture essential for calculations of High Performance Computing (HPC) clusters. Definition of data structures to define grid connectivity is crucial step for designing efficient solver on locally refined grids. Novel data structures and algorithms were developed for new grid connectivity for the unstructured grid solver. As a result, it was possible to perform simulations with large number of unstructured cells in realistic time scales.

The methods developed were validated using previously published experimental and numerical results. Validation was first done for a case of single turbine at lab-scale, for which, experimental measurements of velocity profiles were available. The prediction for actuator line modeling of turbine were in line with previously performed simulations as well as the experimental measurements Next, an array or turbines were simulated for experiments on a miniature wind-farm in SAFL wind tunnel. LES on locally refined grid good prediction in the wake of turbine and results which are characteristic of the actuator line models. The method was also validated for experiments with a model hydrokinetic turbine in SAFL main channel where mean velocity as well as velocity fluctuation measurements were recorded. This simulation was done by resolving the full geometry of the $0.5\,m$ hydrokinetic turbine using immersed boundary method. The LES predicted mean velocity and turbulence characteristics were in excellent agreement with the experiments as well as previous simulations.

The capability of unstructured Cartesian grid solver is employed to finally study the hydrodynamics of a 30-turbine array at the East River site. A detailed bathymetry of the river site, obtained from a recent survey, was used to create a digital elevation model of the river. The digital elevation model acted as immersed boundary for the LES of the East River site. Simulations were first performed in the river for a nominal flow rate without the turbines to obtain baseline flow characteristics. Field measurement in the river was made using ADCP to obtain a single vertical profile of streamwise velocity at a location. The velocity profile from the baseline flow was compared with this available velocity profile. The prediction of velocity profile agreed well with the field data giving a power law profile index similar to the measured data. The final LES of the East River channel with the inset turbine array of 10 TriFrames provided valuable insights about its hydrodynamics. The bathymetry of the river site resulted in unique flow patterns. Simulations indicated that an acceleration in the river flow in the spanwise region where turbines were not placed. Comparison with the baseline flow in terms of mean streamwise velocity as well as vorticity magnitude indicates that there is a very small signature of the turbine wake at the free surface of the channel. This effect could be negligible compared to the free surface disturbances present in the tidal channel otherwise. The wakes of first few TriFrames of the array were not aligned with the axis of rotation defined by orientation of turbines. This means that the yaw of the turbines should turn the turbine in the direction of the incoming flow. The yaw mechanism of the turbine was not modeled in the present simulation.

Subsequent work on the river flow simulation in the future can give us better answers for the deployment sites. In the present case, only limited bathymetry data was available upstream of the turbine array. A more expansive bathymetry of the site was needed in order to avoid the unwanted effects created by the inflow boundary treatment due to missing upstream section. For the future simulations, it is advisable to have longer upstream sections in the simulations, specially if complex features exist in the channel. In a modern hydrokinetic farm, the turbines yaw mechanism rotates the turbine to align the rotor in the direction of the incoming flow. This could be taken into account in the future simulations. One simple way could be to estimate a time-window-averaged velocity upstream of the turbine and use its direction to redefine the orientation of the turbine (or actuator line) rotor. Static grid refinement procedure was adopted in the

simulations here. A more desirable approach for future could be to use an adaptive criteria which dynamically refines the grid in the regions of the flow where small scales exist (or are predicted to exist).

As part of the thesis, a different type of environmental flow than the river flow was also studied. We investigated the flow of bottom-heavy density current developing on a large slope. Such density currents are often seen in nature e.g. rivers flowing merging the ocean, industrial effluents discharged in a river or lake, and saline under-currents in estuaries and oceans. While not directly related to the title of current dissertation, interesting results were obtained for a laboratory scale test. The LES module of the VFS model was used to simulate a turbulent stratified flow of a dense wall jet flow over two sloping beds of 5° and 15°, which were earlier experimentally studied by Christodoulou [107]. The stratified jet resulted in formation of density current plumes on the slope. The numerical simulations are compared with experimental results and shown to be in good qualitative agreement in terms of plume shape at quasi-equilibrium state. Visualizations of the simulated coherent structures shed new striking insights into the physics of such flows, revealing rich dynamics and large-scale instabilities. For the low slope angle case, very-large-scale C-shaped structures appear to be emanating from the inlet region. These structures appear periodically and travel down the slope. A closer look at the image of the experimental plume reveals regions of high dye concentrations in large C-shapes, indicating the presence of double C-shaped (or W-shaped) structures instead of single. This difference could be due to any slight uncertainty and/or asymmetry associated with the experimental conditions which are known to effect the flow regimes in the plume [106, 107]. A spectral analysis of velocity in the plume shows the frequency of the large-scale structures as $St = 0.0122$. Existence of the well known $f^{-5/3}$ decay in the inertial subrange of the spectra was also found. Non-linear analysis of time-series data collected at a point near bed for case B was also performed. This analysis confirms the presence of chaos for this case, whereas, for case A, no such conclusion was found. The attractor thus obtained is plotted in Figure 8.13 (c). Furthermore, comparison of vortical structures of stratified case with unstratified cases highlighted the role of stratification in the formation of density current plume. The spreading of the simulated plumes exhibit power law scaling with exponents comparable to those determined by earlier researchers. The plume shape as well as spreading compared well in the region

away from the inlet, but not close to the exit boundary. Close to the far end of the slope the comparison of the plume shape is difficult because of the ill-defined boundary of the plume in this region for case B. The experimental plume boundary is extracted as a continuous line from the image of plume, but in the computations it is extracted from the dye concentration contour threshold. Given that only two experiments are simulated, more research is needed to further study the effect of different bed slopes and Reynolds and Richardson numbers on the spreading laws.

References

[1] Kai-Wern Ng, Wei-Haur Lam, and Khai-Ching Ng. 2002–2012: 10 years of research progress in horizontal-axis marine current turbines. *Energies*, 6(3):1497–1526, 2013.

[2] The Marine and Hydrokinetic Energy Trade Association. U.s. marine and hydrokinetic renewable energy roadmap. Technical report.

[3] Xiaolei Yang, Seokkoo Kang, and Fotis Sotiropoulos. Toward a simulation-based approach for optimizing mhk turbine arrays in natural waterways. In *Proceedings of the 1st Marine Energy Technology Symposium*, April 2013.

[4] Dionysios Angelidis, Saurabh Chawdhary, and Fotis Sotiropoulos. Unstructured cartesian refinement with sharp interface immersed boundary method for 3d unsteady incompressible flows. *Journal of Computational Physics*, 325:272–300, 2016.

[5] Iman Borazjani, Liang Ge, and Fotis Sotiropoulos. Curvilinear immersed boundary method for simulating fluid structure interaction with complex 3d rigid bodies. *Journal of Computational physics*, 227(16):7587–7620, 2008.

[6] Riccardo Broglia, Andrea Pascarelli, and Ugo Piomelli. Large-eddy simulations of ducts with a free surface. *Journal of Fluid Mechanics*, 484:223–253, 2003.

[7] LeonardoP. Chamorro and Fernando Port-Agel. A wind-tunnel investigation of wind-turbine wakes: Boundary-layer turbulence effects. *Boundary-Layer Meteorology*, 132(1):129–149, 2009.

[8] Xiaolei Yang, Fotis Sotiropoulos, Robert J. Conzemius, John N. Wachtler, and Mike B. Strong. Large-eddy simulation of turbulent flow past wind turbines/farms: the virtual wind simulator (VWiS). *Wind Energy*, 2014, DOI: 10.1002/we.1802.

[9] Leonardo P Chamorro and Fernando Porte-Agel. Turbulent flow inside and above a wind farm: a wind-tunnel study. *Energies*, 4(11):1916–1936, 2011.

[10] LP Chamorro, C Hill, S Morton, C Ellis, REA Arndt, and F Sotiropoulos. On the interaction between a turbulent open channel flow and an axial-flow turbine. *Journal of Fluid Mechanics*, 716:658–670, 2013.

[11] Seokkoo Kang, Xiaolei Yang, and Fotis Sotiropoulos. On the onset of wake meandering for an axial flow turbine in a turbulent open channel flow. *Journal of Fluid Mechanics*, 744:376–403, 2014.

[12] LLC Verdant Power. Pilot lisence application roosevelt island tidal energy project FERC No. 12611. Technical Report 2, Verdant Power, LLC, Verdant Power, Inc., P.O. Box 282, Roosevelt Island, New York, NY 10044, 2010. Final kinetic hydropower pilot license application.

[13] Vassilios A Tsihrintzis and Vahid Alavian. Spreading of three-dimensional inclined gravity plumes. *Journal of Hydraulic Research*, 34(5):695–711, 1996.

[14] Andrew M Fraser and Harry L Swinney. Independent coordinates for strange attractors from mutual information. *Physical review A*, 33(2):1134, 1986.

[15] PL Read, MJ Bel, DW Johnson, and RM Small. Quasi-periodic and chaotic flow regimes in a thermally driven, rotating fluid annulus. *Journal of Fluid Mechanics*, 238:599–632, 1992.

[16] A Phillips, J Brooke, and D Moss. The importance of physical structure in solar dynamo models. *Astronomy & Astrophysics*, 392(2):713–727, 2002.

[17] World Enery Council. Hydropower, 2011. [Online; accessed 21-February-2014].

[18] United States: Environmental Protection Agency. International energy statistics, 2014. [Online; accessed 21-February-2014].

[19] Darren M Ward, Keith H Nislow, and Carol L Folt. Bioaccumulation syndrome: identifying factors that make some stream food webs prone to elevated mercury bioaccumulation. *Annals of the New York Academy of Sciences*, 1195(1):62–83, 2010.

[20] Annika W Walters and David M Post. How low can you go? impacts of a low-flow disturbance on aquatic insect communities. *Ecological Applications*, 21(1):163–174, 2011.

[21] David M Rosenberg, Patrick McCully, and Catherine M Pringle. Global-scale environmental effects of hydrological alterations: introduction. *BioScience*, 50(9):746–751, 2000.

[22] David Finger, Peter Bossard, Martin Schmid, Lorenz Jaun, Beat Müller, Daniel Steiner, Erwin Schäffer, Markus Zeh, and Alfred Wüest. Effects of alpine hydropower operations on primary production in a downstream lake. *Aquatic Sciences*, 69(2):240–256, 2007.

[23] MJ Khan, G Bhuyan, MT Iqbal, and JE Quaicoe. Hydrokinetic energy conversion systems and assessment of horizontal and vertical axis turbines for river and tidal applications: A technology status review. *Applied Energy*, 86(10):1823–1835, 2009.

[24] Sanjiv K Sinha, Fotis Sotiropoulos, and A Jacob Odgaard. Three-dimensional numerical model for flow through natural rivers. *Journal of Hydraulic Engineering*, 124(1):13–24, 1998.

[25] José F Rodriguez, Fabián A Bombardelli, Marcelo H García, Kelly M Frothingham, Bruce L Rhoads, and Jorge D Abad. High-resolution numerical simulation of flow through a highly sinuous river reach. *Water Resources Management*, 18(3):177–199, 2004.

[26] Victor Yakhot and Steven A Orszag. Renormalization group analysis of turbulence. i. basic theory. *Journal of scientific computing*, 1(1):3–51, 1986.

[27] Victor Yakhot and Leslie M Smith. The renormalization group, the -expansion and derivation of turbulence models. *Journal of Scientific Computing*, 7(1):35–61, 1992.

[28] Jorge D Abad, Bruce L Rhoads, İnci Güneralp, and Marcelo H García. Flow structure at different stages in a meander-bend with bendway weirs. *Journal of Hydraulic Engineering*, 134(8):1052–1063, 2008.

[29] Seokkoo Kang, Anne Lightbody, Craig Hill, and Fotis Sotiropoulos. High-resolution numerical simulation of turbulence in natural waterways. *Advances in Water Resources*, 34(1):98–113, 2011.

[30] Liang Ge and Fotis Sotiropoulos. A numerical method for solving the 3D unsteady incompressible NavierStokes equations in curvilinear domains with complex immersed boundaries. *Journal of Computational Physics*, 225(2):1782–1809, August 2007.

[31] Massimo Germano, Ugo Piomelli, Parviz Moin, and William H Cabot. A dynamic subgrid-scale eddy viscosity model. *Physics of Fluids A: Fluid Dynamics (1989-1993)*, 3(7):1760–1765, 1991.

[32] Thorsten Stoesser, Nils Ruether, and Nils Reidar Boe Olsen. Calculation of primary and secondary flow and boundary shear stresses in a meandering channel. *Advances in Water Resources*, 33(2):158–170, 2010.

[33] Seokkoo Kang and Fotis Sotiropoulos. Assessing the predictive capabilities of isotropic, eddy viscosity reynolds-averaged turbulence models in a natural-like meandering channel. *Water Resources Research*, 48(6), 2012.

[34] Tuy NM Phan, John C Wells, William D Kirkey, Mohammad S Islam, and James S Bonner. Large eddy simulation of the flow field in the hudson river. In *ASME-JSME-KSME 2011 Joint Fluids Engineering Conference*, pages 3933–3939. American Society of Mechanical Engineers, 2011.

[35] Ali Khosronejad, Seokkoo Kang, Iman Borazjani, and Fotis Sotiropoulos. Curvilinear immersed boundary method for simulating coupled flow and bed morphodynamic interactions due to sediment transport phenomena. *Advances in Water Resources*, 34(7):829–843, 2011.

[36] Ali Khosronejad, Seokkoo Kang, and Fotis Sotiropoulos. Experimental and computational investigation of local scour around bridge piers. *Advances in Water Resources*, 37:73–85, 2012.

[37] Ali Khosronejad, Craig Hill, Seokkoo Kang, and Fotis Sotiropoulos. Computational and experimental investigation of scour past laboratory models of stream restoration rock structures. *Advances in Water Resources*, 54:191–207, 2013.

[38] LS Blunden and AS Bahaj. Initial evaluation of tidal stream energy resources at portland bill, uk. *Renewable Energy*, 31(2):121–132, 2006.

[39] Seif Eddine Ben Elghali, Rémi Balme, Karine Le Saux, Mohamed El Hachemi Benbouzid, Jean Frédéric Charpentier, and Frédéric Hauville. A simulation model for the evaluation of the electrical power potential harnessed by a marine current turbine. *Oceanic Engineering, IEEE Journal of*, 32(4):786–797, 2007.

[40] RH Karsten, JM McMillan, MJ Lickley, and RD Haynes. Assessment of tidal current energy in the minas passage, bay of fundy. *Proceedings of the Institution of Mechanical Engineers, Part A: Journal of Power and Energy*, 222(5):493–507, 2008.

[41] R Carballo, G Iglesias, and A Castro. Numerical model evaluation of tidal stream energy resources in the ría de muros (nw spain). *Renewable Energy*, 34(6):1517–1524, 2009.

[42] Mårten Grabbe, Emilia Lalander, Staffan Lundin, and Mats Leijon. A review of the tidal current energy resource in norway. *Renewable and Sustainable Energy Reviews*, 13(8):1898–1909, 2009.

[43] B Polagye, M Kawase, and P Malte. In-stream tidal energy potential of puget sound, washington. *Proceedings of the Institution of Mechanical Engineers, Part A: Journal of Power and Energy*, 223(5):571–587, 2009.

[44] Fergal ORourke, Fergal Boyle, and Anthony Reynolds. Tidal current energy resource assessment in ireland: Current status and future update. *Renewable and Sustainable Energy Reviews*, 14(9):3206–3212, 2010.

[45] J Xia, RA Falconer, and B Lin. Numerical model assessment of tidal stream energy resources in the severn estuary, uk. *Proceedings of the Institution of Mechanical Engineers, Part A: Journal of Power and Energy*, 224(7):969–983, 2010.

[46] Yun Seng Lim and Siong Lee Koh. Analytical assessments on the potential of harnessing tidal currents for electricity generation in malaysia. *Renewable Energy*, 35(5):1024–1032, 2010.

[47] Zafer Defne, Kevin A Haas, and Hermann M Fritz. Numerical modeling of tidal currents and the effects of power extraction on estuarine hydrodynamics along the georgia coast, usa. *Renewable Energy*, 36(12):3461–3471, 2011.

[48] Michael LS Abundo, AC Nerves, MRCO Ang, EC Paringit, Lawrence PC Bernardo, and Cesar L Villanoy. Energy potential metric for rapid macro-level resource assessment of tidal in-stream energy in the philippines. In *Environment and Electrical Engineering (EEEIC), 2011 10th International Conference on*, pages 1–4. IEEE, 2011.

[49] Huajun Li, Guoxiang Wu, Bingchen Liang, and Fan Fei. Numerical assessment of tidal stream energy resource in langyatai strait. In *OCEANS, 2012-Yeosu*, pages 1–5. IEEE, 2012.

[50] Paul A Work, Kevin A Haas, Zafer Defne, and Thomas Gay. Tidal stream energy site assessment via three-dimensional model and measurements. *Applied Energy*, 102:510–519, 2013.

[51] Chris Garrett and Patrick Cummins. The power potential of tidal currents in channels. *Proceedings of the Royal Society A: Mathematical, Physical and Engineering Science*, 461(2060):2563–2572, 2005.

[52] Chris Garrett and Patrick Cummins. The efficiency of a turbine in a tidal channel. *Journal of fluid mechanics*, 588:243–251, 2007.

[53] Chris Garrett and Patrick Cummins. Limits to tidal current power. *Renewable Energy*, 33(11):2485–2490, 2008.

[54] George L Mellor. *Users guide for a three-dimensional, primitive equation, numerical ocean model (June 2003 version)*. Program in Atmospheric and Oceanic Sciences, Princeton University Princeton, NJ 6-28, 2003.

[55] Dale B Haidvogel, H Arango, WP Budgell, BD Cornuelle, E Curchitser, E Di Lorenzo, K Fennel, WR Geyer, AJ Hermann, L Lanerolle, et al. Ocean forecasting in terrain-following coordinates: Formulation and skill assessment of the regional ocean modeling system. *Journal of Computational Physics*, 227(7):3595–3624, 2008.

[56] B Sanderse, SP Pijl, and B Koren. Review of computational fluid dynamics for wind turbine wake aerodynamics. *Wind Energy*, 14(7):799–819, 2011.

[57] Jens Norkær Sørensen and Wen Zhong Shen. Numerical modeling of wind turbine wakes. *Journal of fluids engineering*, 124(2):393–399, 2002.

[58] Stefan Ivanell, Robert Mikkelsen, Jens N Sørensen, and Dan Henningson. Stability analysis of the tip vortices of a wind turbine. *Wind Energy*, 13(8):705–715, 2010.

[59] Seokkoo Kang and Fotis Sotiropoulos. Numerical modeling of 3D turbulent free surface flow in natural waterways. *Advances in Water Resources*, 40:23–36, May 2012.

[60] Michael J Lawson, Ye Li, and Danny C Sale. Development and verification of a computational fluid dynamics model of a horizontal-axis tidal current turbine. In *ASME 2011 30th International Conference on Ocean, Offshore and Arctic Engineering*, pages 711–720. American Society of Mechanical Engineers, 2011.

[61] Grégory Pinon, Paul Mycek, Grégory Germain, and Elie Rivoalen. Numerical simulation of the wake of marine current turbines with a particle method. *Renewable Energy*, 46:111–126, 2012.

[62] AS Bahaj, WMJ Batten, and G McCann. Experimental verifications of numerical predictions for the hydrodynamic performance of horizontal axis marine current turbines. *Renewable Energy*, 32(15):2479–2490, 2007.

[63] Jonathan A Colby and Mary Ann Adonizio. Hydrodynamic analysis of kinetic hydropower arrays. *Waterpower XVI*, 204, 2009.

[64] Scott C James, Eddy Seetho, Craig Jones, and Jesse Roberts. Simulating environmental changes due to marine hydrokinetic energy installations. In *OCEANS 2010*, pages 1–10. IEEE, 2010.

[65] Matthew J Churchfield, Ye Li, and Patrick J Moriarty. A large-eddy simulation study of wake propagation and power production in an array of tidal-current turbines. *Philosophical Transactions of the Royal Society A: Mathematical, Physical and Engineering Sciences*, 371(1985):20120421, 2013.

[66] Luolin Bai, Roy RG Spence, and Grégory Dudziak. Investigation of the influence of array arrangement and spacing on tidal energy converter (tec) performance using a 3-dimensional cfd model. In *Proceedings of the 8th European Wave and Tidal Energy Conference, Uppsala, Sweden*, pages 654–660, 2009.

[67] AS Bahaj, LE Myers, RI Rawlinson-Smith, and Matthew Thomson. The effect of boundary proximity upon the wake structure of horizontal axis marine current turbines. *Journal of Offshore Mechanics and Arctic Engineering*, 134(2):021104, 2012.

[68] Scott C James, J Barco, E Johnson, JD Roberts, and S Lefantzi. Verifying marine-hydro-kinetic energy generation simulations using snl-efdc. In *OCEANS 2011*, pages 1–9. IEEE, 2011.

[69] Ali Khosronejad, Jessica Kozarek, Amy Hansen, Kristopher Guentzel, Miki Hondzo, Peter Wilcock, Michele Guala, Jacques Finlay, and Fotis Sotiropoulos. Data-driven LES of turbulence and solute transport in a natural stream. *Bulletin of the American Physical Society*, 59, 2014.

[70] Marsha J Berger and Joseph Oliger. Adaptive mesh refinement for hyperbolic partial differential equations. *Journal of Computational Physics*, 53(3):484–512, 1984.

[71] Joseph Smagorinsky. General circulation experiments with the primitive equations: I. the basic experiment*. *Monthly weather review*, 91(3):99–164, 1963.

[72] David C Wilcox. Reassessment of the scale-determining equation for advanced turbulence models. *AIAA journal*, 26(11):1299–1310, 1988.

[73] Xiaolei Yang, Seokkoo Kang, and Fotis Sotiropoulos. Computational study and modeling of turbine spacing effects in infinite aligned wind farms. *Physics of Fluids (1994-present)*, 24(11):115107, 2012.

[74] Javier Jiménez. Turbulent flows over rough walls. *Annu. Rev. Fluid Mech.*, 36:173–196, 2004.

[75] Hao Lu and Fernando Port-Agel. Large-eddy simulation of a very large wind farm in a stable atmospheric boundary layer. *Physics of Fluids*, 23(6), 2011.

[76] Jens N. Sørensen, Robert F. Mikkelsen, Dan S. Henningson, Stefan Ivanell, Sasan Sarmast, and Søren J. Andersen. Simulation of wind turbine wakes using the actuator line technique. *Philosophical Transactions of the Royal Society of London A: Mathematical, Physical and Engineering Sciences*, 373(2035), 2015.

[77] Wen Zhong Shen, Jens Nørkær Sørensen, and Jianhui Zhang. Actuator surface model for wind turbine flow computations. In *2007 European Wind Energy Conference and Exhibition*, 2007.

[78] Wen Zhong Shen, Jian Hui Zhang, and Jens Nørkær Sørensen. The actuator surface model: a new navier–stokes based model for rotor computations. *Journal of Solar Energy Engineering*, 131(1):011002, 2009.

[79] X. Yang, X. Zhang, Z. Li, and G.-W. He. A smoothing technique for discrete delta functions with application to immersed boundary method in moving boundary simulations. *Journal of Computational Physics*, 228:7821–7836, November 2009.

[80] Anvar Gilmanov and Fotis Sotiropoulos. A hybrid cartesian/immersed boundary method for simulating flows with 3D, geometrically complex, moving bodies. *Journal of Computational Physics*, 207(2):457 – 492, 2005.

[81] L. Ge and F. Sotiropoulos. A numerical method for solving the 3D unsteady incompressible navier-stokes equations in curvilinear domains with complex immersed boundaries. *Journal of Computational Physics*, 225(2):1782–1809, 2007.

[82] Iman Borazjani, Liang Ge, and Fotis Sotiropoulos. Curvilinear immersed boundary method for simulating fluid structure interaction with complex 3D rigid bodies. *Journal of Computational Physics*, 227(16):7587 – 7620, 2008.

[83] A. Gilmanov, F. Sotiropoulos, and E. Balaras. A general reconstruction algorithm for simulating flows with complex 3D immersed boundaries on cartersian grids. *Journal of Computational Physics*, 191(2):660–669, 2003.

[84] MultiMedia LLC. PETSc Users Manual , 2016.

[85] Yu-Ting Wu and Fernando Port-Agel. Simulation of turbulent flow inside and above wind farms: Model validation and layout effects. *Boundary-Layer Meteorology*, 146(2):181–205, 2013.

[86] R Sheldahl, Fotis Sotiropoulos, Robert J. Conzemius, John N. Wachtler, and Mike B. Strong. Aerodynamic characteristics of seven airfoil sections through 180 degrees angle of attack for use in aerodynamic analysis of vertical axis wind turbines. SAND80-2114, Sandia National Laboratories, Albuquerque, New Mexico, March 1981.

[87] Meng Wang and Parviz Moin. Dynamic wall modeling for large-eddy simulation of complex turbulent flows. *Physics of Fluids (1994-present)*, 14(7):2043–2051, 2002.

[88] Xiaolei Yang, Fotis Sotiropoulos, Robert J Conzemius, John N Wachtler, and Mike B Strong. Large-eddy simulation of turbulent flow past wind turbines/farms: the virtual wind simulator (vwis). *Wind Energy*, 18(12):2025–2045, 2015.

[89] Meng Wang and Parviz Moin. Dynamic wall modeling for large-eddy simulation of complex turbulent flows. *Physics of Fluids*, 14(7):2043–2051, 2002.

[90] Craig Hill, Mirko Musa, Leonardo P Chamorro, Chris Ellis, and Michele Guala. Local scour around a model hydrokinetic turbine in an erodible channel. *Journal Hydraulic Engineering*, 140(8):04014037, 2014.

[91] Craig Hill, Mirko Musa, and Michele Guala. Interaction between instream axial flow hydrokinetic turbines and uni-directional flow bedforms. *Renewable Energy*, 86:409–421, 2016.

[92] Craig Hill, Jessica Kozarek, Fotis Sotiropoulos, and Michele Guala. Hydrodynamics and sediment transport in a meandering channel with a model axial-flow hydrokinetic turbine. *Water Resources Research*, 52(2):860–879, 2016.

[93] Seokkoo Kang and Fotis Sotiropoulos. Numerical modeling of 3D turbulent free surface flow in natural waterways. *Advances in Water Resources*, 40:23–36, 2012.

[94] Leonardo P Chamorro, REA Arndt, and Fotis Sotiropoulos. Turbulent flow properties around a staggered wind farm. *Boundary-layer meteorology*, 141(3):349–367, 2011.

[95] Idriss Ammara, Christophe Leclerc, and Christian Masson. A viscous three-dimensional differential/actuator-disk method for the aerodynamic analysis of wind farms. *Journal of Solar Energy Engineering*, 124(4):345–356, 2002.

[96] John E Simpson. *Gravity currents: In the environment and the laboratory*. Cambridge University Press, 1999.

[97] Herbert E Huppert and John E Simpson. The slumping of gravity currents. *Journal of Fluid Mechanics*, 99(04):785–799, 1980.

[98] J Hacker, PF Linden, and SB Dalziel. Mixing in lock-release gravity currents. *Dynamics of Atmospheres and Oceans*, 24(1):183–195, 1996.

[99] Jeffrey D Parsons and Marcelo H Garcıa. Similarity of gravity current fronts. *Physics of Fluids (1994-present)*, 10(12):3209–3213, 1998.

[100] TH Ellison and JS Turner. Turbulent entrainment in stratified flows. *Journal of Fluid Mechanics*, 6(03):423–448, 1959.

[101] DL Wilkinson and IR Wood. Some observations on the motion of the head of a density current. *Journal of Hydraulic Research*, 10(3):305–324, 1972.

[102] RE Britter and PF Linden. The motion of the front of a gravity current travelling down an incline. *Journal of Fluid Mechanics*, 99(03):531–543, 1980.

[103] W Hauenstein and TH Dracos. Investigation of plunging density currents generated by inflows in lakes. *Journal of Hydraulic Research*, 22(3):157–179, 1984.

[104] Vahid Alavian. Behavior of density currents on an incline. *Journal of Hydraulic Engineering*, 112(1):27–42, 1986.

[105] Sung-Uk Choi and Marcelo H Garcia. Spreading of gravity plumes on an incline. *Coastal Engineering Journal*, 43(04):221–237, 2001.

[106] GC Christodoulou and FE Tzachou. Experiments on 3-D turbulent density currents. In *Preprints of 4th Intern. Symposium on Stratified Flows, Grenoble, France*, 1994.

[107] George C Christodoulou. Lateral growth of 3-D density currents. In *Proceedings of the 29th Congress-International Association for Hydraulic Research, Beijing, China*, volume B, pages 29–34, 2001.

[108] Mariano I Cantero, JR Lee, S Balachandar, and Marcelo H Garcia. On the front velocity of gravity currents. *Journal of Fluid Mechanics*, 586:1–39, 2007.

[109] Talia Tokyay, George Constantinescu, and Eckart Meiburg. Lock-exchange gravity currents with a high volume of release propagating over a periodic array of obstacles. *Journal of Fluid Mechanics*, 672:570–605, 2011.

[110] Talia Tokyay, George Constantinescu, and Eckart Meiburg. Lock-exchange gravity currents with a low volume of release propagating over an array of obstacles. *Journal of Geophysical Research: Oceans*, 119(5):2752–2768, 2014.

[111] T Tokyay, G Constantinescu, E Gonzalez-Juez, and E Meiburg. Gravity currents propagating over periodic arrays of blunt obstacles: Effect of the obstacle size. *Journal of Fluids and Structures*, 27(5):798–806, 2011.

[112] Talia Tokyay, George Constantinescu, and Eckart Meiburg. Tail structure and bed friction velocity distribution of gravity currents propagating over an array of obstacles. *Journal of Fluid Mechanics*, 694:252–291, 2012.

[113] E Gonzalez-Juez, E Meiburg, and G Constantinescu. The interaction of a gravity current with a circular cylinder mounted above a wall: Effect of the gap size. *Journal of Fluids and Structures*, 25(4):629–640, 2009.

[114] E Gonzalez-Juez, E Meiburg, T Tokyay, and G Constantinescu. Gravity current flow past a circular cylinder: forces, wall shear stresses and implications for scour. *Journal of Fluid Mechanics*, 649:69–102, 2010.

[115] Seng Keat Ooi, George Constantinescu, and Larry J Weber. 2D large-eddy simulation of lock-exchange gravity current flows at high grashof numbers. *Journal of Hydraulic Engineering*, 133(9):1037–1047, 2007.

[116] Thomas Bonometti, Marius Ungarish, and Sivaramakrishnan Balachandar. A numerical investigation of high-reynolds-number constant-volume non-boussinesq density currents in deep ambient. *Journal of Fluid Mechanics*, 673:574–602, 2011.

[117] Thomas Bonometti, Sivaramakrishnan Balachandar, and Jacques Magnaudet. Wall effects in non-boussinesq density currents. *Journal of fluid mechanics*, 616:445, 2008.

[118] Marius Ungarish. Intrusive gravity currents in a stratified ambient: shallow-water theory and numerical results. *Journal of Fluid Mechanics*, 535:287–323, 2005.

[119] Carlos Härtel, Eckart Meiburg, and Frieder Necker. Analysis and direct numerical simulation of the flow at a gravity-current head. part 1. flow topology and front speed for slip and no-slip boundaries. *Journal of Fluid Mechanics*, 418:189–212, 2000.

[120] Carlos Härtel, Fredrik Carlsson, and Mattias Thunblom. Analysis and direct numerical simulation of the flow at a gravity-current head. part 2. the lobe-and-cleft instability. *Journal of Fluid Mechanics*, 418:213–229, 2000.

[121] Seng Keat Ooi, George Constantinescu, and Larry Weber. A numerical study of intrusive compositional gravity currents. *Physics of Fluids (1994-present)*, 19(7):076602, 2007.

[122] Mariano I Cantero, S Balachandar, and Marcelo H Garcia. High-resolution simulations of cylindrical density currents. *Journal of Fluid Mechanics*, 590:437–469, 2007.

[123] Seng Keat Ooi, George Constantinescu, and Larry Weber. Numerical simulations of lock-exchange compositional gravity current. *Journal of Fluid Mechanics*, 635:361–388, 2009.

[124] George Constantinescu. LES of lock-exchange compositional gravity currents: a brief review of some recent results. *Environmental Fluid Mechanics*, 14(2):295–317, 2014.

[125] Joongcheol Paik, Afshin Eghbalzadeh, and Fotis Sotiropoulos. Three-dimensional unsteady rans modeling of discontinuous gravity currents in rectangular domains. *Journal of Hydraulic Engineering*, 135(6):505–521, 2009.

[126] Talia E Tokyay and Marcelo H García. Effect of initial excess density and discharge on constant flux gravity currents propagating on a slope. *Environmental Fluid Mechanics*, 14(2):409–429, 2014.

[127] Bahar Firoozabadi, Hossein Afshin, and Ehsan Aram. Three-dimensional modeling of density current in a straight channel. *Journal of Hydraulic Engineering*, 135(5):393–402, 2009.

[128] T Maxworthy and RI Nokes. Experiments on gravity currents propagating down slopes. part 1. the release of a fixed volume of heavy fluid from an enclosed lock into an open channel. *Journal of Fluid Mechanics*, 584:433–454, 2007.

[129] A Dai, CE Ozdemir, MI Cantero, and S Balachandar. Gravity currents from instantaneous sources down a slope. *Journal of Hydraulic Engineering*, 138(3):237–246, 2011.

[130] Andrew N Ross, PF Linden, and Stuart B Dalziel. A study of three-dimensional gravity currents on a uniform slope. *Journal of Fluid Mechanics*, 453:239–261, 2002.

[131] VK Birman, BA Battandier, E Meiburg, and PF Linden. Lock-exchange flows in sloping channels. *Journal of Fluid Mechanics*, 577:53–77, 2007.

[132] A Ooi, N Zgheib, and S Balachandar. Direct numerical simulation of three-dimensional gravity current on a uniform slope. *Procedia Engineering*, 126:372–376, 2015.

[133] Ali Khosronejad and Fotis Sotiropoulos. Numerical simulation of sand waves in a turbulent open channel flow. *Journal of Fluid Mechanics*, 753:150–216, 2014.

[134] Hyunkyung Lim, Yan Yu, James Glimm, and David H Sharp. Mathematical, physical and numerical principles essential for models of turbulent mixing. In *Nonlinear Conservation Laws and Applications*, pages 405–413. Springer, 2011.

[135] Liang Ge and Fotis Sotiropoulos. A numerical method for solving the 3D unsteady incompressible navier-stokes equations in curvilinear domains with complex immersed boundaries. *Journal of computational physics*, 225(2):1782–1809, 2007.

[136] AG Venetsanos, GM Horsch, and GC Christodoulou. Assesment of turbulence modelling of density currents developing three dimensionally on a slope. *Journal of Marine Environmental Engineering*, 8(2):147–154, 2005.

[137] Vassilios Andrew Tsihrintzis. *Theoretical and experimental investigation of three-dimensional boundary-attached density currents*. PhD thesis, Department of Civil Engineering, University of Illinois, Urbana, IL, USA, May 1998.

[138] Georgios M Horsch. The structure of two-dimensional, steady, miscible laminar density currents flowing down an incline. *Journal of Hydraulic Research*, 42(2):173–181, 2004.

[139] Trevor R Fietz and Ian R Wood. Three-dimensional density current. *Journal of the Hydraulics Division*, 93(6):1–24, 1967.

[140] Georgios M Horsch. Scaling of three-dimensional, miscible, laminar density currents flowing down an incline. In *E-Proceedings of the VIII International Conference on Protection and Restoration of the Environment, Chania, Greece*, Chania, Greece, July 2006.

[141] Norman H Packard, James P Crutchfield, J Doyne Farmer, and Robert S Shaw. Geometry from a time series. *Physical review letters*, 45(9):712, 1980.

[142] Michael T Rosenstein, James J Collins, and Carlo J De Luca. Reconstruction expansion as a geometry-based framework for choosing proper delay times. *Physica D: Nonlinear Phenomena*, 73(1):82–98, 1994.

[143] Matthew B Kennel, Reggie Brown, and Henry DI Abarbanel. Determining embedding dimension for phase-space reconstruction using a geometrical construction. *Physical review A*, 45(6):3403, 1992.

[144] Holger Kantz. A robust method to estimate the maximal lyapunov exponent of a time series. *Physics letters A*, 185(1):77–87, 1994.

Appendix A

Calculation of power production ratios for TriFrames in Table 6.2]

Power produced by a turbine P is given as:

$$P = \frac{1}{2}\rho A C_p U^3 \tag{A.1}$$

where C_p is the power coefficient of the turbine, ρ is density of fluid, $A = 0.25\pi D^2$ is area intercepted by turbine and U is the incoming fluid velocity. Assuming all turbines have the same diameter, constant fluid density and are operating at the same power coefficient, for two different incoming velocities U_1 and U_2 the power production ratio is given as

$$\frac{P_1}{P_2} = \left(\frac{U_1}{U_2}\right)^3 \tag{A.2}$$

Consider two units in an array of single turbines such that one turbine is placed in wake of another. The incoming velocity $U_{hub,-1D}$ for preceding turbine and $U^{(2)}_{hub,-1D}$ for the next downstream turbine in array are related by $U^{(2)}_{hub,-1D} = R * U_{hub,-1D}$ where R and $U_{hub,-1D}$ are recovery fraction (shown as % in Table 6.2 or in Fig. 6.17(b)) and incoming velocity for the preceding turbine (ST1) in the upstream unit. Same relationship holds true for similarly positioned turbines in two TriFrame units for an array of TriFrames. $U_{hub,-1D}$ for different upstream turbines are listed in Table A.1. Using the above relation (in Eq. A.2) for T4 as 1 and ST2 as 2 we can write,

	Single Turine (ST1)	TriFrame T1	TriFrame T2	TriFrame T3
$U_{hub,-1D}/U_b$	1.135	1.135	1.123	1.126

Table A.1: Incoming velocity for upstream TriFrame turbines or single turbine.

$$\begin{aligned}\frac{P_{T4}}{P_{ST2}} &= \left(\frac{R_{T1}U_{hub,-1D,T1}}{R_{ST1}U_{hub,-1D,ST1}}\right)^3 \\ &= \left(\frac{R_{T1}\times 1.135U_b}{R_{ST1}\times 1.135U_b}\right)^3 \\ &= \left(\frac{R_{T1}}{R_{ST1}}\right)^3\end{aligned} \tag{A.3}$$

and

$$\begin{aligned}\frac{P_{ST2}}{P_{\Delta 2}} &= \frac{P_{ST2}}{P_{T4}+P_{T5}+P_{T6}} \\ &= \frac{(R_{ST1}U_{hub,-1D,ST1})^3}{(R_{T1}U_{hub,-1D,T1})^3+(R_{T2}U_{hub,-1D,T2})^3+(R_{T3}U_{hub,-1D,T3})^3} \\ &= \frac{(R_{ST1}\times 1.135U_b)^3}{(R_{T1}\times 1.135U_b)^3+(R_{T2}\times 1.123U_b)^3+(R_{T3}\times 1.126U_b)^3} \\ &= \frac{(1.135R_{ST1})^3}{(1.135R_{T1})^3+(1.123R_{T2})^3+(1.126R_{T3})^3}\end{aligned} \tag{A.4}$$

Columns four and five in Table 6.2 are populated using the above relations A.3 and A.4, respectively, and the values of recovery (R) at respective downstream distances in the same table.